SURFACE CHARACTERISTICS, MINERALOGY AND GEOCHEMISTRY OF THE GİCİK LOW–SULFIDATION EPITHERMAL AU DEPOSIT (ANKARA PROVINCE, CENTRAL ANATOLIA)

A THESIS SUBMITTED TO
THE GRADUATE SCHOOL OF NATURAL AND APPLIED SCIENCES
OF
MIDDLE EAST TECHNICAL UNIVERSITY

BY

AKIN ÇİL

IN PARTIAL FULFILLMENT OF THE REQUIREMENTS
FOR
THE DEGREE OF MASTER OF SCIENCE
IN
GEOLOGICAL ENGINEERING

SEPTEMBER 2019

Approval of the thesis:

SURFACE CHARACTERISTICS, MINERALOGY AND GEOCHEMISTRY OF THE GİCİK LOW–SULFIDATION EPITHERMAL AU DEPOSIT (ANKARA PROVINCE, CENTRAL ANATOLIA)

submitted by **AKIN ÇİL** in partial fulfillment of the requirements for the degree of **Master of Science in Geological Engineering Department, Middle East Technical University** by,

Prof. Dr. Halil Kalıpçılar
Dean, Graduate School of **Natural and Applied Sciences** _____

Prof. Dr. Erdin Bozkurt
Head of Department, **Geological Engineering** _____

Assist. Prof. Dr. Ali İmer
Supervisor, **Geological Engineering, METU** _____

Examining Committee Members:

Prof. Dr. Erdin Bozkurt
Geological Engineering, METU _____

Assist. Prof. Dr. Ali İmer
Geological Engineering, METU _____

Assist. Prof. Dr. Fatma Toksoy Köksal
Geological Engineering, METU _____

Prof. Dr. Yurdal Genç
Geological Engineering, Hacettepe University _____

Assoc. Prof. Dr. Elif Varol Muratçay
Geological Engineering, Hacettepe University _____

Date: 11.09.2019

I hereby declare that all information in this document has been obtained and presented in accordance with academic rules and ethical conduct. I also declare that, as required by these rules and conduct, I have fully cited and referenced all material and results that are not original to this work.

Name, Surname: Akın Çİl

Signature:

ABSTRACT

SURFACE CHARACTERISTICS, MINERALOGY AND GEOCHEMISTRY OF THE GİCİK LOW–SULFIDATION EPITHERMAL AU DEPOSIT (ANKARA PROVINCE, CENTRAL ANATOLIA)

Çil, Akın
Master of Science, Geological Engineering
Supervisor: Assist. Prof. Dr. Ali İmer

September 2019, 138 pages

Tethyan-Eurasian Metallogenic Belt was formed as a result of the Mesozoic-Cenozoic Alpine-Himalayan orogeny related to the opening and closure of the Tethyan ocean basins. Turkey forms a sector of this extensive belt, and hosts numerous precious and base metal deposits. Gicik Au mineralization is located at Sakarya zone and approximately 15 km north of Ankara. Gold mineralization is hosted within Middle Eocene (ca. 44 Ma) intermediate composition dacitic lavas and agglomerates that are widely exposed near Ankara, and unconformably overlying the Paleozoic metamorphic basement. Whole-rock geochemical analyses of volcanic rocks indicate that the volcanism is metaluminous, medium-K calc-alkaline in composition and related to subduction and post-collisional tectonic setting. Lithogeochemical and geochronological data strongly implies that the studied volcanic rocks belong to the earlier (Eocene) eruptive volcanic event at the north of Ankara which was followed by volcanic rocks of Galatean Volcanic Province (Miocene). These volcanic lithologies are cut by NNE–trending 2 to 10 meters thick siliceous veins that display stockwork, colloform banding and superimposed breccia textures or less commonly bladed textures. Main ore minerals in the Gicik area includes argentiferous tetrahedrite, pyrite and arsenopyrite. Alteration assemblages include widespread

epidote-chlorite with less common calcite (propylitic), argillic (kaolinite-sericite/illite-smectite-quartz-adularia) and silicification. $^{40}Ar/^{39}Ar$ age data obtained from sericite in Gicik deposit yielded age of 45 – 47 Ma suggesting synchronous formation of volcanism and mineralized system. Central Anatolia is remained relatively underexplored when compared to the eastern and western parts of the Eocene magmatic belt across the north of İzmir-Ankara-Erzincan suture. Presence of Eocene volcanism related Gicik mineralization in central Anatolia puts entire magmatic belt in a position potential to especially precious metal mineralization.

Keywords: Central Anatolia, Ankara, Gicik, Cenozoic Volcanism, Low–Sulfidation Epithermal Gold

ÖZ

GİCİK DÜŞÜK-SÜLFİTLİ EPİTERMAL ALTIN YATAĞININ YÜZEY ÖZELLİKLERİ, MİNERALOJİSİ VE JEOKİMYASI (ANKARA, ORTA ANADOLU)

Çil, Akın
Yüksek Lisans, Jeoloji Mühendisliği
Tez Danışmanı: Dr. Öğr. Üyesi Ali İmer

Eylül 2019, 138 sayfa

Tetis-Avrasya Metallojenik Kuşağı, Tetis okyanusunun açılıp kapanması ile ilişkili Mezozoyik-Senozoyik Alp-Himalaya orojenisinin sonucu oluşmuştur. Türkiye bu geniş kuşağın bir bölümünü oluşturmakta olup sayısız kıymetli ve baz metal yataklarına ev sahipliği yapmaktadır. Gicik altın cevherleşmesi, Ankara şehir merkezinin yaklaşık 15 km kuzeyinde, Sakarya zonu içerisinde yer almaktadır. Altın cevherleşmesi, Paleozoyik metamorfik zemin kayaçlarını uyumsuz olarak üzerleyen ve Ankara civarında bolca yüzlek veren Orta Eosen (44.0 My) ortaç bileşimli dasitik lavlar ve aglomeralar içerisinde bulunmaktadır. Tüm-kayaç jeokimya sonuçlarına göre, cevherleşmeyi barındıran bu volkanik kayaçların metaalumina özellikli ortaç-K kalk-alkalen bileşiminde olup dalma-batma ve çarpışma sonrası tektonik ortamında oluştuğu ortaya konmuştur. Kayaç jeokimyası ve jeokronoloji verileri, bu kayaçların Ankara'nın kuzeyinde gözlemlenen volkanizmaya (Eosen) ait olduğu ve sonrasında Galatya Volkanik Bölgesi'ne ait volkanizma (Miyosen) ile takip edildiğini göstermektedir. Bahsedilen kayaçlar NNE uzanımlı 2-10 metre kalınlığında olan ve ağsal, kolloform bantlaşma ve bunların üzerinde gelişen breş dokuları ve nadir bıçaksı dokular gösteren silisli damarlar tarafından kesilmiştir. Gicik bölgesinde bulunan ana cevher mineralleri gümüşlü tetraedrit, pirit ve arsenopirittir. Yaygın gözlenen epidot-

klorit ve daha nadir görülen kalsit (propilitik), arjilik (kaolinit-serizit/illit-simektit-quartz-adularya) ve silisleşme alterasyon tiplerini oluşturmaktadır. Serizit minerallerinden yapılan $^{40}Ar/^{39}Ar$ analizi sonuçları Gicik yatağının yaşını 45 - 47 My olarak vermis olup, volkanizma ve cevherleşmenin eş zamanlı olduğunu ortaya koymuştur. Orta Anadolu, İzmir-Ankara-Erzincan Kenet Kuşağının kuzeyinde yer alan Eosen magmatik kuşağın doğu ve batı kısımlarına görece daha az çalışılmıştır. Orta Anadolu'da yer alan Eosen volkanizması ile ilişkili Gicik cevherleşmesinin varlığı tüm magmatik kuşağı özellikle kıymetli metaller açısından potansiyel bir bölge konumuna getirmiştir.

Anahtar Kelimeler: Orta Anadolu, Ankara, Gicik, Senozoyik Volkanizması, Düşük-Sülfitli Epitermal Altın

To my parents…

ACKNOWLEDGEMENTS

I would like to express my deepest gratitude to my supervisor, Assist. Prof. Dr. Ali İmer, for his invaluable guidance, everlasting patience, and encouragement throughout the course of this study. It would be impossible without his never-ending support starting from the beginning until the very end.

Also, I am grateful to the examining committee because of their constructive criticism and valuable suggestions to improve the quality of this work.

I wish to thank Assist. Prof. Dr. Fatma Toksoy Köksal for sharing her knowledge of clay mineralogy and mineral geochemistry. Her assistance during the preparation of microprobe samples should not be forgotten.

I would like to extend my thanks to Levent Tosun, Uğur Balcı and Meryem Dilan İnce for their aids during the field studies, and Alican Aktağ for discussions about interpretation of geochemical data.

Special thanks also go to Orhan Karaman, Gonca Alptekin Aynur Atak Küçük for their efforts during the preparation of polished thins sections, performing X-Ray Diffraction analyses and conducting Electron Microprobe Analyses, respectively.

This thesis could not have been written without the McKinstry Fund granted by Society of Economic Geologists (SEG). Special thanks to Koza Gold Company for their permission and support.

I am deeply grateful to my friends, Orkun Öztaşkın, Koray Bilasa, Emre Çetinkaya, Erkan İstanbulluoğlu, Burak Tuncal, Buğra Çavdar and for their advices and encouragements during the thesis writing process.

At last but not the least, I would like to express my very special thanks to my family for their trust, patience, guidance and financial support throughout my entire life. I would not be able to succeed without their inspiration.

TABLE OF CONTENTS

ABSTRACT v

ÖZ vii

ACKNOWLEDGEMENTS x

TABLE OF CONTENTS xi

LIST OF TABLES xv

LIST OF FIGURES xvi

CHAPTERS

1. INTRODUCTION 1

1.1. Purpose and Scope 1

1.2. Methodology 4

1.2.1. Fieldwork 5

1.2.2. Laboratory Studies 5

1.3. Epithermal Deposits: A Review 7

1.3.1. Introduction 7

1.3.2. Classification of Epithermal Deposits 8

1.3.2.1. High-Sulfidation Epithermal Deposits 13

1.3.2.2. Low-Sulfidation Epithermal Deposits 14

1.3.2.3. Intermediate-Sulfidation Epithermal Deposits 15

1.3.3. Epithermal Deposits of Turkey 17

1.4. Regional Geology 21

1.4.1. Pre-Cenozoic Tectonic Basement 21

1.4.2. Overview of Cenozoic Volcanism in Northern Ankara 26

1.4.2.1. Galatean Volcanic Province 27
1.5. Exploration History of Gicik 31
2. GEOLOGY OF THE GİCİK AREA 33
2.1. Introduction 33
2.2. Lithological Units 35
2.2.1. Andesitic-Dacitic Lava Flows and Agglomerates 37
2.2.1.1. Lower Agglomerate Unit 37
2.2.1.2. Massive Lava Flows and Agglomerate Intercalations 37
2.2.1.3. Upper Agglomerate Unit 40
2.2.1.4. Mineralogy of Intermediate Volcanic Rocks 40
2.2.2. Basaltic Lavas 50
2.3. Siliceous Veins 51
2.3.1. T Vein 55
2.3.2. Q Vein 55
2.3.3. East Veins 57
2.3.4. G Vein 60
2.3.5. Creek Vein 61
2.4. Structure 63
3. LITHOGEOCHEMISTRY 67
3.1.1. Major Element Geochemistry 69
3.1.2. Trace Element Geochemistry 72
3.1.3. Tectonic Discrimination Diagrams 73
4. MINERALIZATION AND HYDROTHERMAL ALTERATION 77
4.1. Mineralization 77

4.1.1. Ore Mineralogy....77
4.1.2. Hydrothermal Alteration....81
4.1.2.1. Timing of Hydrothermal Alteration....87
5. DISCUSSIONS....91
5.1. Nature and Tectonic Setting of Gicik Volcanism....91
5.2. Formation of Gicik Low-Sulfidation Epithermal System....94
5.3. Potential Implications for Regional Metallogeny....96
6. CONCLUSIONS....99
REFERENCES....101
APPENDICES
A. Compositional Data from Hornblende Phenocrysts....115
B. Compositional Data from Biotite Phenocrysts....117
C. Compositional Data from Plagioclase Phenocrysts....119
D. Compositional Data from magnetite Phenocrysts....121
E. Compositional Data from Ilmenite Phenocrysts....123
F. Hydrothermal Vein Textures....125
G. Paleostress Reconstruction Results....127
H. Sense of Movement on the Fault Surfaces....129
I. Compositional Data from Pyrite and Arsenopyrite Minerals....131
J. Compositional Data from Tetrahedrite Minerals....133
K. XRD Analyses Results of Samples GCK-14 (497261E, 4429301E) and GCK-15 (497262E, 4429292N)....135
L. $^{40}Ar/^{39}Ar$ Analyses Results of Samples 542639 and 661564....137

LIST OF TABLES

TABLES

Table 1.1. Field-oriented characteristics of each subtype of epithermal deposits (Simplified from Sillitoe and Hedenquist, 2003). 12
Table 1.2. Some important gold deposits/prospects of Turkey as reserve and/or resource (resource data from Yiğit, 2006 and 2009; Baker, 2019). 21
Table 2.1. Representative EPMA compositions of hornblende (hb) and biotite (bt) from least-altered volcanic rock samples from Gicik. All values are reported in wt%. 48
Table 2.2. Representative EPMA compositions of plagioclase phenocrysts from least-altered volcanic rock samples from Gicik. All values are reported in wt%. 48
Table 2.3. Representative EPMA compositions of magnetite microphenocrysts from least-altered volcanic rock samples from Gicik. All values are reported in wt%. 49
Table 2.4. Representative EPMA compositions of ilmenite microphenocrysts from least-altered volcanic rocks samples from Gicik. All values are reported in wt%. ...49
Table 2.5. Summary of the veins in terms of textures and ore mineralogy 54
Table 2.6. Summary of fault surface data from Gicik area. 65
Table 3.1. Whole-rock geochemical data of least-altered and altered intermediate composition volcanic rock samples from Gicik. 67
Table 4.1. Mineral geochemistry results of pyrite (py) and arsenopyrite (apy). All values are reported in wt%. 80
Table 4.2. Representative EMPA compositions of tetrahedrites from Gicik. All values are reported in wt%. 81
Table 4.3. $^{40}Ar/^{39}Ar$ age of the sericite minerals from Gicik altered rocks (personal communication with İlkay Kuşcu, unpublished data). 88

LIST OF FIGURES

FIGURES

Figure 1.1. Location map of the study area (modified from MTA 1:25.000 scale geological maps). Gicik lies on the Eocene volcanic rocks near Ankara. Inset map indicates the distribution of Cenozoic Volcanism around Turkey and related epithermal system in Central Anatolia. 3

Figure 1.2. Cross-section representing the Earth's crust. Epithermal deposits are strongly correlated with oceanic and continental arc settings at depths of generally <500 meters or less commonly within 1–2 kilometers (Groves et al., 1998; Goldfarb et al., 2005). 8

Figure 1.3. Schematic sections of end-member volcanotectonic settings and associated epithermal mineralization types. a) High- and intermediate-sulfidation epithermal deposits formed at calc-alkaline volcanic arc with neutral to mildly extensional stress state. b) Low-sulfidation deposits formed at rift with bimodal volcanism (Sillitoe and Hedenquist, 2003)..... 11

Figure 1.4. Typical alteration zonation in high-sulfidation epithermal systems (Stoffregen, 1987; Arribas, 1995)..... 14

Figure 1.5. Alteration, textures, ore and gangue mineralogy in typical low–sulfidation epithermal vein deposits (Buchanan, 1981 and Sillitoe, 1993). 16

Figure 1.6. The Tethyan metallogenic belt showing approximate traces of Paleo- and Neotethyan suture zones locations of major porphyry and epithermal deposits (Richards, 2015). 19

Figure 1.7. Map showing distribution of major epithermal mineralizations in Turkey. 20

Figure 1.8. Paleogeography of the Neotethys ocean basin when it reached its maximum extent in the Late Jurassic (modified from Scotese, 2007). 23

Figure 1.9. Paleogeographic reconstructions of Anatolia and its neighboring regions between 150 and 25 Ma as obtained from the Ocean Drilling Stratigraphic Network's Plate Tectonic Reconstruction Service (www.odsn.de/odsn/services/paleomap/paleomap.html). Abbreviations: A: Afghan Block; C: Carpathians; CI: Central Iranian Block; Is: Istanbul Zone; K: Kırşehir Block; L: Lut Block; M: Moesian Platform; P: Pontides; R: Rhodopes; SA: South Armenian Block; Sk: Sakarya Zone; SSZ: Sanandaj-Sirjan Zone; TAB: Tauride-Anatolide Block. 24

Figure 1.10. Map showing the major tectonic units and suture zones of Turkey (Okay and Tüysüz, 1999). IAESZ: İzmir-Ankara-Erzincan Suture Zone; RSZ: Rhodope-Strandja Zone; BFZ; Bornova Flysch Zone. 26

Figure 1.11. Map of Turkey showing distribution of the Cenozoic–Quaternary volcanic activity throughout Turkey and taken from MTA 1:25.000 geological maps (WAVP: Western Anatolian Volcanic Province; GVP: Galatean Volcanic Province; CACC: Central Anatolian Crystalline Complex; EAVP: Eastern Anatolian Volcanic Province; KVP: Karacadağ Volcanic Province). 28

Figure 1.12. Regional tectonic setting of Central Anatolia (Koçyiğit et al., 1995). AFFZ: Ankara forced fold zone; AITFZ: Ankara imbricate thrust fault zone; GVC: Galatean Volcanic Complex; IAESZ: İzmir-Ankara-Erzincan Suture Zone; KB: Kırşehir Block; ATB: Anatolide-Tauride Block; NATF: North Anatolian Transform Fault Zone; RSZ: Rhodope-Strandja Zone; SC: Sakarya Continent; SLFZ: Lake Tuz Fault Zone; A: Ankara; G: Gicik. 30

Figure 2.1. Geological map of Ankara region (Rojay, 2013). Lithologies are based on MTA 1:25.000 scale maps. Points on the map indicates age data: 1) 45.31 Ma, 2) 44.5 and 44.7 Ma, 3) 46.95 Ma, 4) 42.0 and 41,7 Ma, 5) 44.8 Ma and 6) 43.2 Ma. 34

Figure 2.2. View from Koza drill site just south of Gicik towards Huseyingazi Hill to the south (UTM Coordinates 497375 E, 4428678 N). 35

Figure 2.3. Detailed outcrop geology map of the Gicik area. White areas are agricultural field where there is no outcrop exposed. 36

Figure 2.4. Lower agglomerate and massive lavas cross-cut by G and East veins south of Gicik (UTM Coordinates 497103 E, 4428360 N). Note the approximate N-S trend in massive lava flows. 38
Figure 2.5. The contact between lower agglomerate and massive lava flows (UTM Coordinates 497251 E, 4428500 N). 39
Figure 2.6. Contact between the lower agglomerate unit and pinkish colored massive lava flows (UTM Coordinates 497532 E, 4428656 N). 39
Figure 2.7. Field photographs of the upper agglomerate unit. a) outcrop from the Akdoğan Hill. Note the presence of pink colored massive andesitic boulders within the gray andesitic matrix (UTM Coordinates 498782 E, 4431414 N) b) outcrop from creek at the East of the road (UTM Coordinates 498000 E, 4431875 N). 41
Figure 2.8. Resistant silicified outcrops towards south of Akdoğan Hill (looking east; UTM Coordinates 497783 E, 4431620 N). 42
Figure 2.9. Microphotographs of hornblende (hb) and biotite (bt) in volcanic rocks around Gicik area a) euhedral hornblendes with highly developed cleavage planes (Sample GCK-12, PPL), b) slightly opacitized euhedral hornblende (Sample GCK-12, PPL), c) euhedral biotite and completely opacitized hornblende (Sample GCK-09, PPL), and d) euhedral hornblende and biotite lying inside groundmass (Sample GCK-12, PPL). 43
Figure 2.10. Microphotographs of biotite (bt) in volcanic rocks around Gicik area a) subhedral biotite lying in groundmass (Sample GCK-01, PPL), b) euhedral biotite in volcanic rock (Sample GCK-12, PPL), c) subhedral biotite crystals with slightly oxidized rims (Sample GCK-12, PPL), and d) biotite crystal with tiny opaque crystals which are Fe-Ti oxide crystals formed due to crystal-melt reaction during cooling and crystallization of magma (Sample GCK-37, PPL). 45
Figure 2.11. Microphotographs of plagioclase feldspar (plg) in volcanic rocks around Gicik area a) representative appearance and texture of dacitic lava flows. Porphyritic texture is represented by plagioclase feldspar, biotite (bt) and quartz (qtz) phenocrysts set in finer-grained groundmass of plagioclase microlites (Sample GCK-09, XPL), b) plagioclase phenocrysts showing polysynthetic twinning forming cumulates with

quartz and hornblende phenocrysts (Sample GCK-36, XPL), c) plagioclase feldspar grain displaying polysynthetic twinning and compositional zoning (Sample GCK-01, XPL), and d) melt inclusions clustered in the compositional zones of plagioclase phenocryst (Sample GCK-04, PPL). 46
Figure 2.12. Microphotographs of a) quartz (qtz) phenocryst displaying embayed texture (Sample GCK-37, XPL) and b) EPMA back scattered image of light gray colored magnetite (mt) with dark gray colored ilmenite (ilm). Ilmenite is both found as phenocrysts (ilm) and exsolution lamellae (ilm ex.) (Sample GCK-01). 47
Figure 2.13. Field photograph of basalt unit exposed at the roadcut towards the southeastern border of the study area (499138E, 4426917N). 50
Figure 2.14. Microphotograph of basalt sample with quartz phenocrysts forming glomeroporphyritic texture. Note the high birefringence epidote developed on feldspar phenocryst (Sample GCK-10, XPL). 51
Figure 2.15. Various textures and minerals observed within the Gicik vein system; a) Gray colored rhombohedral tetrahedrite intergrown with pyrite (not visible in this image) in colloform banded silica from G Vein (Sample GCK-64-2), b) dark colored silicified andesite with pyrite from East Vein (Sample GCK-61), c) colloform banded milky quartz with late amethystic quartz (purple) from southernmost part of Q2 Vein (Sample GCK-54), d) hydrothermal breccia with colloform bands consisting of quartz-pyrite from Q1 Vein (Sample GCK-38). 52
Figure 2.16. Typical vein textures from the Gicik vein system; a) and b) hydrothermal breccia from (Q Vein), c) colloform banding and cockade texture (G Vein), d) lattice bladed texture (Q Vein), e) drusy quartz (Q vein), and f) massive quartz (G Veins). 53
Figure 2.17. Field photograph of T Vein exposed near Taştepe Hill to the north of Gicik (497496E, 4430126N). 56
Figure 2.18. Field photograph of contact between argillized agglomerate and siliceous vein observed in the Q1 Vein at the north of Gicik Village (UTM Coordinates 497249 E, 4429198 N). Arrow indicates the decreasing intensity of argillic alteration. 57

Figure 2.19. Field photograph of the Q2 Vein cross-cutting agglomerate and forming intense clay alteration (white color) (UTM Coordinates 497035 E, 4428873 N). 58
Figure 2.20. Field photograph of NW dipping (~70°) East 1 vein in the field (UTM Coordinates 497711 E, 4429129 N). 59
Figure 2.21. Field photograph of the NE–SW trending East2 Vein in the field (UTM Coordinates 497809 E, 4428866 N). 60
Figure 2.22. Outcrop images of the best exposed section of the NE-SW trending G Vein. a) Northern segment of G Vein exposed immediately to the south of Gicik village (UTM Coordinates 497333 E, 4428844 N), b) southern segment of the G Vein. Dark brown colored center is dominated by dark gray silicified zone, with disseminated pyrite, cut by thin, white colored quartz veinlets (UTM Coordinates 497389 E, 4428585 N)..... 62
Figure 2.23. Paleostress reconstruction analysis results and their spatial distribution in Gicik. 64
Figure 2.24. Oblique dextral fault with reverse component on the Q1 Vein located near the Gicik Village (UTM Coordinates 497248 E, 4429198 N). Paleostress reconstruction indicates compression along northeast–southwest direction. 65
Figure 3.1. Plots of the least-altered and altered Gicik samples on the $Al_2O_3/CaO+Na_2O+K_2O$ versus Al_2O_3/Na_2O+K_2O diagram (Shand, 1943). Data for comparison with regional volcanic systems are from (1) Seyitoğlu and Büyükönal (1995), (2) Tankut et al. (1998) and (5) Tankut (1985). 70
Figure 3.2. Plots of the least-altered and altered samples from Gicik on rock classification diagrams. a) Total alkali versus silica diagram (Le Bas et al., 1968), b) total alkali (Na_2O+K_2O)-$FeO_{(t)}$-MgO diagram (Irvine and Baragar, 1971). 71
Figure 3.3. Plots of the least-altered and altered volcanic rocks from Gicik on K_2O versus SiO_2 diagram (Peccerillo and Taylor, 1976). 71
Figure 3.4. Harker variation diagrams for the major elements in the Gicik intermediate rocks. Reference data are from (1) Seyitoğlu and Büyükönal (1995) and, (3) Besbelli and Varol (2002). All values are in wt%. 72

Figure 3.5. Primitive mantle-normalized multi–element diagram of volcanic samples. Normalization values are from Sun and McDonough (1989). 74
Figure 3.6. C1 Chondrite-normalized rare earth element diagram of volcanic samples. Normalization values are from Sun and McDonough (1989). 74
Figure 3.7. Plots of the Gicik samples on the Ti versus Zr tectonic discrimination diagram (Pearce, 1982). 75
Figure 3.8. Plots of least-altered and altered igneous rocks from Gicik on tectonic discrimination diagrams. a) Ta versus Yb diagram (Pearce et al., 1984), b) Nb versus Y diagram (Pearce et al., 1984), c) Rb/30-Hf-3Ta trivariate diagram (Harris et al., 1986). 76
Figure 4.1. Microphotographs of a) oxidized pyrite (py; center) with pyrite (left; Sample GCK-38, reflected light), b) pyrite and arsenopyrite (apy; Sample GCK-61, reflected light) and c) argentiferous tetrahedrite mineral (tet) partially oxidized into digenite (dig) along microfractures (Sample GCK-64-2, reflected light). 78
Figure 4.2. Ore minerals of Gicik epithermal system: a) close-up view of tetrahedrite in colloform banded sample from G Vein (Sample GCK-64-2), b) microphotograph of large euhedral tetrahedrite grain (Sample GCK-64-2, reflected plane polarized light), c) close-up view of disseminated pyrite and arsenopyrite in silicified volcanic wall-rock (Sample GCK-61), d) microphotograph of pyrite in silicified wall-rock (Sample GCK-61, reflected plane polarized light), e) close-up view of colloform banding (Sample GCK-32-A), and f) microphotograph of colloform banded quartz-pyrite (Sample GCK-32-A, PPL). 79
Figure 4.3. Hand specimens of altered samples; a) epidote-chlorite-carbonate altered agglomerate (Sample GCK-35), b) epidote-chlorite-carbonate alteration (Sample GCK-10), c) argillic-altered (quartz-clay) volcanic rock with Fe-oxides after pyrite oxidation (Sample GCK-27), and d) argillic-altered (clay) volcanic rock (Sample GCK-24). 83
Figure 4.4. Hand specimens of altered samples. a) slightly argillized volcanic rock (Sample GCK-20), b) argillic alteration (Sample GCK-44-A), c) silicified

agglomerate (Sample GCK-44-B) and d) silicified agglomerate (Sample GCK-40). 84
Figure 4.5. Microphotographs of vein textures a) hydrothermal breccia in quartz vein (Sample GCK-55, XPL), b) colloform banding surrounding silicified hydrothermal breccia (Sample GCK-49, XPL), c) siliceous vein showing paragenesis of earlier medium-grained massive quartz and pyrite bearing later fine-grained quartz (Sample GCK-32A, XPL), and d) pyrite within finer quartz changing into coarser barren quartz zone (Sample GCK-30, XPL). 85
Figure 4.6. Microphotographs of vein textures a) silicified vein with comb texture (Sample GCK-49, x4, XPL), b) quartz forming cockade texture (GCK-48, XPL), c) quartz veins cutting each other (Sample GCK-51, XPL) and d) quartz vein displaying lattice bladed texture (Sample GCK-66, PPL). 86
Figure 4.7. Hand specimen of Fe-(hydr)oxide-coated siliceous rock from Q1 Vein (UTM Coordinates 497249 E, 4429198 N). 86
Figure 4.8. Microphotographs of alteration minerals a) epidote and chlorite crystals formed after plagioclase mineral. Epidote has its characteristic pale-yellow color; on the other hand, chlorite has distinctive pale green color (Sample GCK-10, PPL), b) euhedral adularia formed in the colloform bands (Sample GCK-64-1, XPL), c) calcite formed as a result of epidote–chlorite (propylitic) alteration (Sample GCK-6, XPL) and d) sericite formed after plagioclase feldspar (Sample GCK-15, XPL). 87
Figure 4.9. $^{40}Ar/^{39}Ar$ spectra and inverse isochron plots of sericite from hydrothermally-altered samples 542639 (a and b) and 661564 (c). Sample locations and analytical are given in the text. (Data is from Kuşcu, unpublished). 89

CHAPTER 1

INTRODUCTION

1.1. Purpose and Scope

Anatolia is one of the oldest mining regions in the world with Anatolian mining and metallurgy dating back to at least 9th millennia B.C. The region is the birthplace of Bronze Age, and is also well known for its gold production since the ancient times. Lydians carried out placer gold mining along the Gediz (Pactolus) River around 560 B.C., particularly during the reign of King Croesus, whereas exposed gold deposits of hydrothermal origin have been exploited by many Anatolian civilizations including Trojans, Romans, and Ottomans (Kaptan, 1990).

In recent years the Turkish Mining Law was substantially modified to encourage foreign investment, which resulted in exploration and discovery of numerous gold deposits. As a consequence, Turkey now leads annual gold production among all European and Middle Eastern countries (Brown et al., 2019). Much of the gold endowment and production of Turkey are constituted by epithermal deposits and also partly by orogenic gold, gold-bearing porphyry and volcanic-hosted massive sulfide deposits (Yiğit, 2006, 2009; Baker, 2019; Oyman, 2019).

During the past three decades, many small- to medium-sized, and few world-class epithermal gold ± silver deposits have been discovered in western Anatolia (e.g., Efemçukuru, Ovacık, Çukuralan, Ağıdağı, Kirazlı, TV Tower), eastern Pontides (e.g., Cerattepe, Hot Maden, Taç, Çorak, Mastra) and eastern Anatolia (e.g., Çöpler). Almost all of these deposits are temporally and spatially associated with widespread Cenozoic volcanism and plutonism that developed during or after the closure of the Neotethyan ocean basins through continental subduction (Yiğit, 2009; Richards, 2015; Rabayrol et al., 2019). In fact, post-subduction magmatism, rather than typical

Andean-style subduction magmatism, is proposed as the major contributor to development of the most significant magmatic-hydrothermal deposits hosted in the aforementioned districts and also in other parts of the western Tethyan metallogenic belt such as in Iran, Pakistan, and Tibet (e.g., Wang et al., 2014; Richards, 2015; Richards and Sholeh, 2016).

Although Cenozoic volcanism was also quite active in central Anatolia, this region remained relatively underexplored for epithermal- and potentially linked porphyry-style mineralization. Most of the previously known epithermal deposits, clustered mainly near the Niğde Massif to the south of the Kırşehir Block (Figure 1.1), appear to be not economically feasible. However, the past decade has seen several important discoveries in other parts of central Anatolia, such as the Öksüt and Himmetdede deposits in Kayseri and the İnlice deposit near Konya (Figure 1.1). These three systems seem to lie on a young (Miocene) post-collisional metallogenic belt to the south of the Central Anatolian Crystalline Complex (Rabayrol et al., 2019; Figure 1.1), which had been unrecognized prior to the previous decade.

This thesis focuses on the Gicik vein-hosted epithermal Au deposit, located farther north of the south-central Anatolian Miocene belt, near Ankara (Figure 1.1). The Gicik epithermal system is exposed ~15 km north of Ankara city center, where a swarm of NNE-trending gold mineralized siliceous veins have been developed within Cenozoic volcanic units.

Epithermal-style gold mineralization at Gicik was first identified by Eurogold in late 1980s through surface sampling, detailed geological mapping, and geophysical surveys. Eurogold later tested the site through drilling of a total of 26 diamond holes totaling 2,436 meters. Following this, Koza Gold acquired the permits of the field and continued exploration, mainly conducted channel sampling and diamond drilling. The best intercepts yielded gold and silver grades of 45 g/t Au and 79 g/t Ag over one-meter intervals. In early 2000s, small-scale open-pit gold production took place at Gicik, where low-grade gold ore was processed at Mastra and Kaymaz mines. Koza

Gold still continues further diamond drilling and feasibility studies in the southern part of the Gicik town.

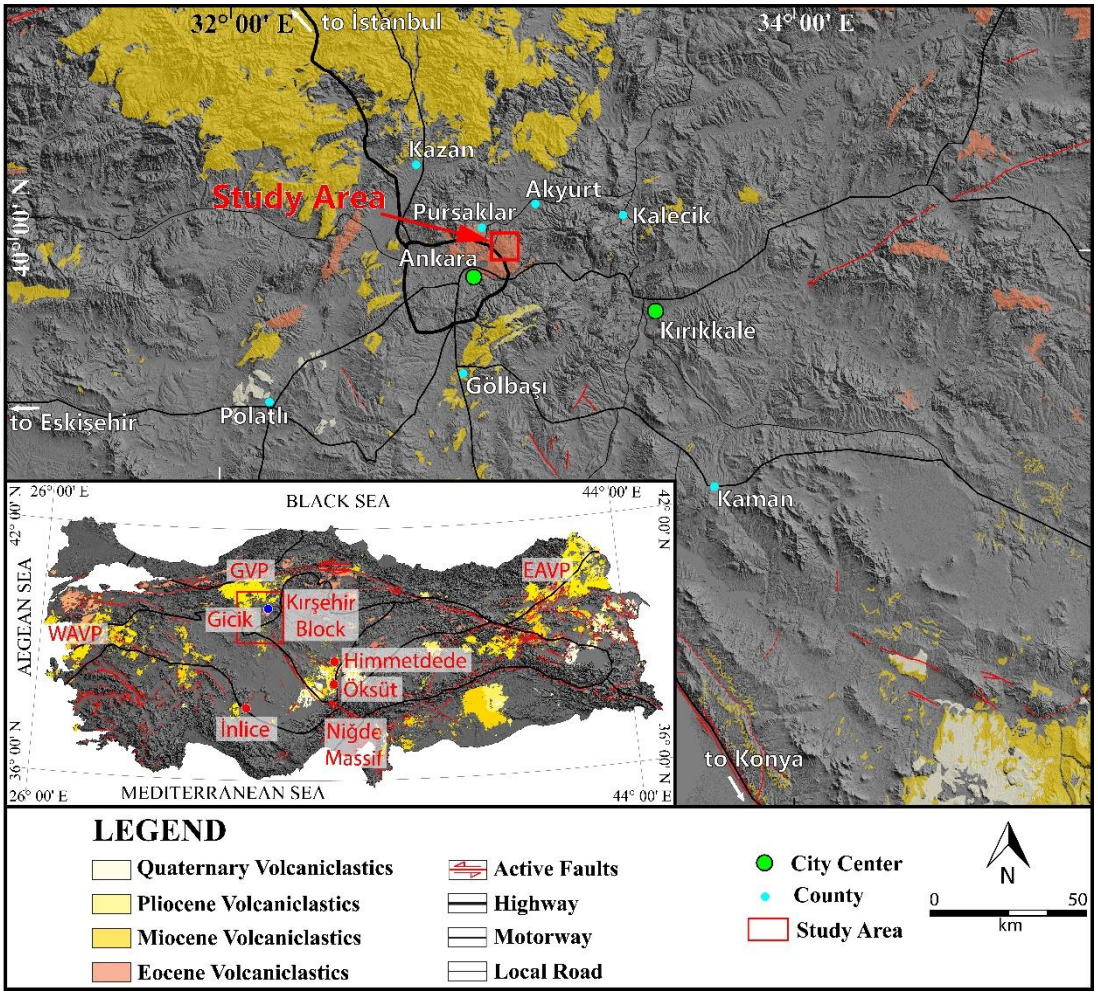


Figure 1.1. Location map of the study area (modified from MTA 1:25.000 scale geological maps). Gicik lies on the Eocene volcanic rocks near Ankara. Inset map indicates the distribution of Cenozoic Volcanism around Turkey and related epithermal system in Central Anatolia.

Only one study (Besbelli and Varol, 2002) is available in the literature focusing on the nature of volcanism and hydrothermal alteration/mineralization near Gicik and Kurtsivrisi areas (located 50 km NNE of Gicik); Besbelli and Varol (2002) reported

major oxide compositions of 5 least-altered and altered rock samples (including one vein sample) from Gicik, and conducted petrographic, mineralogic, and fluid inclusion investigations on a limited number of hydrothermally-altered/mineralized samples. Their study has shown that least-altered dacitic–andesitic wall-rocks are calc-alkaline in composition and wall-rock alteration is characterized by an assemblage of quartz, kaolinite, smectite and illite. Besbelli and Varol (2002) further concluded that the Gicik gold deposit was formed in relation to Miocene–Pliocene volcanic activity, from acidic hydrothermal solutions with temperatures between 240° and 140°C.

The significance of this thesis study lies mainly in two aspects. Firstly, Gicik is the most significant yet a relatively understudied epithermal system near Ankara and its geotectonic setting as well as the geological controls on its formation remain unclear. Secondly, characteristics of the gold-mineralizing hydrothermal system have not been constrained in detail. By addressing these two issues a geological model will be generated for the Gicik epithermal gold deposit, which is aimed to provide vectors to guide future exploration for similar mineralization styles in the same region.

The above-mentioned points will be addressed by means of lithological, structural, and alteration mapping, petrographic studies on least-altered volcanic host rocks and mineralized and altered samples representative of the epithermal system, and whole-rock geochemical analyses. Obtained results will be compared with data from other similar epithermal systems associated with Anatolian Cenozoic volcanism.

1.2. Methodology

This study involves two main research methods; field and laboratory studies. Field studies include preparation of geological and alteration mapping and systematic collection of surface samples. Collected samples are aimed to be analyzed during the laboratory studies in order to understand the mineralogical and geochemical characteristics of surrounding rocks, ore and gangue mineralogy and alteration assemblages of Gicik deposit via microscopical studies, X-Ray diffractometry, electron microprobe and whole-rock geochemical analyses.

1.2.1. Fieldwork

Fieldwork was completed between May 2018 and July 2019, with an aim to carry out geological mapping and sampling. Geological mapping studies included lithological, structural, and alteration mapping of the Gicik volcanic system and associated mineralized veins, mainly at the scale of 1:25.000. More detailed mapping, at the scale of 1:5.000, was conducted near exposed veins, in particular to highlight the changes in alteration, ore mineralogy and vein textures. A handheld GPS was used to delineate the boundaries between various lithological units as well as to determine the surface distribution of different alteration facies, whereas structural data (bedding, lineation, fault, etc.) was collected using a Brunton compass and a mobile application (eGEO Compass Pro).

Fieldwork also included surface sampling of least-altered and altered igneous lithologies, mineralized wall-rocks as well as sampling of vein exposures. A systematic sampling approach was utilized during sampling of the veins, whereby samples were collected along traverses perpendicular to the vein strike orientation to observe lateral variations in alteration and mineralization. Collected samples provided a basis for subsequent laboratory analyses that are described in Section 1.2.2.

1.2.2. Laboratory Studies

Laboratory studies including petrographic and X-ray diffractometry (XRD) analyses were carried out at the Geological Engineering Department, Middle East Technical University (METU). Polished thin sections from a total of 65 samples were prepared at the Thin Section Preparation Laboratory in Geological Engineering Department at METU, and petrographic investigations were performed using transmitted and reflected light polarized microscopes to highlight host rock mineralogy, ore and gangue mineral assemblages, ore textures, and alteration mineralogy and intensity.

Two altered samples were selected for XRD analysis in order to determine clay minerals associated with hydrothermal and alteration. Sample preparation and XRD analysis were done at the Clay Mineralogy and XRD Laboratories at METU. Selected

samples were ground into small fragments by using a geological hammer. Crushed fragments were further powdered using a by mechanical grinder and sieved below 170 mesh for random measurements. 10 gr of each sample in a 1 lt beaker measured and mixed with anti-coagulant Na-polyphosphate in order to prevent flocculation. Distilled water was added to fill the beaker completely and mixed with sample for several minutes and waited for 8 to 12 hours to separate clay and non-clay minerals. Clay sized material was left at suspension after 8 hours. Suspended material was separated from the precipitated material. Separation process was repeated multiple times until there was almost no suspended material in the distilled water. Collected clay-sized material were put into centrifuge to remove water, centrifuged clay sized material was mounted onto four thin slides. Further treatments on oriented slides were performed as air drying, heating at 300°C, 550°C and ethylene glycolated.

Electron probe micro analyses (EPMA) were employed to obtain compositions of primary magmatic mineral phenocrysts/microphenocrysts (such as amphibole, biotite, plagioclase, magnetite, ilmenite) in least-altered volcanic rocks, and also to accurately identify ore minerals (e.g., sulfides) in mineralized rocks under 20kV accelerating voltage, 20nA accelerating current and spot size light beam radius conditions. Compositions of various mineral species were measured by wavelength dispersive spectrometry (WDS) using a JEOL JXA-8230 electron microprobe at the Central Laboratories in METU.

Four least-altered and altered samples were submitted to Actlabs (Ontario, Canada) for whole-rock geochemical analyses. Major and trace element compositions were measured using the 4E-research analytical package, which includes a combination of inductively-coupled plasma (ICP), inductively-coupled plasma emission mass spectrometry (ICP-MS), and instrumental neutron activation analysis (INAA) methods. Accuracy for major elements is generally within 5 relative percent for major elements, and 10 relative percent for trace elements, as indicated by replicate analyses of certified standards.

1.3. Epithermal Deposits: A Review

1.3.1. Introduction

Epithermal deposits play a significant role in the world's production of gold by providing about 19% of the total gold reserves of all known gold deposit types (Lipson, 2014). Epithermal deposits are concentrated mainly along the late Mesozoic and Cenozoic subduction zones such as the Circum-Pacific Belt and the Tethyan-Eurasian Metallogenic Belt, and are seldom observed along regions of Paleozoic orogeny (e.g., White et al., 1995), possibly due to their low preservation potential (Cooke and Simmons, 2000).

Epithermal deposits were initially noticed by Emmons (1918) and later by Lindgren (1922), and were then included in the detailed mineral deposit classification of Lindgren (1933). These are typically found in spatial association with volcanic and volcanosedimentary sequences erupted in arc, back-arc or continental rift settings (Cooke and Simmons, 2000; John, 2001; Corbett, 2002; Sillitoe and Hedenquist, 2003; Groves and Bierlein, 2007; Figure 1.2). In contrary to the traditional deposit models, some epithermal systems (especially low- and intermediate-sulfidation varieties) may also be hosted in non-volcanic sequences, such as basement metamorphic lithologies or sedimentary sequences. Well-known examples of such systems in Turkey are the Efemçukuru and Himmetdede low-sulfidation epithermal Au deposits.

Epithermal deposits are distinctive from low-grade, high-tonnage porphyry deposits in that they are typically high-grade but relatively small-sized deposits. There are a few other characteristic features of epithermal deposits, perhaps the most notable is that they form at shallow depths (≤1 km) and the mineralization in most of the deposits is developed within the first 600 meters of the surface (Corbett, 2002; Simmons et al., 2005; Taylor, 2007), rendering these to be easy targets for both exploration and mining. At such shallow depths, epithermal deposits form from low temperature (100°–300°C) and usually low salinity (<5 wt.% NaCl equiv.; with the exception of

some intermediate-sulfidation deposits) hydrothermal fluids (Corbett, 2002; Simmons et al., 2005), and develop as typically vein- or breccia-style and less commonly as replacement-style or disseminated ore bodies (Cooke and Simmons, 2000; Simmons et al., 2005). In most cases, the surrounding rocks of epithermal deposits are older than the mineralization itself, however, this may not be valid in cases where the mineralization is occurred around active volcanic and hot spring environments (White and Hedenquist, 1990; Taylor, 2007).

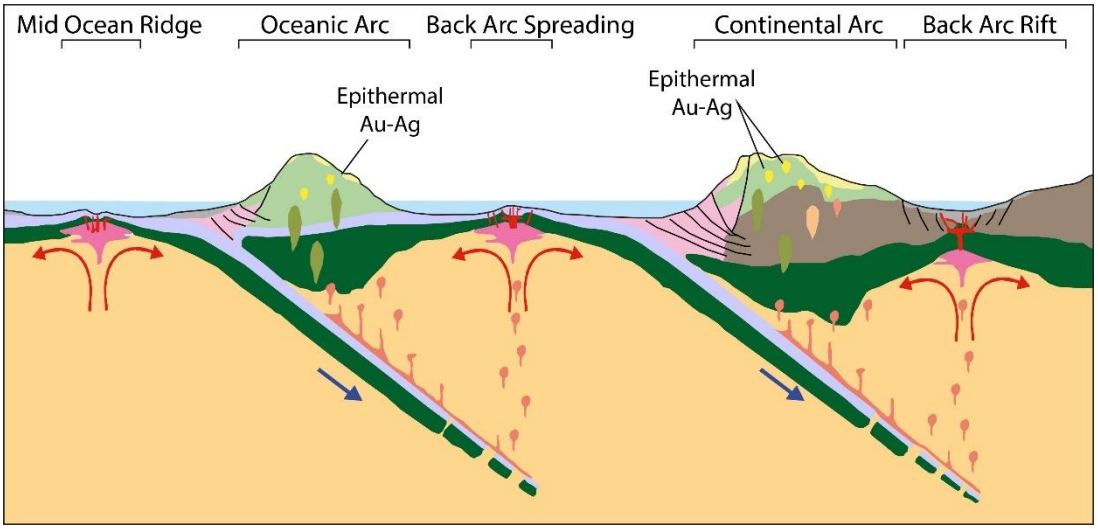


Figure 1.2. Cross-section representing the Earth's crust. Epithermal deposits are strongly correlated with oceanic and continental arc settings at depths of generally <500 meters or less commonly within 1–2 kilometers (Groves et al., 1998; Goldfarb et al., 2005).

1.3.2. Classification of Epithermal Deposits

Early studies revealed two end-member types of epithermal deposits, which develop under different geological conditions observed in diverse geological environments. The first of these is the result of highly oxidized and acidic magmatic fluids, which rapidly rise towards volcanic levels after derivation from magmas cooling and crystallizing at shallow depths. Such systems are described in the literature as "acid"

(Sillitoe, 1977), “enargite-gold” (Ashley, 1982), “high sulfur” (Bonham, 1986 and 1988), “acid-sulfate” (Hayba et al. 1985; Heald et al.1987), “alunite–kaolinite” (Berger and Henley, 1989), and more recently as “high-sulfidation” (Hedenquist, 1987; Hedenquist et al. 2000; Sillitoe and Hedenquist, 2003) epithermal deposits. High-sulfidation epithermal systems are typically hosted in volcanic rocks that have undergone intense advanced argillic alteration, silicification and/or minerals including alunite, kaolinite, pyrophyllite and diaspore, contains sulfide minerals such as covellite, pyrite and enargite, which are stable at high sulfur fugacity (f_{S_2}) conditions (Arribas, 1995; Simmons et al., 2005; Taylor, 2007; Figure 1.3).

The second end member is described in the literature as “alkalic” (Sillitoe, 1977), “hot-spring” (Giles and Nelson, 1982), “low sulfur” (Bonham, 1986 and 1988), “adularia-sericite” (Hayba et al. 1985; Heald et al., 1987; Berger and Henley, 1989) and “low-sulfidation” (Hedenquist, 1987; Hedenquist et al., 2000; Sillitoe and Hedenquist, 2003) and is characterized by lower oxidation levels, neutral or low acidity fluids which are commonly developed in the outer parts of the volcanic system and often post-dates magmatism (White and Hedenquist, 1990 and 1995; Simmons et al., 2005; Figure 1.3). Gold mineralization is predominantly accompanied by pyrite–arsenopyrite assemblage together with other ore minerals such as sphalerite, galena, tetrahedrite/tennantite, and chalcopyrite (White and Hedenquist, 1990, 1995). Proximal wall-rock alteration in low–sulfidation epithermal systems is characterized by quartz-adularia-sericite-carbonate alteration and silicification.

Sillitoe and Hedenquist (2003) described the most commonly used classification for epithermal deposits, and in addition to high- and low-sulfidation systems, intermediate-sulfidation systems have been proposed. Intermediate-sulfidation systems, which are transitional between the two end-members, are generally formed from hydrothermal fluids that are magmatic in origin similar to high-sulfidation systems, however, both ore (sphalerite, galena, chalcopyrite, tetrahedrite/tennantite) and gangue mineralogy (adularia, sericite, and carbonate) as well as alteration style in

intermediate-sulfidation systems are similar to that of low-sulfidation systems (Table 1.1).

It is concluded by the isotopic studies that the meteoric fluids play a dominant role in the formation of low-sulfidation systems, although magmatic fluids may contribute as well (Hedenquist and Lowenstern, 1994). Fluids react with the country rock and equilibrate, thereby resulting in reduced and near neutral fluid compositions (Giggenbach, 1992). As a result of this reaction, fluids mainly contain NaCl, CO_2 and H_2S which also controls the pH of the ore-transporting fluid. On the contrary, fluids forming high-sulfidation epithermal systems are derived from shallowly-degassing oxidized magmas. There is little or no equilibrium reaction between ascending fluids and country rock. This results in oxidized, hot and highly acidic fluids which contain HCl^- and SO^{2-} and cause intense leaching of the host rock (Henley et al., 1984).

In low-sulfidation systems, the principle controls on fluid pH are concentration of CO_2 and salinity in solution. Thus, boiling and loss of CO_2 to the vapor results in an increase in pH. Boiling is widely accepted as a critical mechanism for precipitation of gold, which is caused by a sudden drop in confining pressures as the fluid approaches to the surface. In high-sulfidation systems, mixing and dilution of hydrothermal fluid and ground water prevent boiling. Thus, boiling is not the sole mechanism for precipitation of gold and sulfides (Hedenquist et al., 2000). Acidic fluids ascending towards surface through an opening as discontinuity, fractures or faults. On its way, acidic fluids interact with surrounding rocks and form vuggy texture. This part corresponds to the central zone of alteration, and more neutral alteration minerals are formed away from this center.

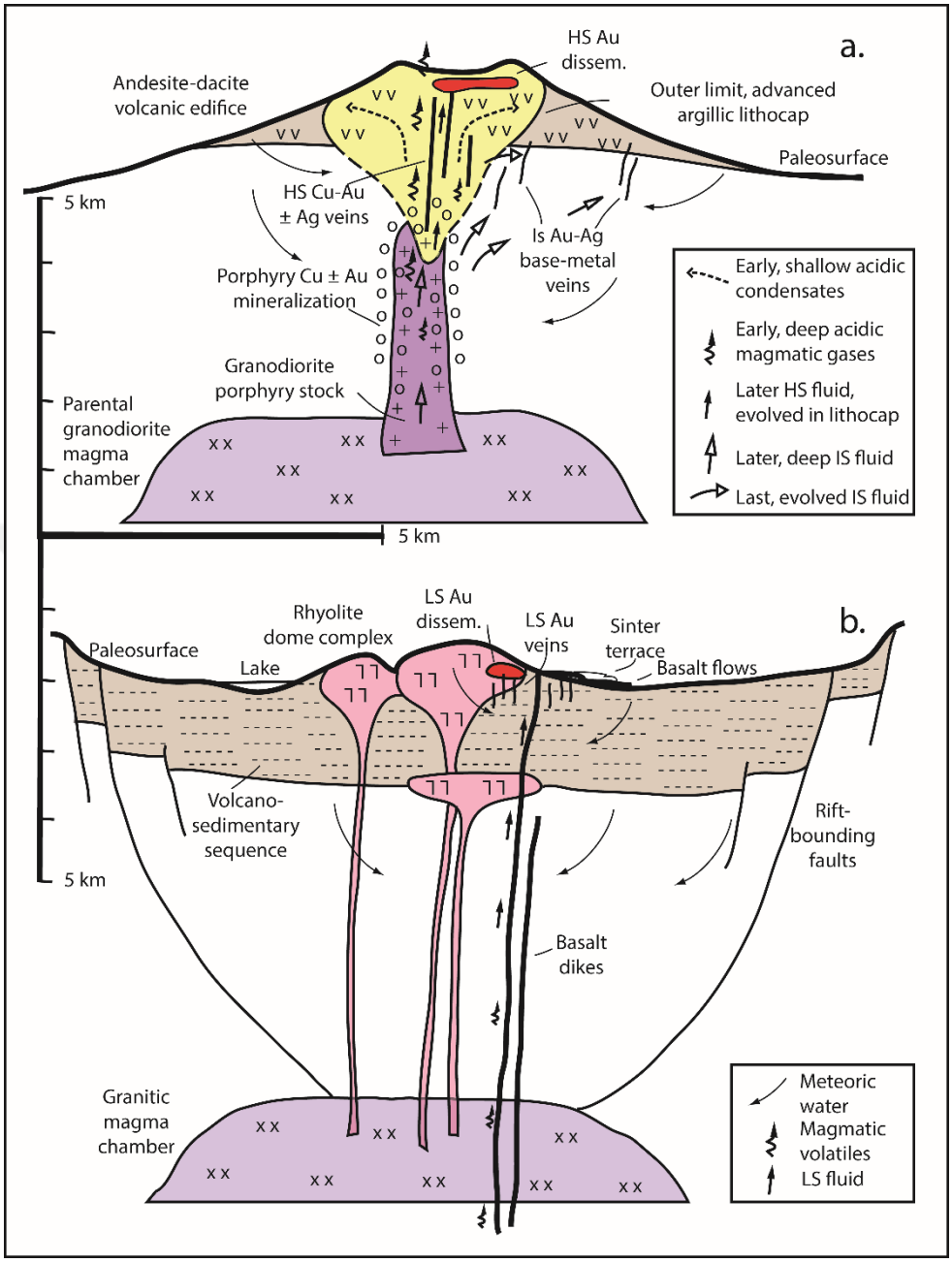


Figure 1.3. Schematic sections of end-member volcanotectonic settings and associated epithermal mineralization types. a) High- and intermediate-sulfidation epithermal deposits formed at calc-alkaline volcanic arc with neutral to mildly extensional stress state. b) Low-sulfidation deposits formed at rift with bimodal volcanism (Sillitoe and Hedenquist, 2003).

Table 1.1. Field-oriented characteristics of each subtype of epithermal deposits (Simplified from Sillitoe and Hedenquist, 2003).

	High Sulfidation		Intermediate Sulfidation	Low Sulfidation	
	Oxidized magma	Reduced magma		Subalkaline magma	Alkaline magma
Genetically related volcanic rocks	Mainly andesite to rhyodacite	Rhyodacite	Principally andesite to rhyodacite but locally rhyolite	Basalt to rhyolite	Alkali basalt to trachyte
Key proximal alteration mineral	Quartz-aluntite/APS; quartz-pyrophyllite/dickite at depth	Quartz-alunite/APS; quartz-dickite at depth	Sericite; adularia generally uncommon	Illite/smectite-adularia	Roscoelite-illite-adularia
Silica gangue	Massive fine-grained silicification and vuggy residual quartz		Vein-filling crustiform and comb quartz	Vein-filling crustiform and colloform chalcedony and quartz; carbonate-replacement texture	Vein-filling crustiform and colloform chalcedony and quartz; quartz deficiency common in early stages
Carbonate gangue	Absent		Common, typically including manganiferous varieties	Present but typically minor and late	Abundant but not manganiferous
Other gangue	Barite common, typically late		Barite and manganiferous silicates present locally	Barite uncommon; fluorite present locally	Barite, celestite, and/or fluorite common locally
Sulfide abundance	10-90 vol %		5->20 vol %	Typically <1-2 vol % (but up to 20 vol % where hosted by basalt)	2-10 vol%
Key sulfide species	Enargite, luzonite, famatinite, covellite	Acanthite, stibnite	Sphalerite, galena, tetrahedrite-tennantite, chalcopyrite	Minor to very minor arsenopyrite ± pyrrhotite; minor sphalerite, galena, tetrahedrite-tennantite, chalcopyrite	
Main metals	Au-Ag, Cu, As-Sb	Ag, Sb, Sn	Ag-Au, Zn, Pb, Cu	Au ± Ag	
Minor metals	Zn, Pb, Bi, W, Mo, Sn, Hg	Bi, W	Mo, As, Sb	Zn, Pb, Cu, Mo, As, Sb, Hg	
Te and Se species	Tellurides common; selenides present locally	None known but few data	Tellurides common locally; selenides uncommon	Selenides common; tellurides present locally	Tellurides abundant; selenides uncommon

APS = aluminum-phosphate-sulfate minerals

1.3.2.1. High-Sulfidation Epithermal Deposits

High-sulfidation epithermal deposits occur mainly in calc-alkaline andesitic-dacitic arc terranes, although locally felsic (i.e., rhyolitic) volcanic rocks can be genetically-related to the mineralization (Corbett, 2002; Sillitoe and Hedenquist, 2003).

High-sulfidation systems mostly display massive bodies of vuggy quartz and local veins and breccias. Highly acidic (pH<2; Stoffregen, 1987) hydrothermal fluids are responsible for the formation of vuggy texture by acid leaching, and these vugs prepare the ground for later fluid infill forming residual quartz and pyrite zones. Vuggy zones may be overprinted by massive to banded pyrite and enargite veins during late in the paragenesis (White and Hedenquist, 1995).

In high-sulfidation deposits, ore minerals like sphalerite are absent and arsenopyrite is scarce (White and Hedenquist, 1995). Rather, these contains copper-bearing sulfide and sulfosalt phases including covellite, chalcopyrite, bornite, chalcocite, and especially high-sulfidation state sulfosalts enargite and luzonite/famatinite (White and Hedenquist, 1995; Einaudi et al., 2003). Gangue minerals which are stable under relatively acidic conditions including kaolinite and alunite with pyrophyllite, diaspore and P-, Sr-, Pb- and REE-bearing aluminum phosphate–sulfate (APS) minerals commonly appear only in high-sulfidation deposits in relatively minor amounts (White and Hedenquist, 1995; Simmons et al., 2005; Figure 1.4).

High-sulfidation systems are formed as a result of oxidized and highly acidic hydrothermal fluids compared to low-sulfidation systems. Alteration minerals display zonation from leached silicic ore bearing vuggy quartz zone to advanced argillic quartz-alunite zone, kaolinite zone, illite-rich argillic zone, propylitic montmorillonite-rich zone, and chlorite-rich zone, respectively (Stoffregren, 1987; White and Hedenquist, 1995; Arribas, 1995).

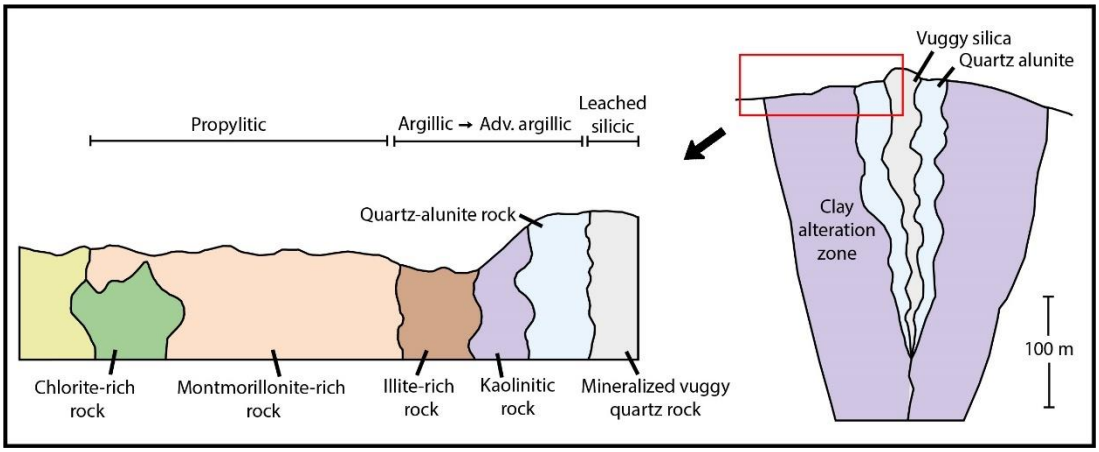


Figure 1.4. Typical alteration zonation in high-sulfidation epithermal systems (Stoffregen, 1987; Arribas, 1995).

1.3.2.2. Low-Sulfidation Epithermal Deposits

Low-sulfidation epithermal deposits are generally related with andesite-dacite-rhyolite arc terranes and bimodal basalt-rhyolite suites erupted at continental rift settings (White and Hedenquist, 1990). The rifts may develop in intra-, near-, and back-arc settings during subduction of oceanic lithosphere, post-arc settings following cessation of subduction and post-collisional settings (Sillitoe and Hedenquist, 2003).

Textures observed in the low-sulfidation systems are mainly banded and crustiform quartz and chalcedony veins, druse-lined cavities, multi-episodic vein breccias, bladed or lattice bladed calcite which later gets replaced by quartz as the system cools (Simmons and Christenson, 1994).

Low-sulfidation deposits are generally characterized by the common presence of pyrite, pyrrhotite, arsenopyrite, and Fe-rich sphalerite (Heald et al., 1987; Hedenquist et al., 2000). Cinnabar, stibnite, galena, tetrahedrite, realgar, and orpiment are other sulfide minerals typically observed in low-sulfidation epithermal systems (White and Hedenquist, 1995; Hedenquist et al., 2000; Einaudi et al., 2003; Figure 1.5). Gangue mineralogy of low-sulfidation epithermal deposits is characterized by minerals such

as sericite (illite), adularia, and calcite, which reflect near-neutral to slightly-acidic pH conditions of associated hydrothermal fluids (White and Hedenquist, 1995; Simmons et al., 2005; Figure 1.5), although argillic alteration zones characterized by illite, smectite, and kaolinite assemblages are also suggestive of relatively more acidic hydrothermal fluids.

Low-sulfidation epithermal systems are formed as a result of neutral and relatively less oxidized fluids and alteration mineralogy reflects these chemical properties. Where preserved (i.e., uneroded), low-sulfidation epithermal systems display well-developed alteration and mineralization zonation both vertically and horizontally (Buchanan, 1981; Hedenquist et al., 2000; Figure 1.5) starting from ore bearing veins as crustiform quartz/chalcedony-carbonates ± adularia ± barite/fluorite (argillic) to wall rock as sericite/illite ± adularia, smectite/mixed-layer clay ± chlorite and chlorite-carbonate ± epidote (propylitic) laterally. Textural and mineralogical zonation is also present in vertical direction. Gold grades are typically low near the surface and mineralization occurs as rare native gold or gold may be present in pyrite, whereas gold grades increase towards the deeper parts of the system (closer to the boiling level). Main sulfide assemblages of galena, sphalerite and chalcopyrite occupy the lower section of the system (Hedenquist et al., 2000). Thickness of the quartz vein decreases from top to bottom and eventually pinch out or may be replaced by small carbonate veins (Hedenquist et al., 2000).

1.3.2.3. Intermediate-Sulfidation Epithermal Deposits

Intermediate-sulfidation type epithermal deposits are related with calc-alkaline andesitic-dacitic magmatic arcs, post-collisional orogenic belts and back-arc settings (Hedenquist et al., 2000; Sillitoe and Hedenquist, 2003; Wang et al., 2019). They occur in geological environments where neutral to mildly extensional regime predominates, however, some exceptions of deposits occurred where compressional regime prevails (Sillitoe and Hedenquist, 2003).

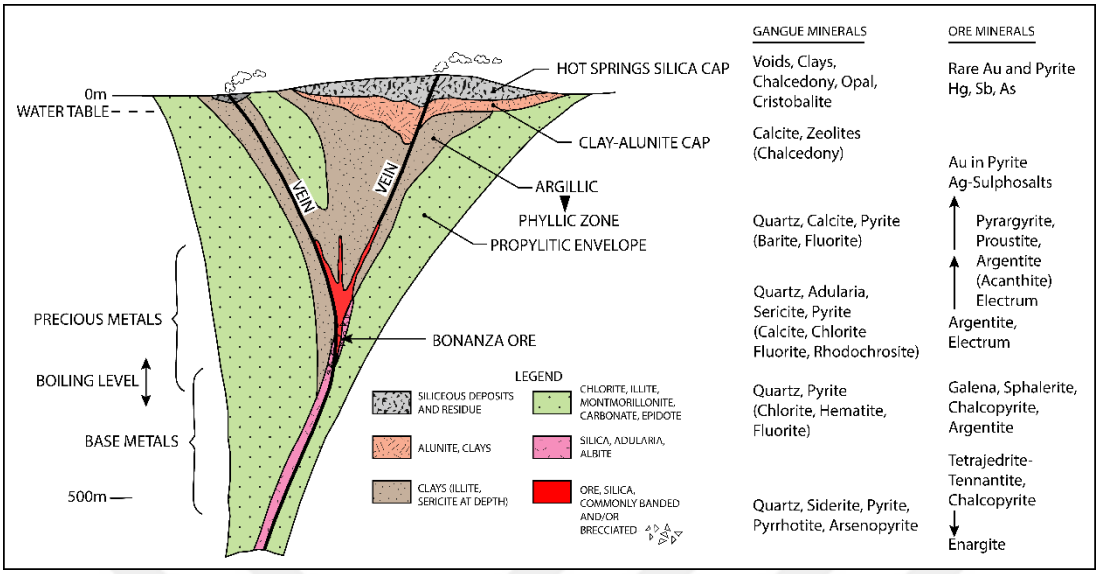


Figure 1.5. Alteration, textures, ore and gangue mineralogy in typical low–sulfidation epithermal vein deposits (Buchanan, 1981 and Sillitoe, 1993).

Intermediate-sulfidation systems may be related to deeply situated porphyry deposits, thus, can be distinguished from low-sulfidation systems.

Acidic, highly saline fluids (up to 23 wt.% NaCl equiv.; Sillitoe and Hedenquist, 2003; Simmons et al., 2005) are responsible for the formation of intermediate-sulfidation epithermal systems, which typically contain pyrite, Fe-poor sphalerite, galena, chalcopyrite, and tetrahedrite-tennantite as the main sulfide mineral assemblages (Hedenquist et al., 2000). Electrum, rare native gold, argentite and silver sulfosalt minerals exist in precious metal-rich intermediate-sulfidation epithermal deposits. This type of epithermal systems is generally characterized by lower Au grades when compared to the low-sulfidation end-member (Simmons et al., 2005). Quartz, Mn-carbonates and silicates (rhodochrosite and rhodonite), adularia, barite, and fluorite are the main gangue minerals in intermediate-sulfidation systems (Hedenquist et al., 2000; Sillitoe and Hedenquist, 2003).

1.3.3. Epithermal Deposits of Turkey

The Tethyan-Eurasian Metallogenic Belt (TEMB; Jankovic, 1977) was formed as a result of the Mesozoic–Cenozoic Alpine-Himalayan orogeny related to the opening and closure of the Neotethyan ocean basins. This belt, extending from southern Europe in the west to western Pacific in the east (Figure 1.6), is one of the world's richest metal producing belts (Richards, 2015). Turkey constitutes the part of the western sector of this extensive magmatic-metallogenic belt, and hosts numerous precious and base metal deposits (Figure 1.6). Turkish segment of the TEMB was mainly shaped by opening and by later ultimate closure of the Tethyan oceanic basins. Related tectonic events including rifting, subduction, and collision played a major role in shaping of the regional metallogeny especially during the Late Cretaceous to Cenozoic period (Richards, 2015). These mechanisms provided fertile magmatic activity which resulted in formation of important porphyry, epithermal, skarn/iron-oxide copper gold (IOCG), and volcanic-hosted massive sulfide (VHMS) deposits.

The Sakarya Zone of Pontides is a host to the majority of the known Turkish epithermal systems, which are mainly concentrated in two districts: the Biga Peninsula and the Eastern Pontide Belt. The Biga Peninsula in NW Turkey is the richest precious and base metal district in Anatolia, and not only contains a large number of Cenozoic-aged epithermal deposits/prospects (Table 1.2), but also several important porphyry deposits/prospects (e.g., Halilağa Cu-Au and Tepeoba Cu-Mo), and Pb-Zn and Fe skarn systems (e.g., Balya, Şamlı). Majority of the known significant epithermal systems at Biga are currently at advanced stages such as TV Tower, Ağı Dağı, Kirazlı, and Çamyurt HS epithermal systems, and Lapseki/Kestanelik and Küçükdere (both LS epithermal gold systems) are the only operating mines in the region. In addition, Kartaldağ HS and Madendağ LS epithermal systems near Çanakkale historically produced gold and are also being explored for additional mineralized zones.

Eastern Pontides is primarily known by its large endowment of VHMS deposits formed during the Late Cretaceous subduction of the northern Neotethys basin.

However, recent exploration work has demonstrated that this region is also potentially important for porphyry-, skarn-, and epithermal-style mineralization. The Mastra IS epithermal gold deposit has been actively mined since the 1990s, whereas Hot Maden, Sisorta, Taç, and Çorak (Figure 1.7) are other regionally important epithermal systems that are at advanced stages of exploration.

Eastern Taurides is another important but yet underexplored district containing epithermal-style deposits, but its full potential has not been completely tested yet. There are a few small deposits but other than these, the Eocene-aged Çöpler (Erzincan; Figure 1.7) deposit is currently known to contain the largest epithermal system in Turkey (Table 1.2). The Çöpler deposit contains an early, low-grade porphyry-style Cu-Au mineralization, and peripheral carbonate-replacement Cu-Au bodies, largely overprinted by intermediate-sulfidation epithermal-style Au mineralization (İmer et al., 2013; İmer, 2016).

Relatively less studied Central Anatolia region was exposed to multiphase compressional and extensional tectonism due to collision between Gondwana and Eurasian plates and associated tectono-magmatic events. These events produced a swath of NE–SW-trending post-collisional volcanic rocks between Kayseri in the east and Konya in the west during Neogene to Quaternary times. During this time period, intensive volcanism related to subduction and following collision between the Afro–Arabian and Eurasian plates in Central Anatolia generated a promising region for epithermal mineralization. Within this region, important epithermal systems (Öksüt, Himmetdede and İnlice) have been discovered recently. Discoveries of these systems emphasize the prospectivity of Central Anatolia in terms of epithermal-style mineralization.

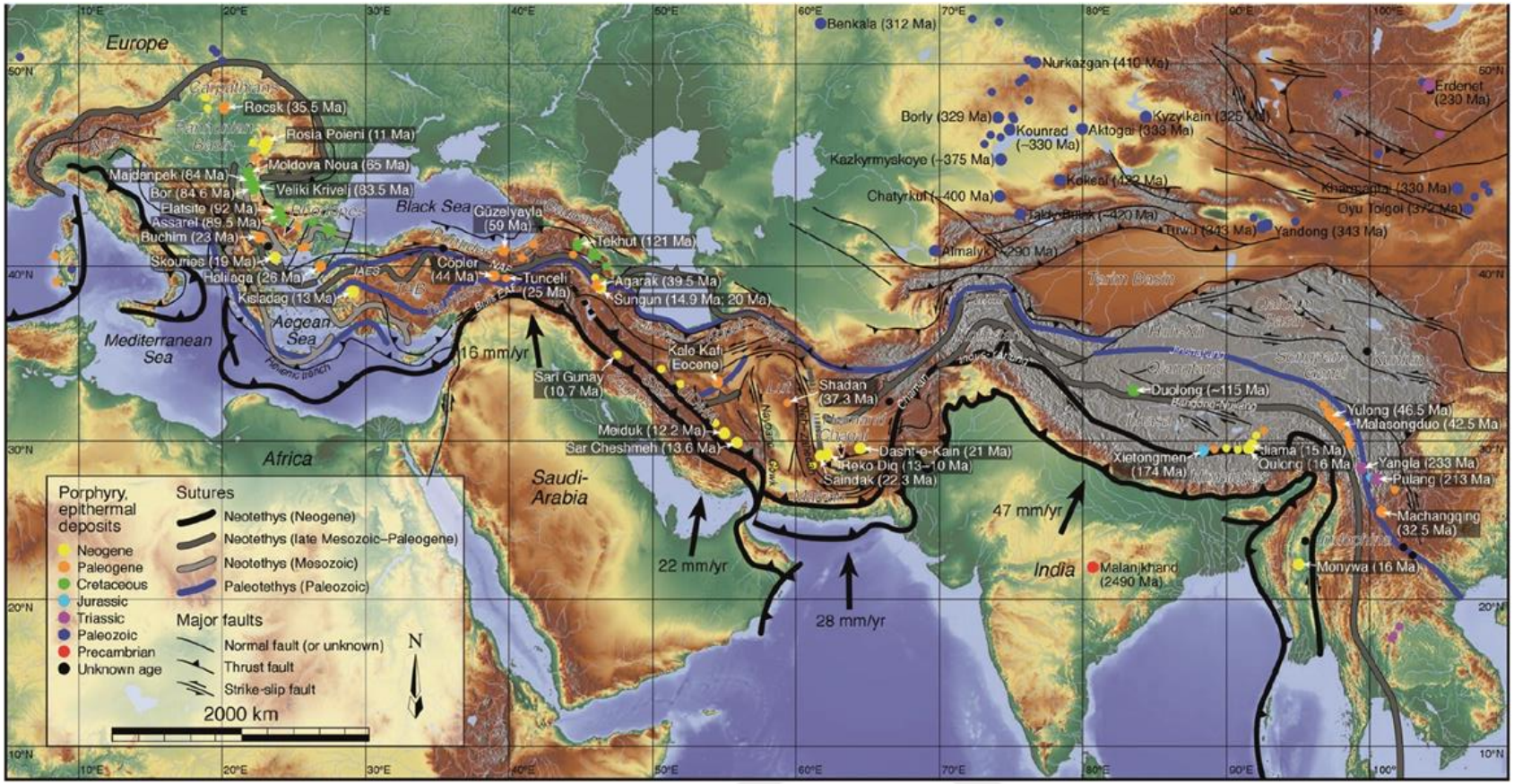


Figure 1.6. The Tethyan metallogenic belt showing approximate traces of Paleo- and Neotethyan suture zones locations of major porphyry and epithermal deposits (Richards, 2015).

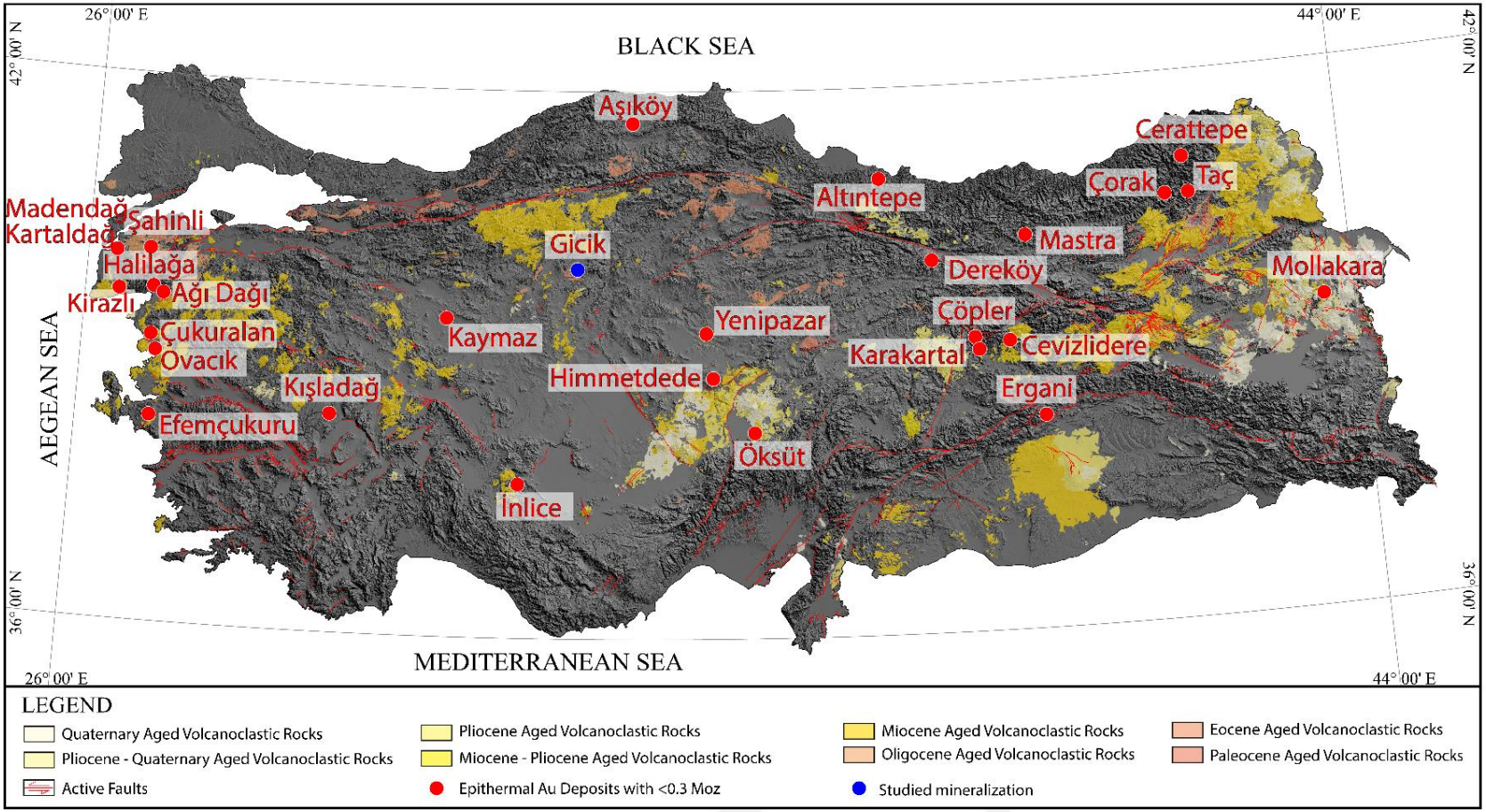


Figure 1.7. Map showing distribution of major epithermal mineralizations in Turkey.

Table 1.2. Some important gold deposits/prospects of Turkey as reserve and/or resource (resource data from Yiğit, 2006 and 2009; Baker, 2019).

Deposit Name	Province	Commodity	Total Au M oz	Total Au Tonnes	Status
Çöpler	Erzincan	Au	4,2	130,6	Development
Şahinli	Çanakkale	Au, Ag	2,05	63,7	Prospect
Efemçukuru	İzmir	Au	1,87	58	Development
Ovacık	İzmir	Au, Ag	1,54	47,9	Mine
Cerattepe	Artvin	Cu, Au, Ag	1,2	37,2	Development
Aşıköy	Kastamonu	Cu, Au, Ag	0,9	27,8	Mine
Çorak	Artvin	Au	0,58	18	Prospect
Ağı Dağı	Çanakkale	Au	0,58	18	Prospect
Taç	Artvin	Au	0,56	17,5	Prospect
Mastra	Gümüşhane	Au	0,43	13,5	Development
Madendağ	Çanakkale	Au	0,32	10	Prospect
Altıntepe	Ordu	Au	0,31	9,7	Prospect
Madenköy	Rize	Cu, Zn, Au, Ag	0,3	9,2	Mine
Küçükdere	Balıkesir	Au, Ag	0,29	9,1	Prospect
Tavşan	Kütahya	Au	0,29	9,1	Prospect
Gümüşhane	Artvin	Cu, Au, Mo	0,29	9	Prospect
Murgul	Artvin	Cu, Au	0,26	8	Mine
Kirazlı	Çanakkale	Au	0,25	7,8	Prospect
Lapseki	Çanakkale	Au, Ag	0,046	7,15	Mine
Himmetdede	Kayseri	Au, Ag	0,15	7,2	Mine
İnlice	Konya	Au	0,06	-	Development
Öksüt	Kayseri	Au	1,2	28,2	Mine

1.4. Regional Geology

1.4.1. Pre-Cenozoic Tectonic Basement

Turkey forms part of the Tethyside orogenic collage, which developed in response to the opening and demise of two prominent oceanic realms: the Paleotethys and Neotethys oceans. Situated between Gondwana in the north and Laurasia in the south

(Figure 1.8), these oceans strongly influenced the geology and hence the metallogeny of Anatolia (Şengör and Yılmaz, 1981; Göncüoğlu et al., 1996; Bozkurt and Mittwede, 2001; Yiğit, 2009; Richards, 2015). Timing and nature of closure (i.e., subduction polarity) of the Paleotethyan and Neotethyan ocean basins have been widely debated, however, it is generally accepted that Paleotethys existed during the Paleozoic–Early Mesozoic period and Neotethys existed during the Permian–Miocene interval. The Paleotethys ocean basin was progressively closed by convergence between Gondwana-derived Cimmerian continental fragments (including parts of present-day Turkey, Iran, and Tibet) and Laurentia, which resulted in opening of Neotethys ocean in the south during the Permian-Early Triassic and continuing to the Jurassic (Şengör and Yılmaz, 1981; Stampfli et al., 1991; Figure 1.8). Neotethys reached to its maximum extent during the Late Jurassic and started to close progressively after the initiation of drifting of Afro-Arabia fragments towards the north (Figure 1.9).

In general, the geological record relating to the Paleotethys ocean has been only poorly preserved in parts of Anatolia, and it is actually the Neotethys that predominates the major geological entities of this part of the Tethysides. Consequently, the relationship between Neotethys rifting, subduction, and closure cycles and Turkish metallogeny has been much better constrained overall (Yiğit, 2009; Richards, 2015; Kuşçu et al.,

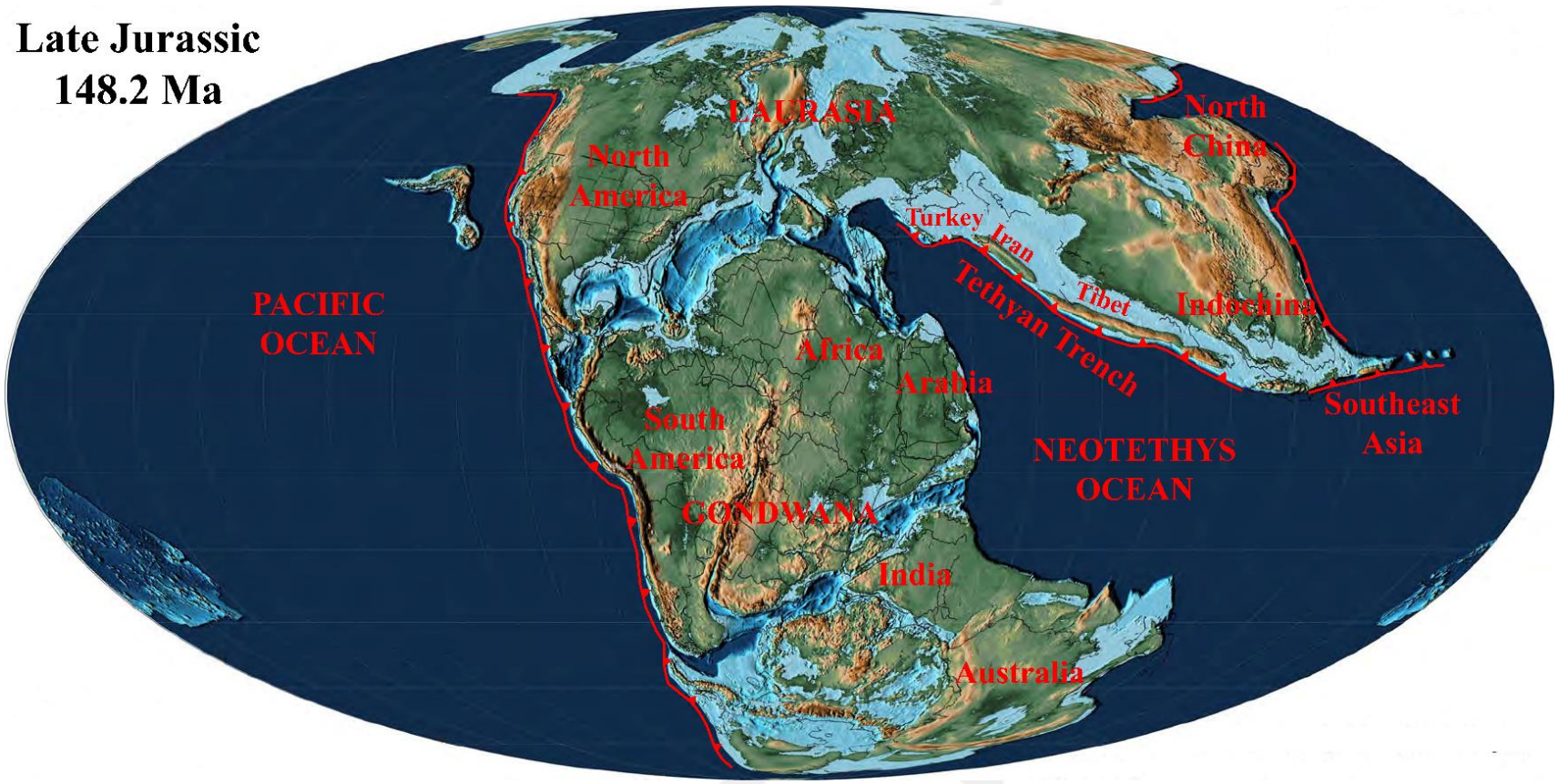


Figure 1.8. Paleogeography of the Neotethys ocean basin when it reached its maximum extent in the Late Jurassic (modified from Scotese, 2007).

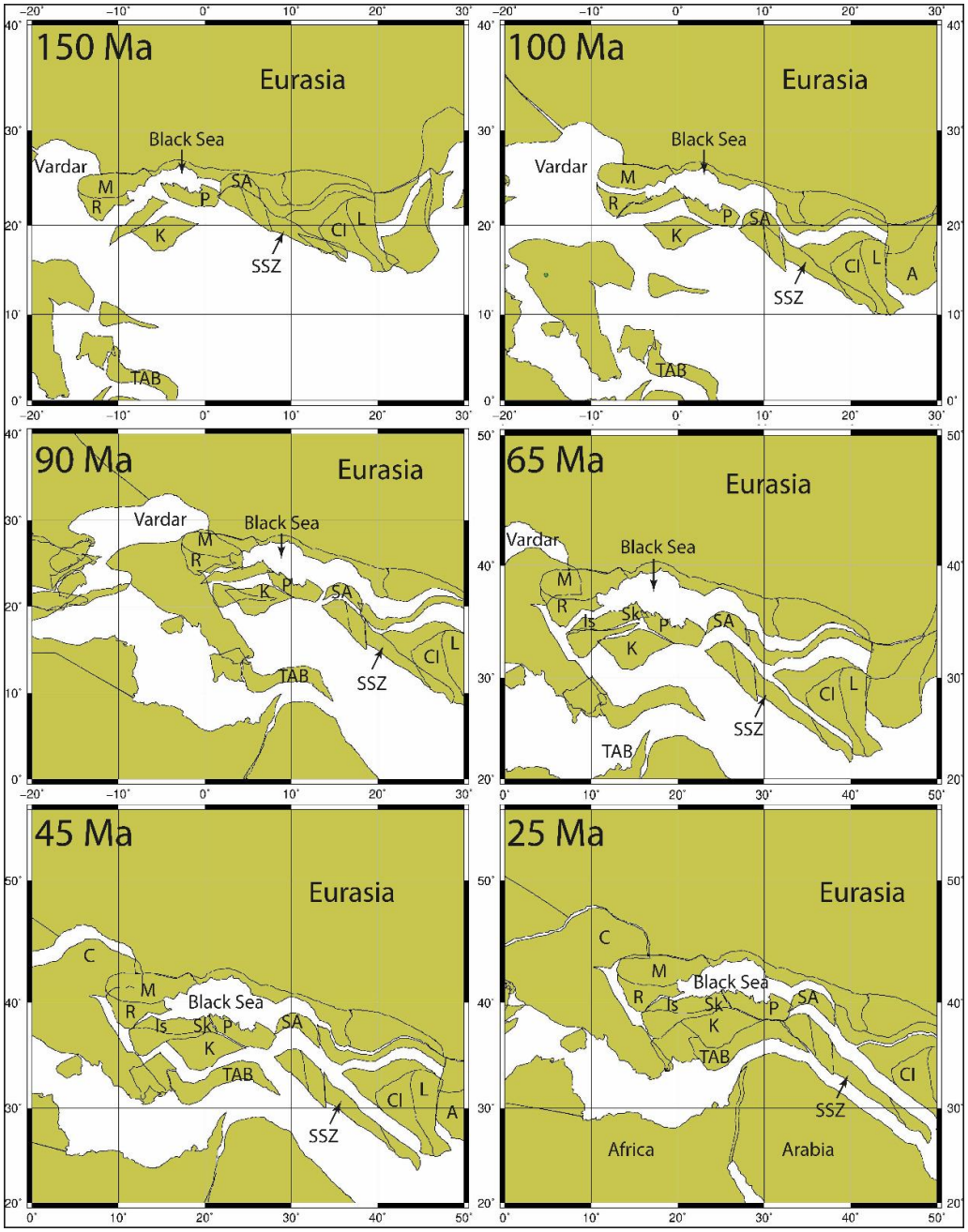


Figure 1.9. Paleogeographic reconstructions of Anatolia and its neighboring regions between 150 and 25 Ma as obtained from the Ocean Drilling Stratigraphic Network's Plate Tectonic Reconstruction Service (www.odsn.de/odsn/services/paleomap/paleomap.html). Abbreviations: A: Afghan Block; C: Carpathians; CI: Central Iranian Block; Is: Istanbul Zone; K: Kırşehir Block; L: Lut Block; M: Moesian Platform; P: Pontides; R: Rhodopes; SA: South Armenian Block; Sk: Sakarya Zone; SSZ: Sanandaj-Sirjan Zone; TAB: Tauride-Anatolide Block.

2019; Rabayrol et al., 2019). From a traditional point, present-day Turkey constitutes three main continental fragments (Ketin, 1966, Şengör and Yılmaz, 1981), which were separated from each other by curvilinear belts marked by the presence of ophiolite rocks and ophiolitic mélange. Of these three fragments, two (the Anatolide-Tauride Block and the Arabian Platform; Figure 1.9) were derived from the northern margin of Gondwana, whereas the Pontides has Laurasian affinity. The Anatolide-Tauride Block and the Arabian Platform in the south are separated from each other by the main branch of Neotethys (also known as Neotethys I, southern Neotethys or Bitlis-Zagros Ocean; Figure 1.9). On the other hand, the northern margin of the Anatolide-Tauride Block accreted to the Pontides is marked by the Izmir-Ankara-Erzincan Suture Zone, representing the closed northern branch of Neotethys (also known as Neotethys II; Figure 1.9). The early classification of the Turkish tectonic units, however, was later revised to include several other subdivisions (Okay and Tüysüz, 1999; Moix et al., 2008; Figure 1.10).

The northern part of Ankara remains within the Sakarya Zone, which together with the İstanbul and Rhodope-Strandja Zones make up the Pontide fragment, comprising most of the northern part of Turkey (Figure 1.10). The Sakarya Zone consists of a Variscan metamorphic basement cut by granitoid intrusions of Paleozoic age (Delaloye and Bingöl, 2000; Okay et al., 2006). Until the Late Triassic, the Sakarya Zone remained as a part of the active Laurasian margin, but the Permo-Triassic and Early Jurassic period saw widespread development of subduction-accretion complexes (the Karakaya and Küre complexes) along this active margin (Okay and Göncüoğlu, 2004; Okay et al., 2006). The opening of the marginal Küre ocean in the Late Triassic resulted in rifting of Sakarya Zone from Laurasia (Ustaömer and Robertson, 1994), but the Sakarya Zone and other Pontic fragments re-accreted to the Laurasian margin in the Early Jurassic, initiating the Izmir-Ankara-Erzincan (northern Neotethys) Ocean to the south of these fragments (Okay and Tüysüz, 1999; Moix et al., 2008). By this time, the Anatolide-Tauride Block and the Kırşehir Block already occupied the north-facing southern margin of the Izmir-Ankara-Erzincan Ocean.

Closure of this branch of Neotethys was initiated during the Cretaceous, which resulted in development of arc complexes mainly in the eastern and central Pontides (Okay and Şahintürk, 1997; Rice et al., 2006). Continent-continent collision between the Sakarya Zone and the Kırşehir Block occurred during the Late Cretaceous (Kaymakçı et al., 2000, 2009; Rice et al., 2006). This collisional event is generally regarded as a soft collision, whereas more significant hard collision likely took place in the late Paleocene–early Eocene interval (Rice et al., 2006; Kaymakçı et al., 2009).

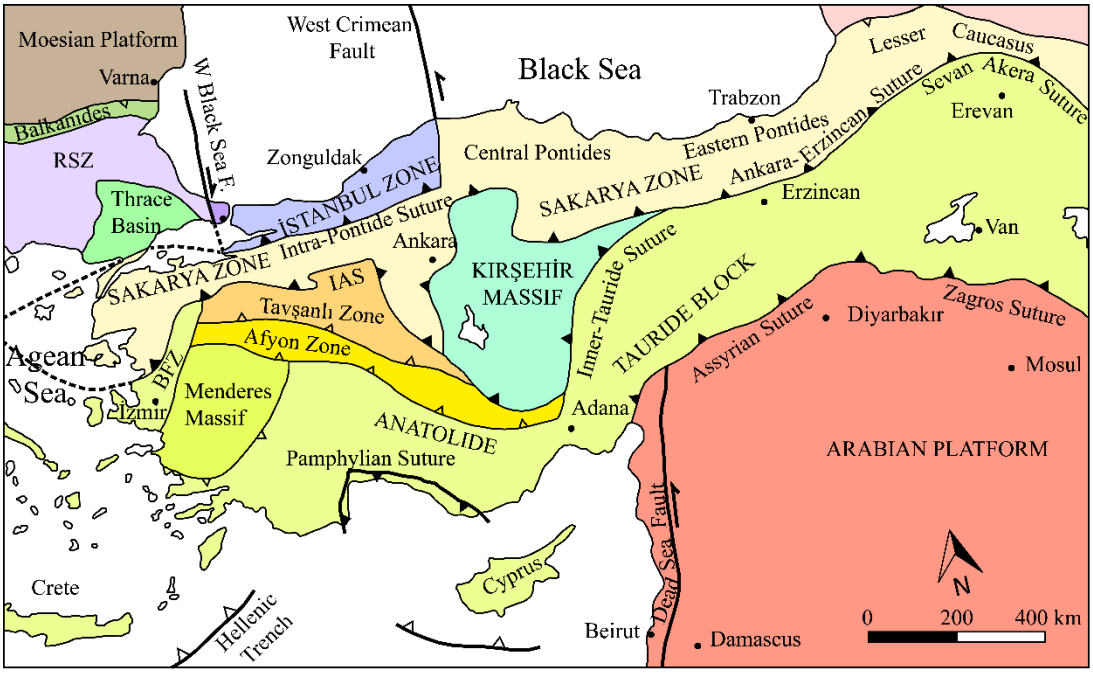


Figure 1.10. Map showing the major tectonic units and suture zones of Turkey (Okay and Tüysüz, 1999). IAESZ: İzmir-Ankara-Erzincan Suture Zone; RSZ: Rhodope-Strandja Zone; BFZ; Bornova Flysch Zone.

1.4.2. Overview of Cenozoic Volcanism in Northern Ankara

Complex tectonic background of Turkey provides suitable conditions for the Cenozoic volcanic activity which is associated with the closure of oceans and with neotectonic regimes. There are five main Tertiary–Quaternary volcanic provinces in Turkey,

namely the Western Anatolian volcanics (WAVP), Galatean volcanics (GVP), Central Anatolian Volcanics (CAVP), Eastern Anatolian Volcanics (EAVP), and the Karacadağ volcanics (KVP) (Bozkurt and Mittwede, 2001; Figure 1.11).

Central Anatolia is characterized by two important volcanic domains (1) the Galatian Volcanic Province (GVP; Toprak et al., 1996) and (2) the Central Anatolian Volcanic Province (Toprak and Göncüoğlu et al., 1993).

1.4.2.1. Galatean Volcanic Province

Galatian Volcanic Province, covering an area of approximately 6500 km^2, is located within the Pontide tectonic belt (Ketin, 1966) or Sakarya Zone (Okay and Tüysüz, 1999; Moix et al., 2008) of northwest Central Anatolia (Figures 1.10 and 1.11). It is bordered to the north by the North Anatolian Fault Zone (NAFZ) and is partially bordered to the south by the İzmir-Ankara-Erzincan suture zone forming a more or less triangular geological entity (Figure 1.12).

The term Galatean Volcanic Province, formerly named as "Galatian Volcanic Massive" by Leonhard (1902, 1915), "Ankara Volcanics" by Ach (1982), was firstly used by Toprak et al. (1996). Early studies on the petrochemistry of volcanic rocks around Ankara which consists of bimodal volcanism. Volcanism in Galatean Volcanic Province is a result of Early-Late Miocene (Akyürek et al., 1984; Türkecan et al., 1991; Wilson et al., 1997; Tankut et al., 1998a; Varol et al., 2007; Temel, 2010; Asan, 2015) eruptive volcanism.

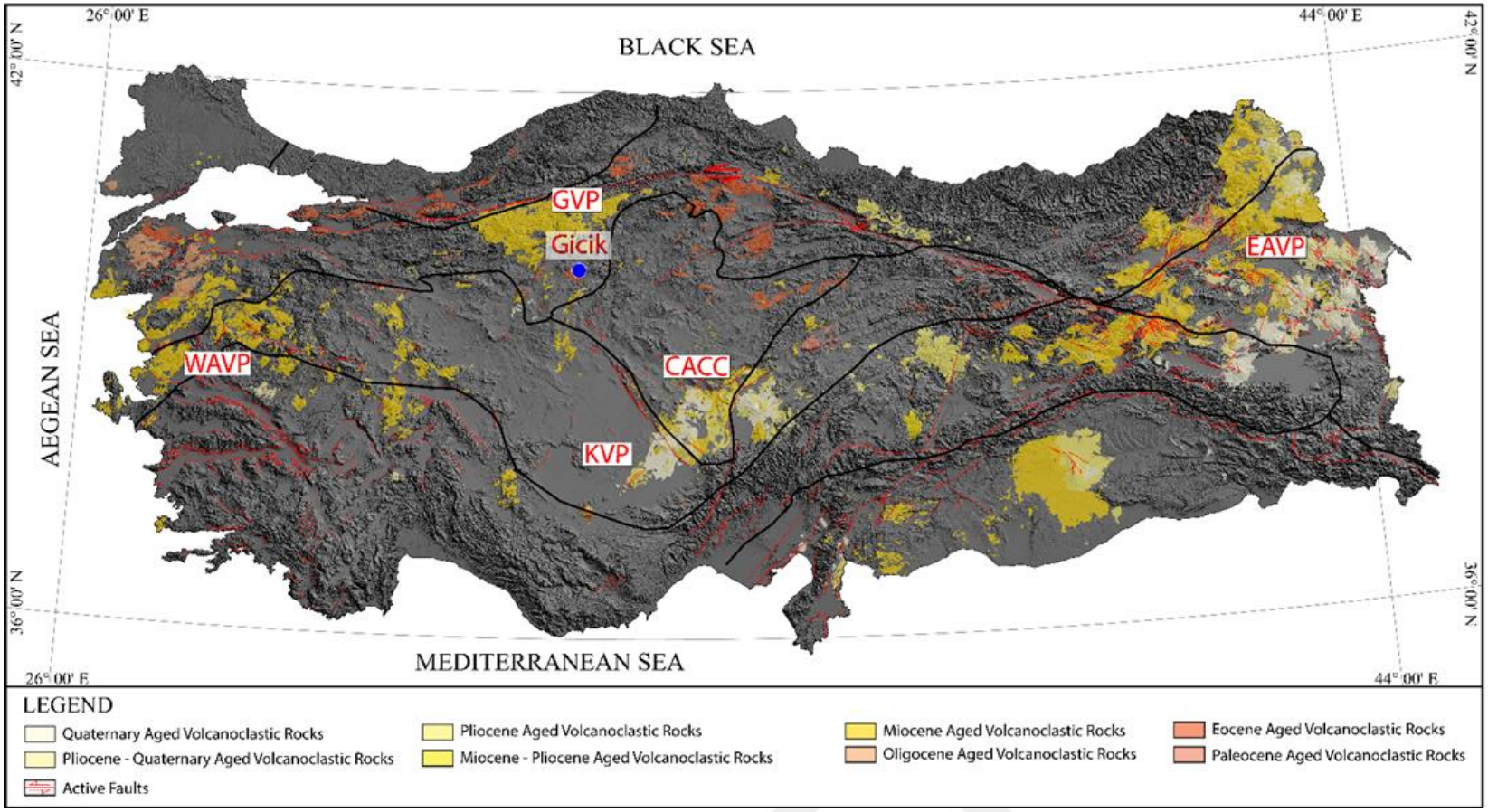


Figure 1.11. Map of Turkey showing distribution of the Cenozoic–Quaternary volcanic activity throughout Turkey and taken from MTA 1:25.000 geological maps (WAVP: Western Anatolian Volcanic Province; GVP: Galatean Volcanic Province; CACC: Central Anatolian Crystalline Complex; EAVP: Eastern Anatolian Volcanic Province; KVP: Karacadağ Volcanic Province).

Miocene volcanism which covers most of the Galatean Volcanic Province consists of volcanic rocks which are considered to be the result of two major phases of volcanism in Early Miocene and Late Miocene respectively. The main phase (Early Miocene) is comprised of early calc–alkaline, subduction and collision related alkali basalts to trachyandesite–andesite, trachydacite–dacite, agglomerate and tuffs with rare rhyolite (Leonhard, 1902, 1915; Büyükönal, 1971; Çalgın et al., 1973; Ach, 1982; Tankut 1985; Türkecan et al., 1991; Seyitoğlu and Büyükönal, 1995; Gökten et al., 1996; Wilson et al., 1997; Tankut et al., 1998a and b; Bozkurt et al., 1999; Adıyaman et al., 2001; Besbelli and Varol, 2002; Yürür et al., 2002; Varol et al., 2007 and 2008; Şen, 2009; Temel, 2010; Varol et al., 2014), and the latter (Late Miocene) is dominated by post–collision related Late Miocene mafic lavas ranging from alkali olivine basalt to basanite (Tankut, 1985; Adıyaman et al., 2001; Yürür et al., 2002; Temel, 2010; Varol et al., 2014; Asan, 2015). Geochronology when combined with geochemistry support the idea that subduction in Early Miocene (21–25 according to Türkecan et al., 1991; 17–19 Ma according to Wilson et al., 1997; 16–20 Ma according to Tankut et al., 1998a; 20–22 Ma according to Varol et al., 2007, Temel, 2010; Asan, 2015) produced lithospheric mantle modified, collisional and post–collisional calc–alkaline volcanism under NE–SW oriented compressional regime (Adıyaman et al., 2001), whereas in Late Miocene (<10 Ma according to Wilson et al., 1997; 10 Ma according to Tankut et al., 1998a), after a short cessation, volcanism produced post–collisional, asthenospheric mantle modified alkali mafic lavas under either E–W oriented (Adıyaman, 2001) or NE–SE to NNE–SSW multi–directed (Rojay and Karaca, 2008) extensional regime.

Volcanism in north of Ankara and Galatean Volcanic Province is divided into two phases, early arc-related calc-alkaline volcanism in Late Cretaceous-Middle Paleogene and collisional to post-collisional calc–alkaline to alkaline volcanism during the Miocene–Pliocene, respectively. Eocene volcanism in the central Anatolia is a result of subduction and following collision of Pontides and Anatolide-Tauride, and extensively exposed along İzmir-Ankara-Erzincan Suture Zone. Volcanic rocks

of Eocene age andesite and dacite have calc-alkaline characteristics which have been formed in post-collisional tectonic setting following the thickening of the crust at Eastern Anatolia which resulted in the collapse by slab-breakoff during middle Eocene (Keskin et al., 2008).

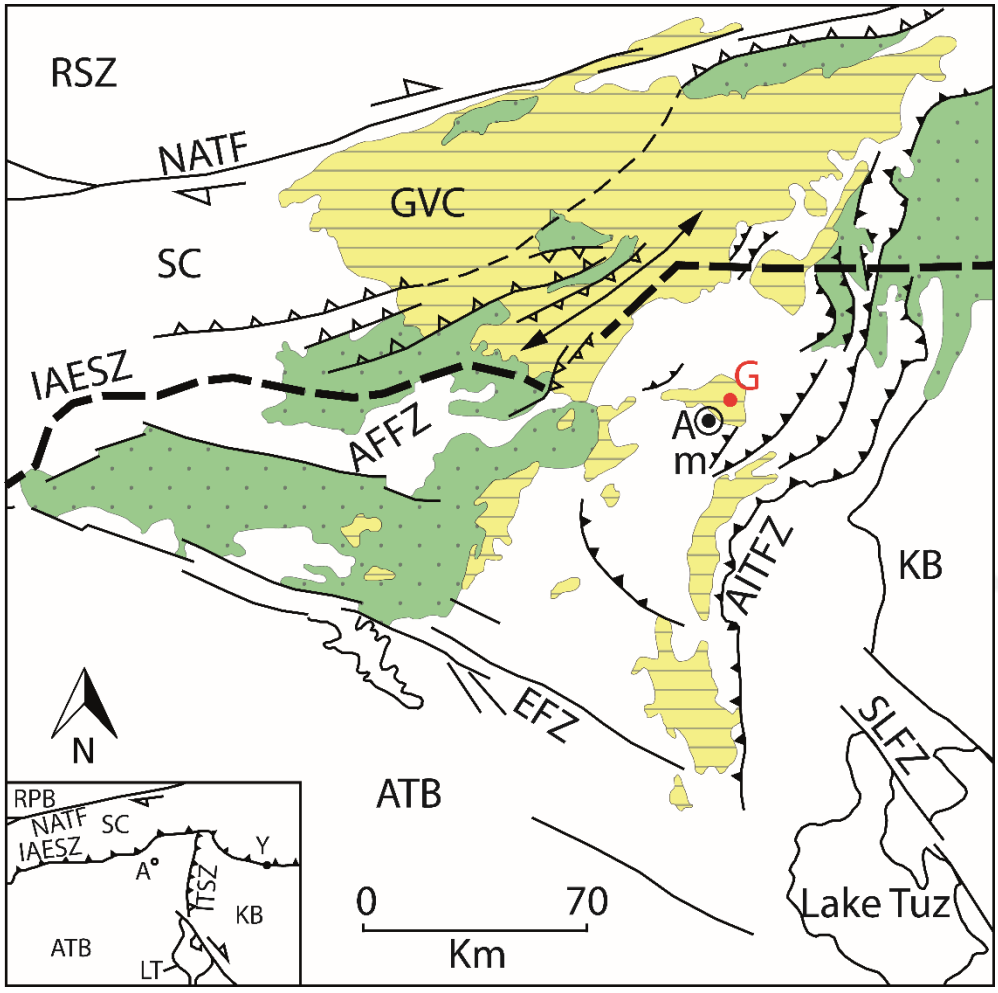


Figure 1.12. Regional tectonic setting of Central Anatolia (Koçyiğit et al., 1995). AFFZ: Ankara forced fold zone; AITFZ: Ankara imbricate thrust fault zone; GVC: Galatean Volcanic Complex; IAESZ: İzmir-Ankara-Erzincan Suture Zone; KB: Kırşehir Block; ATB: Anatolide-Tauride Block; NATF: North Anatolian Transform Fault Zone; RSZ: Rhodope-Strandja Zone; SC: Sakarya Continent; SLFZ: Lake Tuz Fault Zone; A: Ankara; G: Gicik.

1.5. Exploration History of Gicik

Gicik low–sulfidation epithermal system was firstly discovered by Eurogold after stream sediment and Bulk Leach Extractable Gold (BLEG) sampling at the end of eighties and beginning of nineties. Low-sulfidation epithermal style vein system in the Gicik area was discovered by following the initial positive anomalies obtained by sediment sampling methods. Having discovered the mineralized system, detailed geological mapping, rock (mostly channel) sampling and drilling at 22 locations with total of approximately 2,5 km drilling were completed further to understand the extend and evaluate the prospect. In 2005, Eurogold had to deal with environmental issues. These problems provided Koza Gold Company an opportunity to acquire license of the Gicik area. Exploration studies especially drilling activities were accelerated since then with almost 49 km of additional drilling at 144 drilling locations until 2009. Slightly less than 10 thousand tonnes of ore were produced with 2800 ounces of gold and 4100 ounces of silver by open pit mining method in august 2008 by Koza Gold. After a year of operation, Gicik open pit mine was closed. In 2018, drilling operations was restarted and still continue.

CHAPTER 2

GEOLOGY OF THE GİCİK AREA

2.1. Introduction

The Gicik vein system has been exposed about 15 km north of Ankara city center and about 4 km southeast of the town of Pursaklar. Gold mineralization at Gicik is hosted by intermediate composition andesitic–dacitic volcanic units of Cenozoic age, which cover large areas to the north and northeast of Ankara (Figure 2.1). The study area has an approximate surface extent of 13 km^2 within 40.00°N–40.02°N latitudes and 32.57°–32.60°E longitudes, and is contained within the south of H29-c3 quadrangle of 1:25,000 scale topographic map of Turkey.

Regionally, the widespread Cenozoic volcanism observed in northern and northeastern Ankara developed near the southern edge of the Sakarya Zone, where this tectonic fragment is separated from the Kırşehir Block along a Late Cretaceous accretionary belt consisting mainly of ophiolite rocks and ophiolitic mélange (Koçyiğit et al., 1995; Rojay, 2013; Figure 2.1).

There are several prominent volcanic vents near the study area, most notable of which is the Hüseyingazi Hill, located 4–5 km to the south Gicik (Figure 2.2). This prominent hill may be the likely eruptive center of the Gicik volcanic sequence. This sequence was initially included within the "Central Ankara Volcanics" of Tankut (1985). Akyürek et al. (1988) and Besbelli and Varol (2002), on the other hand, identified the andesitic–dacitic lava flows, tuffs and agglomerates near Hüseyingazi Hill, Elmadağ, Çubuk, and Sincan as Tekke Volcanics, and suggested a Miocene age for volcanic activity, contemporaneous with Galatian magmatism. However, published K-Ar ages between 47 and 44 Ma (Ach, 1982; Seyitoğlu and Büyükönal, 1995; Dönmez et al.,

2009) from Gicik, Hüseyingazi, and Kurtsivrisi contradicted this assumption, and indicated a much older volcanic cycle.

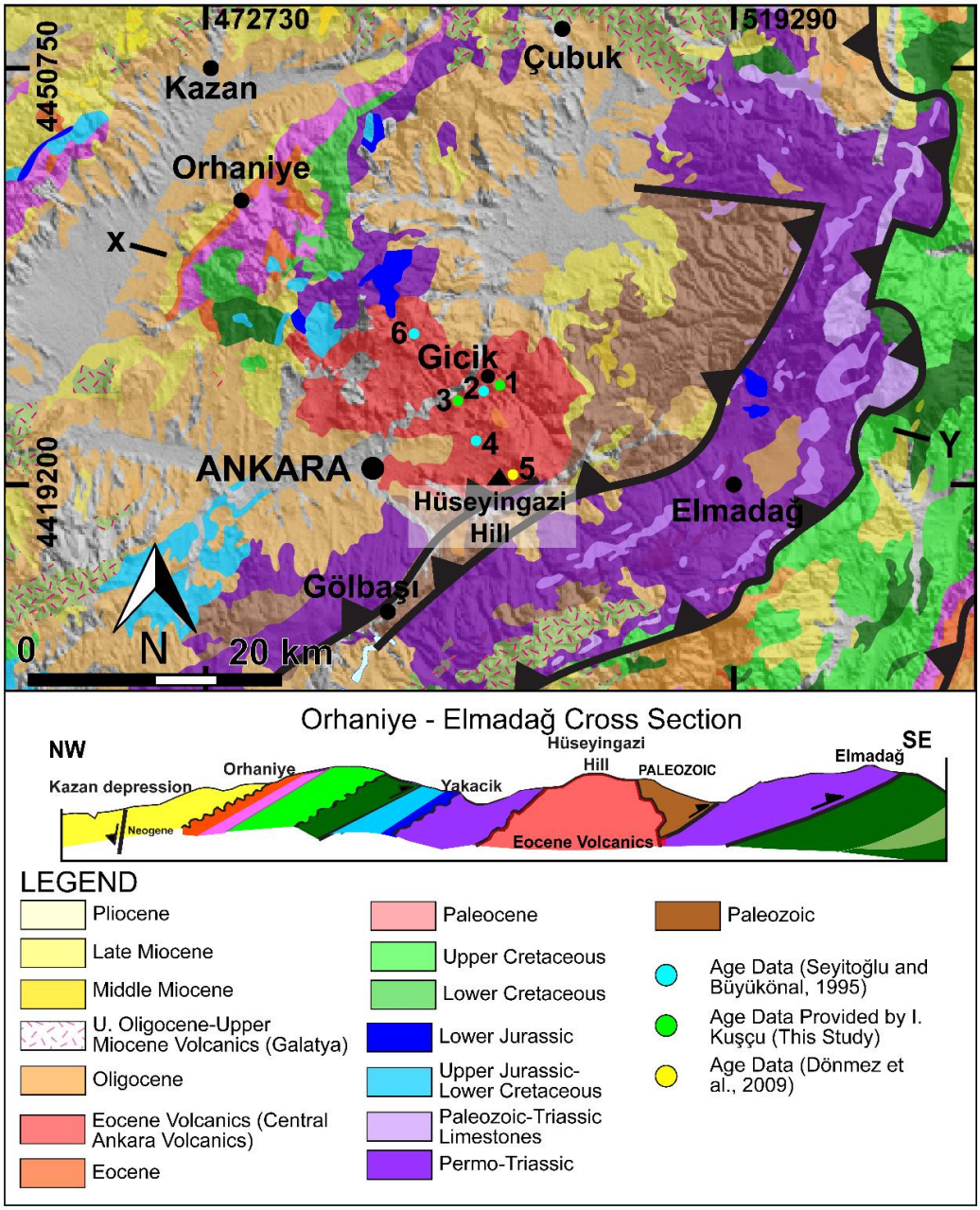


Figure 2.1. Geological map of Ankara region (Rojay, 2013). Lithologies are based on MTA 1:25.000 scale maps. Points on the map indicates age data: 1) 45.31 Ma, 2) 44.5 and 44.7 Ma, 3) 46.95 Ma, 4) 42.0 and 41,7 Ma, 5) 44.8 Ma and 6) 43.2 Ma.



Figure 2.2. View from Koza drill site just south of Gicik towards Huseyingazi Hill to the south (UTM Coordinates 497375 E, 4428678 N).

2.2. Lithological Units

Lava flows and agglomerates are the only lithologic units in the study area and are present as massive lava flows, agglomerates, and minor tuff layers. Based on contact relationships and texture, the intermediate group of volcanics were subdivided into three separate units: lower agglomerate unit, massive lava flows with agglomerate intercalations, and upper agglomerate unit (Figure 2.3). Apart from these, small mafic lava outcrops and Plio-Quaternary sedimentary cover are also present near Gicik (Figure 2.3).

All volcanic units and younger sedimentary cover units unconformably overlie the Paleozoic–Mesozoic metamorphic basement (Akyürek et al., 1982, 1984). The pre-

Cenozoic basement, however, do not crop out in the vicinity of Gicik, nor it was intersected in any of the drillholes during Eurogold's exploration campaign.

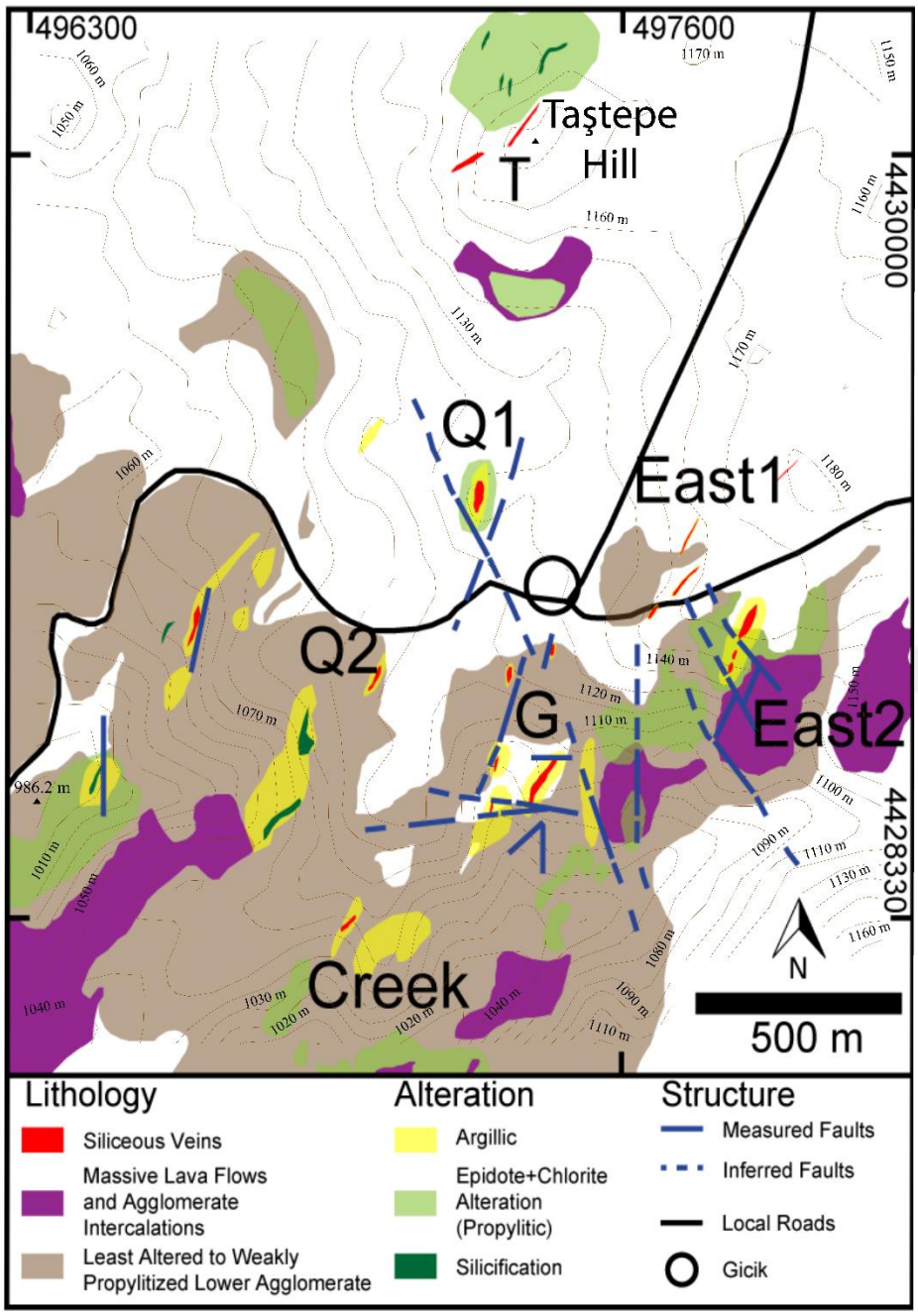


Figure 2.3. Detailed outcrop geology map of the Gicik area. White areas are agricultural field where there is no outcrop exposed.

2.2.1. Andesitic-Dacitic Lava Flows and Agglomerates

2.2.1.1. Lower Agglomerate Unit

Lower agglomerate unit, which occupies the lowermost part of the Gicik volcanic sequence, has the most widespread cover in the study area (Figure 2.3). This unit is well exposed in the central and southern parts of Gicik (Figure 2.3), and it can be easily recognized along the roadcuts opened during recent drilling operations by Koza Gold as well as along incised valleys walls and gullies.

In the outcrop, lower agglomerate unit typically has grayish to beige colors and consist of 2–10 cm-sized, gray colored, intermediate composition volcanic (andesitic-dacitic) blocks (Figures 2.4, 2.5 and 2.6). Dark colored ferro-magnesian minerals, which are visible to naked eye, and clasts of andesitic blocks comprise the matrix of agglomerates.

Lower contact of this unit is not observable throughout the study area, whereas its upper contact with massive lava flows with agglomerate intercalations is transitional and can be easily identified in the field (Figures 2.4, 2.5 and 2.6).

2.2.1.2. Massive Lava Flows and Agglomerate Intercalations

Massive lava flows are exposed at the central parts of the study area (Figure 2.3). Approximately N-S trending massive lava flows are exposed as intercalations with grayish colored agglomerate units. Several layers of massive pinkish colored massive lava flows intercalating with grayish colored agglomerates are identified in the field. Hornblende and biotite phenocrysts embedded within a pinkish colored matrix result in coarse-grained porphyritic texture in the lavas.

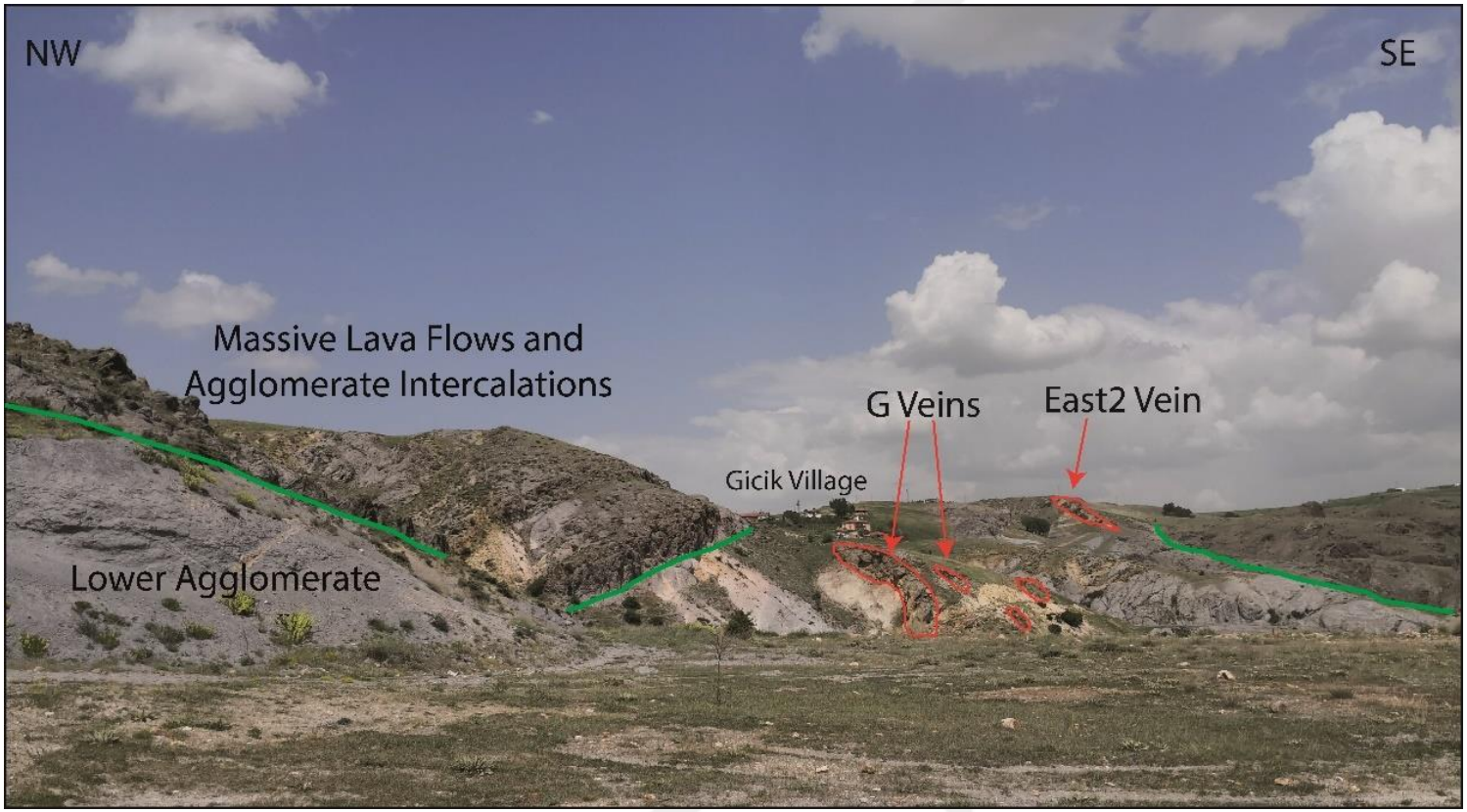


Figure 2.4. Lower agglomerate and massive lavas cross-cut by G and East veins south of Gicik (UTM Coordinates 497103 E, 4428360 N). Note the approximate N-S trend in massive lava flows.

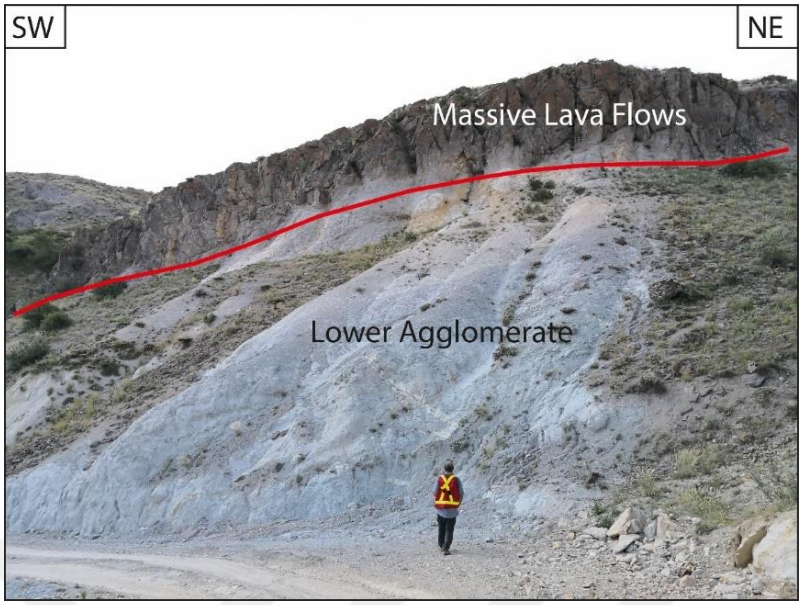


Figure 2.5. The contact between lower agglomerate and massive lava flows (UTM Coordinates 497251 E, 4428500 N).

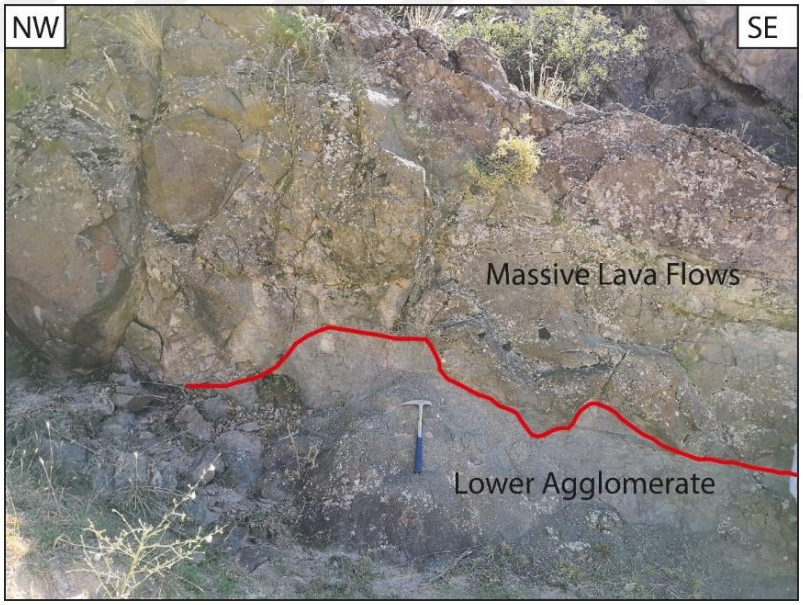


Figure 2.6. Contact between the lower agglomerate unit and pinkish colored massive lava flows (UTM Coordinates 497532 E, 4428656 N).

2.2.1.3. Upper Agglomerate Unit

The northern part of the study area is dominated by the upper agglomerate unit but its lateral continuity could not be assessed accurately because of widespread agricultural cover and recreational gardens resulting in relatively poor exposure. Consequently, the lower contact of this unit with massive lava flow and agglomerate intercalations could not be clearly observed as well. Nevertheless, the higher stratigraphic position of the upper agglomerates within the Gicik volcanic sequence is presumed since this unit outcrops at relatively higher elevations to the north of Gicik.

The upper agglomerate unit is best distinguished in the outcrop by the presence of boulder-sized (from several tens of centimeters to a meter in diameter) pinkish to grayish lava fragments surrounded by a grayish andesitic matrix (Figure 2.7a). This unit is best observed in the northern border of the study area approximately 1.5 km north of Gicik as well as near Akdoğan Hill in the northeast (Figure 2.8b).

Least-altered exposures of the upper agglomerates has undergone weak to moderate intensity propylitic alteration and the intensity of this type of alteration progressively increases towards east. In addition to propylitic alteration, silicification is also present especially towards the southern tip of the Akdoğan Hill, where silicified agglomerate outcrops form resistant ridges (Figure 2.8).

2.2.1.4. Mineralogy of Intermediate Volcanic Rocks

All identified units within the Gicik volcanic sequence are characterized by broadly similar mineral content and modal abundance, and textural characteristics. And it is difficult to distinguish three units, identified in the field, under thin section.

In the Gicik volcanic rocks, hornblende constitutes one of the main phenocrystic phases and its modal abundance ranges about 20-25%. Hornblende phenocrysts are mostly euhedral to subhedral, and have blocky prismatic habit (Figure 2.9). Their dark brown color implies that hornblende is rich in iron (Gribble and Hall, 1992), yet there are some rare greenish colored varieties. Representative compositional data for

hornblende phenocrysts are presented in Table 2.1 and full data is provided in Appendix A.

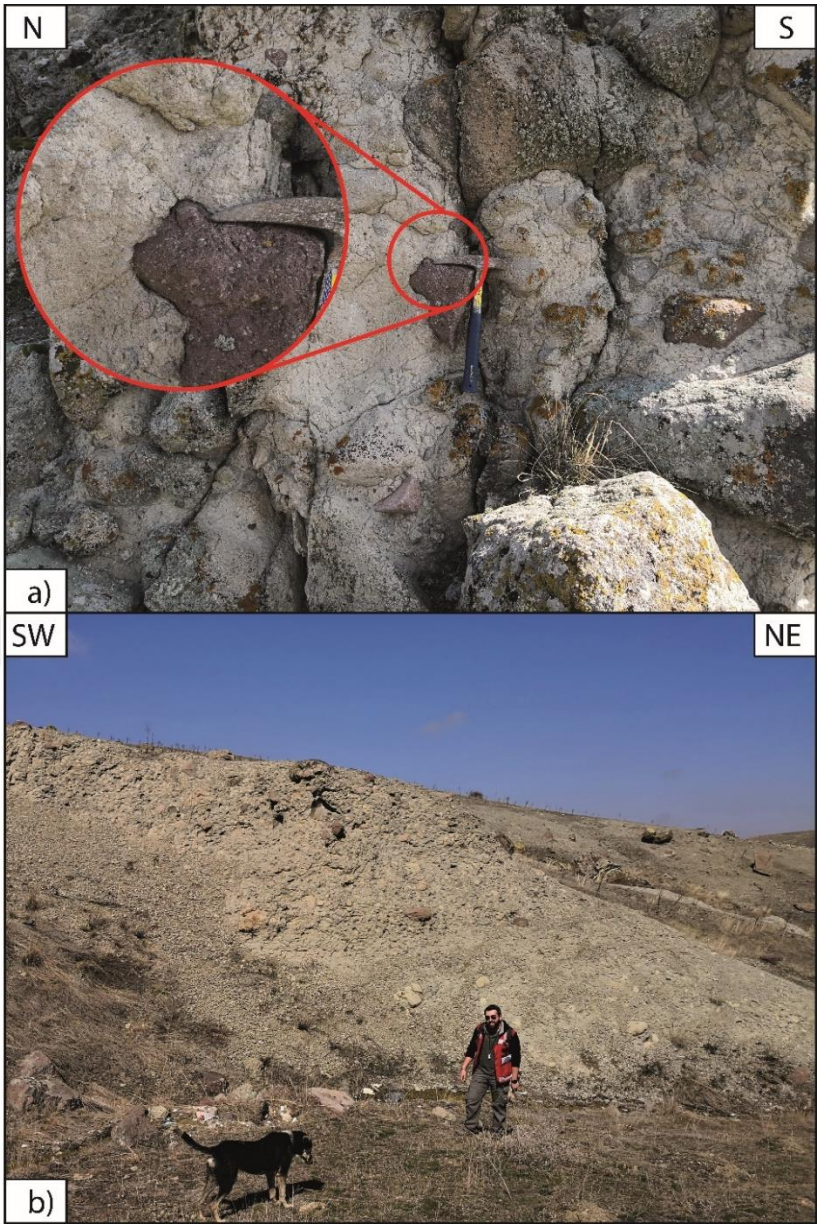


Figure 2.7. Field photographs of the upper agglomerate unit. a) outcrop from the Akdoğan Hill. Note the presence of pink colored massive andesitic boulders within the gray andesitic matrix (UTM Coordinates 498782 E, 4431414 N) b) outcrop from creek at the East of the road (UTM Coordinates 498000 E, 4431875 N).



Figure 2.8. Resistant silicified outcrops towards south of Akdoğan Hill (looking east; UTM Coordinates 497783 E, 4431620 N).

Most hornblende crystals contain minute inclusions of plagioclase and/or magnetite (Figure 2.9b). Oxidation of hornblende to opacite (Fe-Ti oxide phases) is common. Most crystals show complete oxidation to Fe-Ti oxides (Figure 2.9c), but in remaining crystals oxidation is incomplete, primarily developed along the rims or cleavage planes (Figures 2.9b and 2.9d). Opacitization of hornblende in volcanic or sub-volcanic rocks are commonly attributed to magmatic oxidation or depressurization of magma during ascent (Rutherford and Hill, 1993; Chambefort et al., 2013).

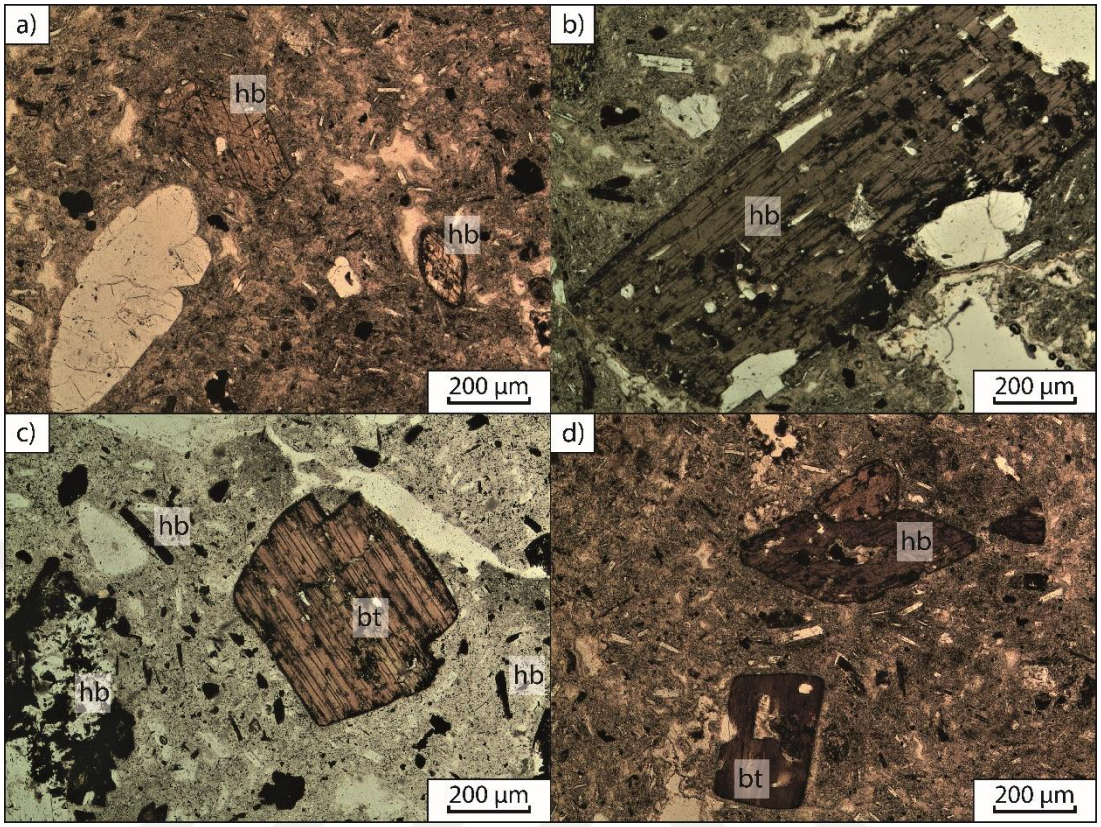


Figure 2.9. Microphotographs of hornblende (hb) and biotite (bt) in volcanic rocks around Gicik area a) euhedral hornblendes with highly developed cleavage planes (Sample GCK-12, PPL), b) slightly opacitized euhedral hornblende (Sample GCK-12, PPL), c) euhedral biotite and completely opacitized hornblende (Sample GCK-09, PPL), and d) euhedral hornblende and biotite lying inside groundmass (Sample GCK-12, PPL).

Biotite commonly occurs as subhedral to euhedral phenocrysts with grain sizes of 1–2 mm in diameter and has an average modal abundance of 10–15% (Figures 2.9c, 2.9d, 2.10a and 2.10b). Similar to hornblende, majority of biotite crystals have been completely to incomplete opacitized (Figures 2.10c and 2.10d), again likely due to oxidation of parental magmas during cooling and crystallization upon ascending to shallow crustal level (Rutherford and Hill, 1993; Chambefort et al., 2013). Representative compositions of biotite phenocrysts from least-altered volcanic rocks is given in Table 2.1, and full compositional data is presented in Appendix B.

Plagioclase crystals are mostly euhedral to subhedral (Figures 2.11a, 2.11b and 2.11c), and form approximately 40–45% of the volcanic rocks. They occur either as large phenocrysts (1–4 mm in diameter) or as finer-grained (≤1 mm) lath–shaped microlites within the groundmass of the lava flows (Figure 2.11a). Plagioclase microlites occasionally have preferred orientations suggesting flow direction upon eruption. Polysynthetic twinning is commonly observed together with compositional zoning in all plagioclase crystals. Plagioclase in Gicik volcanic rocks is typically andesine in composition (Table 2.2 and Appendix C). In compositionally zoned plagioclase, well-developed silicate melt inclusions were identified along concentric compositional zones (Figure 2.11d).

Quartz comprises about 8–10% of the intermediate composition volcanic rocks and is commonly subhedral to anhedral in form. It is found either as isolated phenocrysts or in glomeroporphyritic clusters. Embayed quartz grains were occasionally observed in some of the studied samples (Figure 2.12a) indicating partial resorption of quartz by the molten magma during ascent and decompression (Nekvasil, 1991).

In least-altered intermediate volcanic rocks, magnetite is the most abundant opaque mineral phase. Isolated microphenocrysts of magnetite (30 to 50 microns in diameter) typically make up about 2-5% of volcanic rocks. Relatively smaller amounts of ilmenite also occur in the same volcanic rock samples, either as microphenocrysts intergrown with magnetite or more commonly as exsolution lamellae within magnetite grains (Figure 2.12b).

Representative compositions of magnetite and illmenite phenocrysts from least-altered volcanic rocks is given in Table 2.3 and Table 2.4, respectively, and full compositional data is presented in Appendix D and Appendix E.

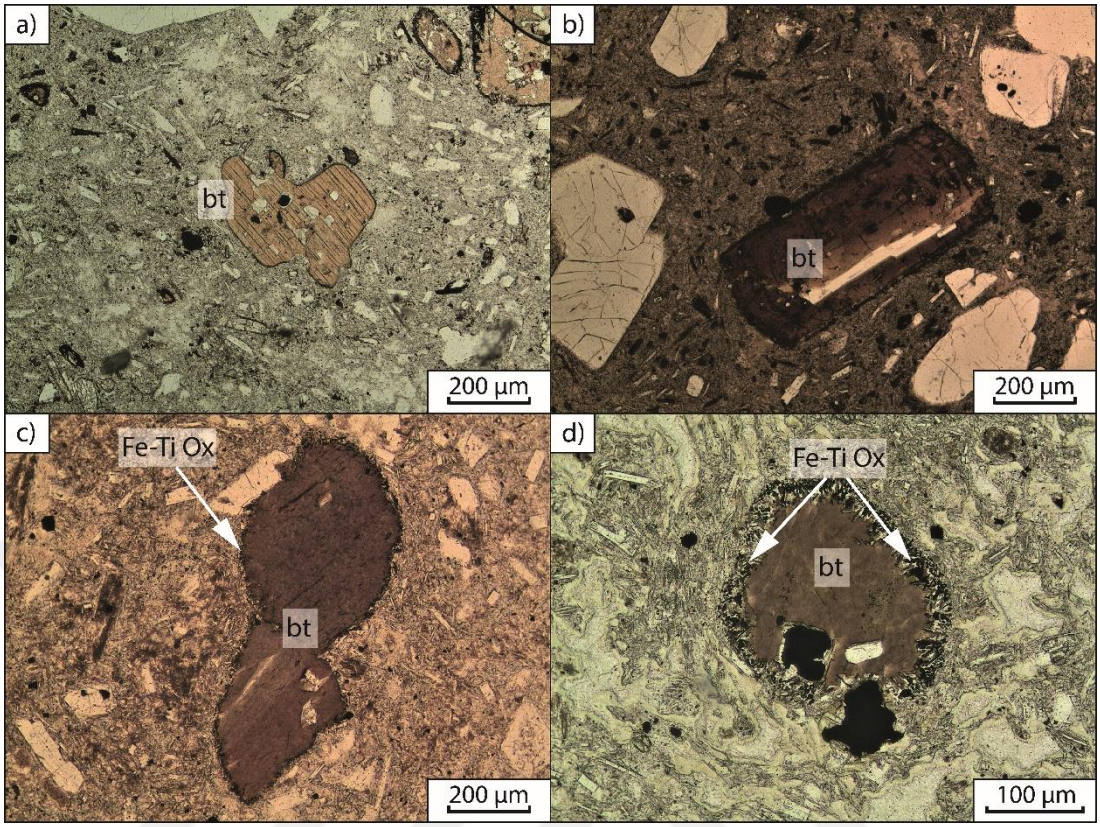


Figure 2.10. Microphotographs of biotite (bt) in volcanic rocks around Gicik area a) subhedral biotite lying in groundmass (Sample GCK-01, PPL), b) euhedral biotite in volcanic rock (Sample GCK-12, PPL), c) subhedral biotite crystals with slightly oxidized rims (Sample GCK-12, PPL), and d) biotite crystal with tiny opaque crystals which are Fe-Ti oxide crystals formed due to crystal-melt reaction during cooling and crystallization of magma (Sample GCK-37, PPL).

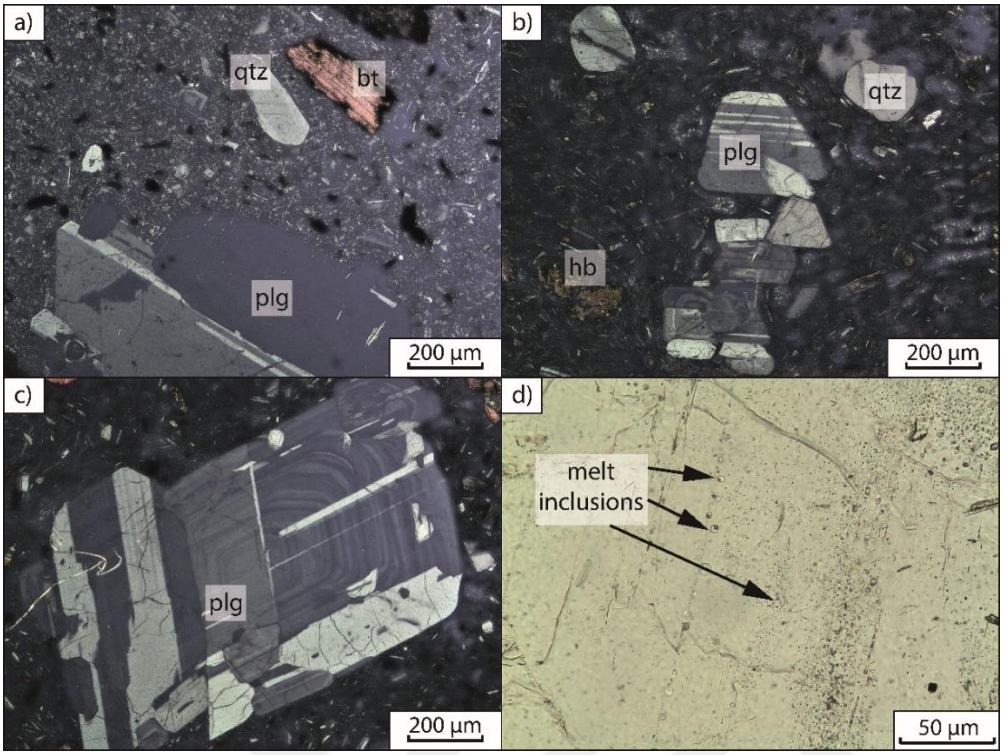


Figure 2.11. Microphotographs of plagioclase feldspar (plg) in volcanic rocks around Gicik area a) representative appearance and texture of dacitic lava flows. Porphyritic texture is represented by plagioclase feldspar, biotite (bt) and quartz (qtz) phenocrysts set in finer-grained groundmass of plagioclase microlites (Sample GCK-09, XPL), b) plagioclase phenocrysts showing polysynthetic twinning forming cumulates with quartz and hornblende phenocrysts (Sample GCK-36, XPL), c) plagioclase feldspar grain displaying polysynthetic twinning and compositional zoning (Sample GCK-01, XPL), and d) melt inclusions clustered in the compositional zones of plagioclase phenocryst (Sample GCK-04, PPL).

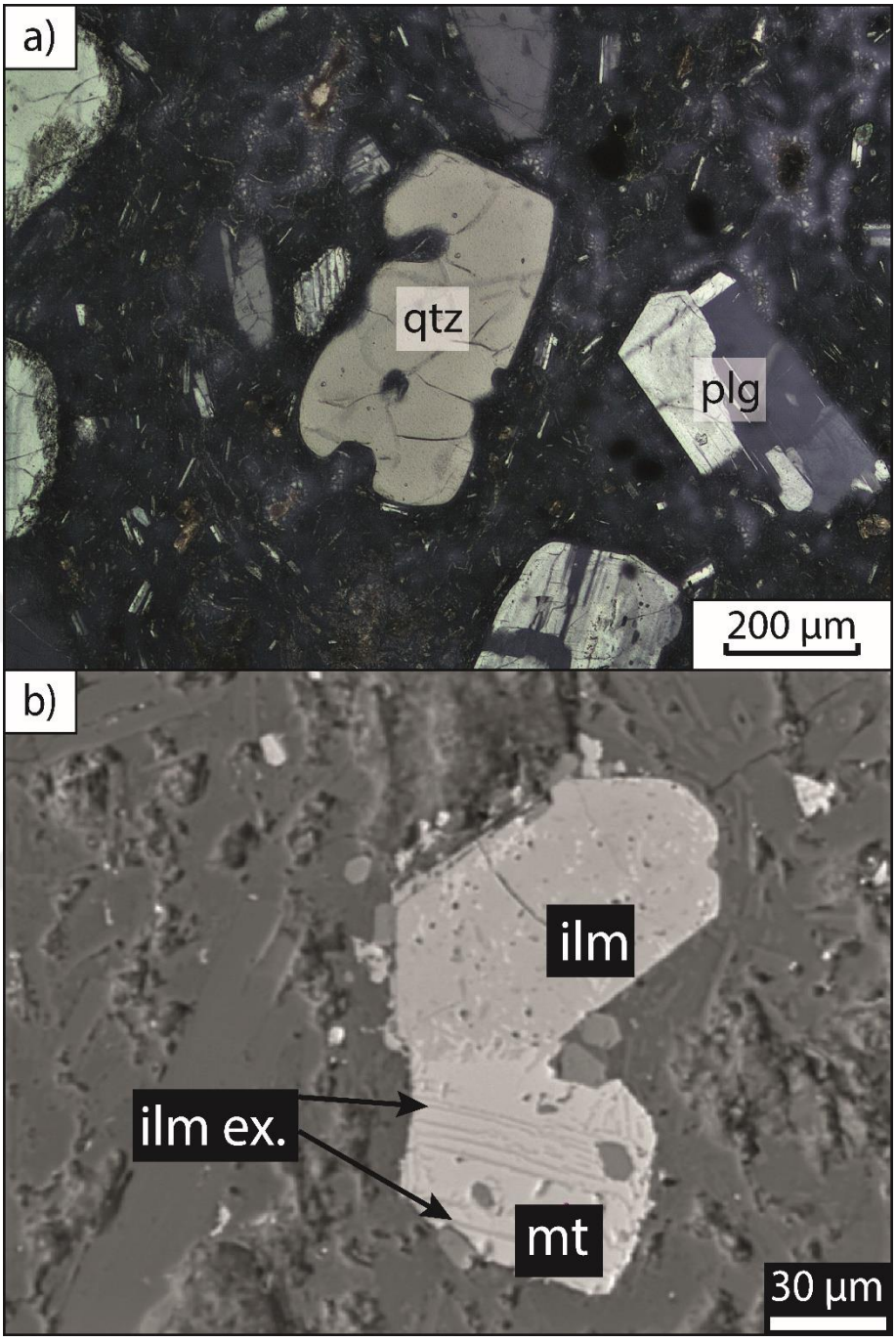


Figure 2.12. Microphotographs of a) quartz (qtz) phenocryst displaying embayed texture (Sample GCK-37, XPL) and b) EPMA back scattered image of light gray colored magnetite (mt) with dark gray colored ilmenite (ilm). Ilmenite is both found as phenocrysts (ilm) and exsolution lamellae (ilm ex.) (Sample GCK-01).

Table 2.1. Representative EPMA compositions of hornblende (hb) and biotite (bt) from least-altered volcanic rock samples from Gicik. All values are reported in wt%.

Sample No.	G1-2 hb	G1-4 hb	G1-5 hb	G12-2 hb	G12-4 hb	G12-6 hb	G12-7 hb	G1-4 bt
Na_2O	1.14	1.08	1.19	1.32	1.08	1.08	1.17	1.19
SiO_2	48.50	49.30	48.35	46.87	48.90	48.58	49.01	48.17
Al_2O_3	6.31	6.39	6.58	7.43	5.75	5.98	6.22	6.80
MgO	15.64	15.86	15.52	14.55	15.76	15.61	15.69	15.31
K_2O	0.388	0.332	0.355	0.466	0.304	0.332	0.329	0.385
CaO	11.18	10.88	10.85	11.06	10.87	11.00	10.92	10.93
FeO	11.91	12.03	11.87	12.46	11.36	11.70	11.71	12.12
MnO	0.403	0.457	0.390	0.347	0.431	0.424	0.422	0.398
NiO	0.012	0.008	0.012	0.026	0.017	0.016	0.006	0.015
TiO_2	1.12	1.12	1.23	1.47	1.08	1.22	1.15	1.27
Cr_2O_3	0.001	0.004	0.004	0.012	0.011	0.018	0.048	0.007
O	1.81	1.84	1.81	1.79	1.80	1.81	1.82	1.81
Total	98.41	99.28	98.15	97.79	97.36	97.77	98.49	98.40

Table 2.2. Representative EPMA compositions of plagioclase phenocrysts from least-altered volcanic rock samples from Gicik. All values are reported in wt%.

Sample No.	G1-1	G1-3	G1-6	G1-7	G12-1	G12-5	G12-6	G12-8
Na_2O	6.28	6.34	6.08	6.18	6.00	6.13	6.41	5.64
SiO_2	58.68	58.99	57.92	58.37	58.16	58.10	58.75	57.26
Al_2O_3	25.83	25.52	26.20	25.83	25.72	25.84	25.39	26.39
K_2O	0.433	0.420	0.363	0.400	0.411	0.401	0.439	0.551
CaO	7.96	7.68	8.37	8.01	8.05	8.09	7.70	8.79
SrO	0.128	0.132	0.127	0.126	0.132	0.124	0.130	0.123
BaO	0.041	0.051	0.018	0.054	0.053	0.027	0.068	0.043
FeO	0.208	0.219	0.190	0.211	0.215	0.211	0.258	0.204
Total	99.56	99.35	99.27	99.17	98.75	98.92	99.13	99.01

Table 2.3. Representative EPMA compositions of magnetite microphenocrysts from least-altered volcanic rock samples from Gicik. All values are reported in wt%.

Sample No.	G1-8-2 mt	G1-8-3 mt	G1-9-1 mt	G1-9-3 mt	G1-9-4 mt
MgO	2.06	1.39	1.38	1.39	1.40
Al_2O_3	1.82	0.96	1.99	1.92	1.66
SiO_2	0.041	0.510	0.00	0.217	0.109
FeO	79.61	70.46	81.94	76.68	81.49
TiO_2	4.72	16.12	3.25	3.07	3.21
MnO	0.633	0.259	0.347	0.367	0.412
V_2O_3	0.044	0.162	0.025	0.302	0.055
NiO	0.037	0.002	0.036	0.020	0.024
Cr_2O_3	0.085	0.098	0.082	0.101	0.082
CaO	0.039	0.083	0.021	3.053	0.072
Total	89.08	90.05	89.07	87.12	88.51

Table 2.4. Representative EPMA compositions of ilmenite microphenocrysts from least-altered volcanic rocks samples from Gicik. All values are reported in wt%.

Sample No.	G1-8-1 ilm	G1-8-2 ilm	G1-8-3 ilm	G-1-9-1 ilm	G-1-9-2 ilm
MgO	1.76	2.04	2.35	1.84	2.01
Al_2O_3	0.46	0.86	1.26	0.72	0.60
SiO_2	1.950	0.031	0.023	0.054	0.027
FeO	53.16	47.82	44.67	46.96	52.16
TiO_2	32.84	40.27	42.94	41.41	34.87
MnO	0.537	0.460	0.191	0.300	0.245
V_2O_3	0.250	0.162	0.344	0.144	0.325
NiO	0.025	0.015	0.011	0.017	0.012
Cr_2O_3	0.028	0.011	0.009	0.016	0.085
CaO	0.092	0.038	0.046	0.016	0.070
Total	91.10	91.70	91.84	91.48	90.40

2.2.2. Basaltic Lavas

Small outcrops of basaltic lavas are exposed outside, but in close proximity of the southern part of the study area. The lateral continuity of the basaltic lavas is very limited, and therefore these lavas were not mapped.

Basaltic lavas are dark green to black in the outcrop (Figure 2.13). Contact relationship of this unit with the surrounding intermediate composition volcanic units is not clear, however, based on the regional observations, basaltic lavas are assumed to overlie the Gicik volcanic units.



Figure 2.13. Field photograph of basalt unit exposed at the roadcut towards the southeastern border of the study area (499138E, 4426917N).

Moderate to strong intensity propylitic alteration is common in basaltic lavas. However, plagioclase and minor quartz were observed as relict primary mineral phases. Plagioclase occurs mainly as microlites as well as large phenocrysts (2–4 millimeters in diameter), but phenocrystic plagioclase has been mostly altered to carbonate, epidote, and chlorite (Figure 2.14). Quartz is the second most abundant

(about 10%) primary mineral in basaltic lavas. Quartz phenocrysts (0.2–1.0 mm) are clustered together resebling glomeroporphyritic texture. Fine-grained cubic grains of pyrite were also identified in basaltic lavas.

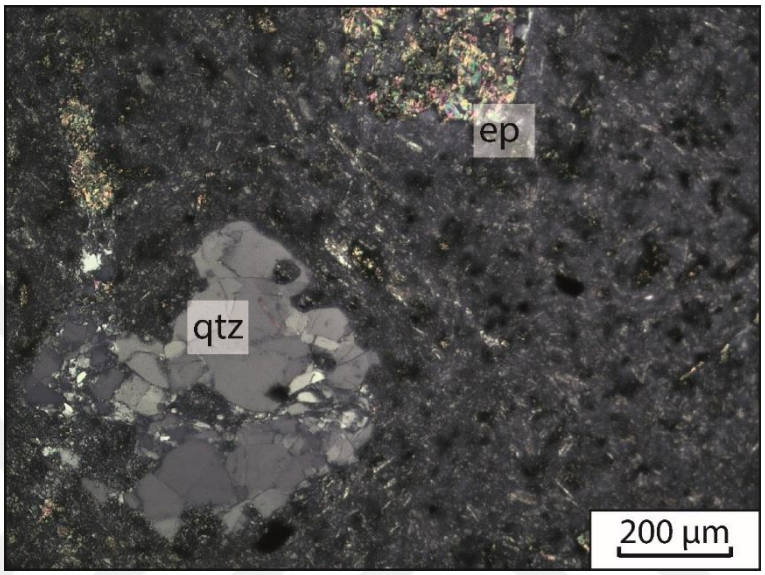


Figure 2.14. Microphotograph of basalt sample with quartz phenocrysts forming glomeroporphyritic texture. Note the high birefringence epidote developed on feldspar phenocryst (Sample GCK-10, XPL).

2.3. Siliceous Veins

Gold at Gicik is contained in a series of NNE–striking quartz veins (Figure 2.3) hosted in dacitic lava flows and agglomerates. Five sets of veins were identified within the Gicik mineralized system and these were originally named as T, Q, G, East and Creek Veins (Figure 2.3) by Eurogold. The same vein nomenclature will be followed here as well with minor modifications.

Thicknesses of the siliceous veins at Gicik vary from 1 to 10 meters in the surface. Colloform banding, hydrothermal brecciation, stockwork veinlets and lattice–bladed textures are the dominant textures present in these vein systems (Figures 2.15 and

2.16; also see Appendix F). Gold mineralization in vein samples from the surface is associated with an ore mineral assemblage dominated by sulfide minerals, such as pyrite, arsenopyrite, and tetrahedrite. The formation of quartz veins is related with the NNE-striking strike-slip faults, which display a dominant oblique component with reverse movement. Apart from these fault sets, a second set of faults striking NNW cuts and laterally offsets siliceous veins (Figure 2.3).

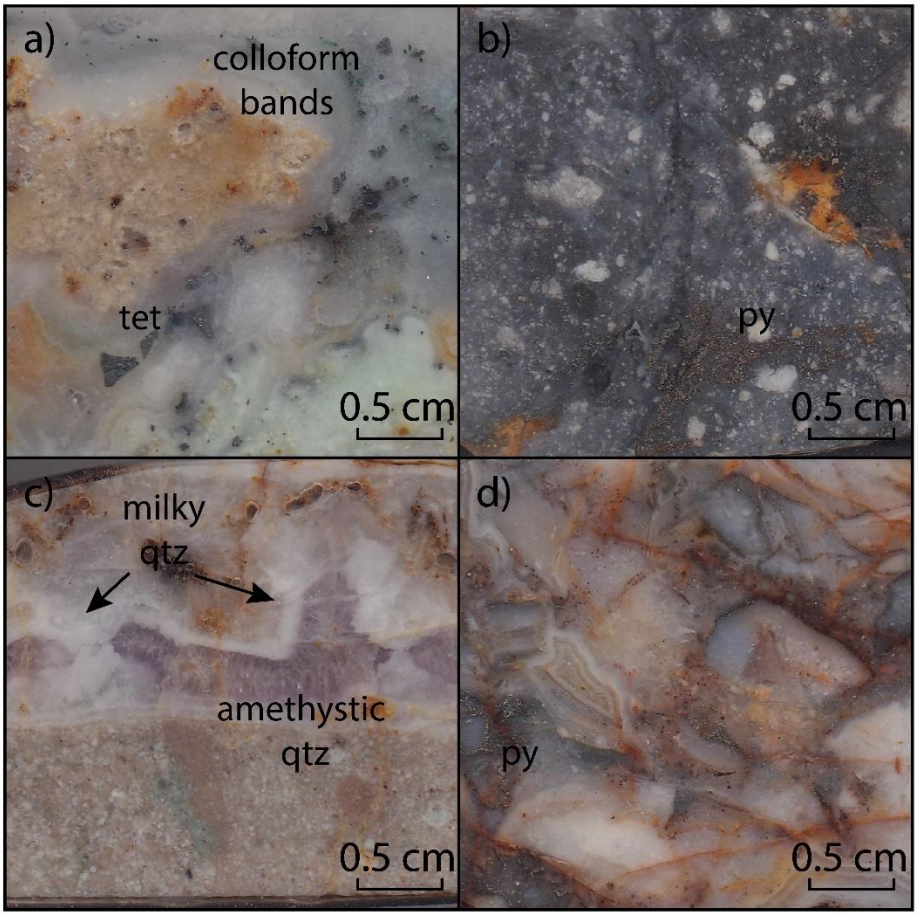


Figure 2.15. Various textures and minerals observed within the Gicik vein system; a) Gray colored rhombohedral tetrahedrite intergrown with pyrite (not visible in this image) in colloform banded silica from G Vein (Sample GCK-64-2), b) dark colored silicified andesite with pyrite from East Vein (Sample GCK-61), c) colloform banded milky quartz with late amethystic quartz (purple) from southernmost part of Q2 Vein (Sample GCK-54), d) hydrothermal breccia with colloform bands consisting of quartz-pyrite from Q1 Vein (Sample GCK-38).

Mineralogy and texture of each vein system are broadly similar to each other, yet there are some significant differences and specific textures are better developed in certain vein sets. A summary table highlighting vein characteristics is provided in Table 2.5.

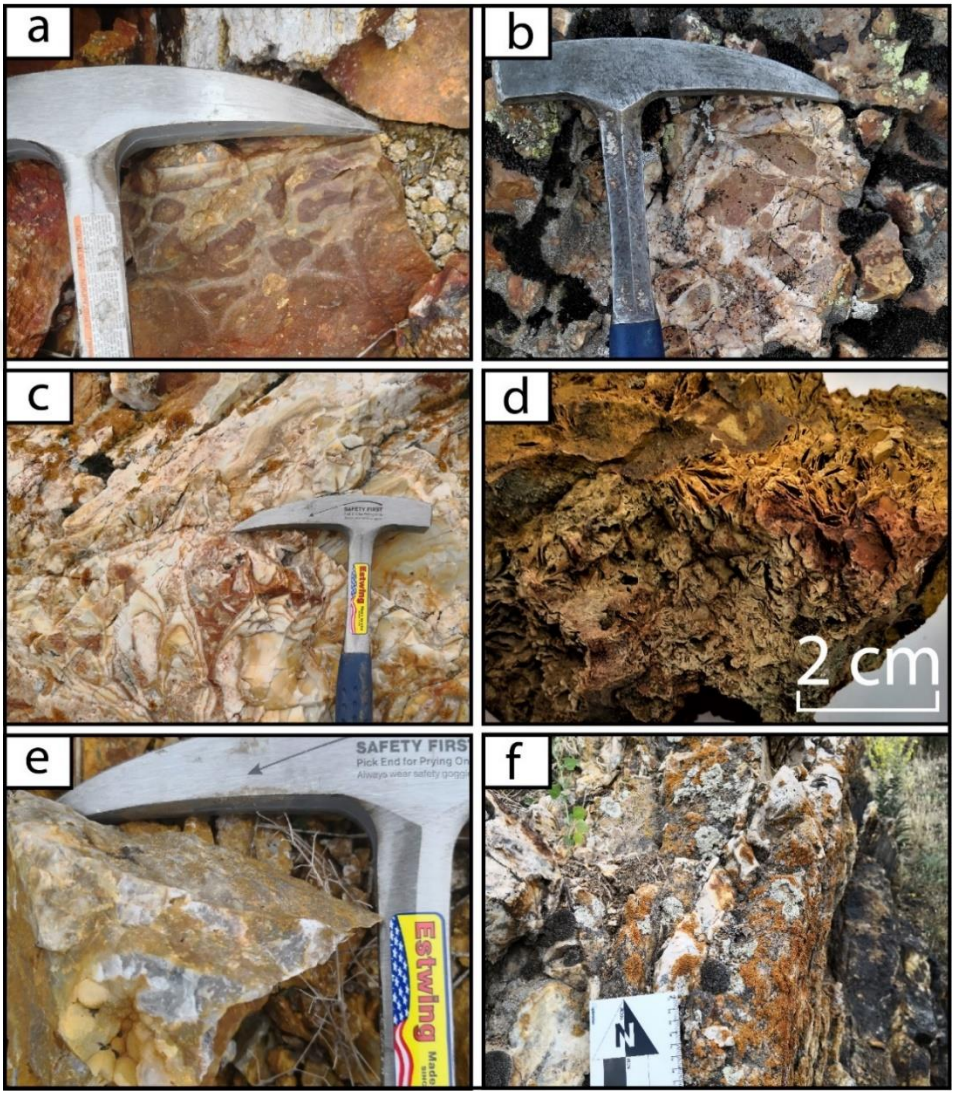


Figure 2.16. Typical vein textures from the Gicik vein system; a) and b) hydrothermal breccia from (Q Vein), c) colloform banding and cockade texture (G Vein), d) lattice bladed texture (Q Vein), e) drusy quartz (Q vein), and f) massive quartz (G Veins).

Table 2.5. Summary of the veins in terms of textures and ore mineralogy

East	Vein	Thickness	Exposed Strike Length	Orientation	Description	Textures	Ore Minerals	Gangue Minerals
T	-	~2-3 m	~120 m	NE-SW	Blocks and boulders of silicified intermediate composition volcanic rocks	2-5 cm thick massive quartz veinlets	-	Quartz
Q	Q1	~5-10 m	~80 m	N-S	Siliceous vein surrounded by intensely altered host rock	Stockwork, colloform banding, lattice bladed, cockade, open space filling, hydrothermal breccia	Pyrite	Quartz, amethystic quartz
	Q2	~2-3 m	~27 m	NE-SW	Two vein sets merging at the south forming the main vein	Colloform, massive, open space filling, cockade, hydrothermal breccia	Pyrite	Quartz
G	-	~1-3 m	~10-60 m	NE-SW	Comprises of several small veins	Colloform banding, gray colored silicification, open space filling	Pyrite, arsenopyrite, tetrahedrite	Quartz
East	East1	~1-3 m	~15-40	NE-SW	Blocks and boulders of silicified host rock	-	-	Quartz
	East2	~2-7 m	~140 m	NE-SW	Several thin veins in the same orientation forming the main vein	Hydrothermal breccia, gray colored silicification, stockwork	Pyrite, arsenopyrite	Quartz
Creek	-	~3-4 m	~25 m	NE-SW	Silica vein with intensly silicified host rock	Massive, open space filling	Minor pyrite	Quartz

2.3.1. T Vein

T Vein is exposed ~1 km northwest of the study area near Taştepe Hill, where it forms a prominent hill within the surrounding agricultural field due to intense silicification leading to resistance to erosion. In outcrop, the vicinity of the vein comprises intensely silicified agglomerates, and the vein itself is only poorly exposed. However, where observed (Figure 2.17), the vein has a thickness of ~2–3 m and an exposed strike length of ~120 meters. The vein appears as intensely silicified volcanic rocks with 2–5 cm thick, white colored massive quartz veinlets. In comparison to other veins at Gicik, the T vein is exposed at a relatively higher elevation (1170–1180 meters), and may represent higher levels of the hydrothermal system.

The T vein was the first vein segment at Gicik, which was drilled by Eurogold. A total of six diamond drill holes were drilled through this vein and assay values as high as ~50 g/t from one meter-thick intervals were reported from drillhole TD-5 (497024E, 4429981N).

2.3.2. Q Vein

The Q vein system is subdivided into two major veins: Q1 and Q2 (Figure 2.3). The Q1 vein comprising the northern part is one of the best developed veins of the Gicik mineralized system and is known as the original discovery vein. This N–S-trending vein segment is exposed immediately to the north of the Gicik Village (Figure 2.3). Its thickness varies from 5 to 10 meters with an exposed strike length of ~80 meters. The elevation of Q1 vein changes between 1120 and 1130 meters.

Alteration zonation is well developed around the Q1 vein, where mineralized siliceous vein laterally grades into intensely and later to moderately argillized volcanic wall-rocks (Figure 2.18). A large variety of hydrothermal silica textures were identified within the Q1 vein, which yielded most evident paragenetic information for the Gicik mineralized system. These include typical low-sulfidation textures such as colloform banding and lattice bladed with other hydrothermal textures including cockade, open-space filling textures, stockwork veinlets, and hydrothermal breccia. Eastern margin

of the vein is where these textures are better exposed. Hydrothermal brecciation is cut by colloform banding, while colloform banding is cross-cut by coarsely-crystalline quartz veinlets. Gold is mainly contained within colloform banded quartz-pyrite layers. Amethystic quartz is also locally present as a late stage phase in the Q1 vein (Figure 2.15c).



Figure 2.17. Field photograph of T Vein exposed near Taştepe Hill to the north of Gicik (497496E, 4430126N).

The southerly Q2 vein is 2–3 meters thick, and has an exposed strike length of about 27 meters length. This vein comprises two smaller veins merging at the southern end and forming the main vein segment (Figure 2.19). The Q2 vein is similar to the Q1 vein in terms of the variety of textures and mineralogy, and display colloform banding,

cockade textures, crustification, and hydrothermal brecciation. Argillic alteration developed near the siliceous vein margins in the lower agglomerate unit (Figure 2.19). Pyrite is the main ore mineral found in surface samples from the Q2 vein and it occurs as fine layers within colloform bands.

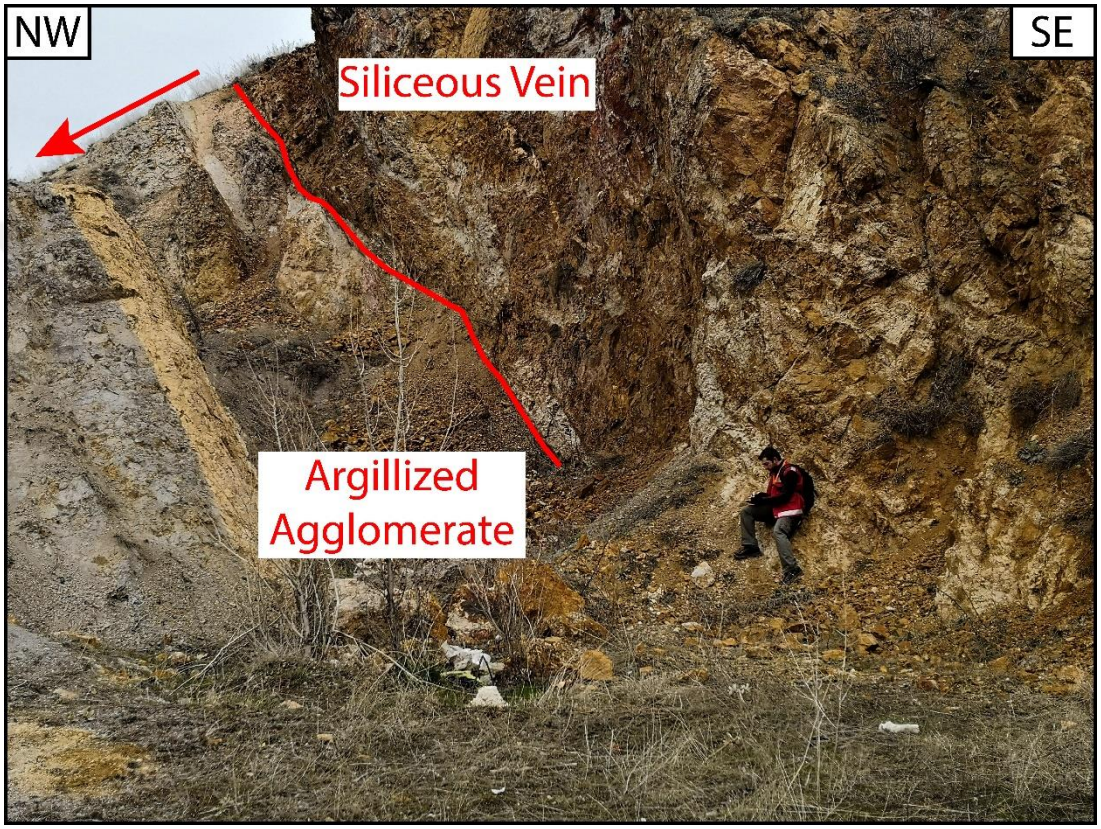


Figure 2.18. Field photograph of contact between argillized agglomerate and siliceous vein observed in the Q1 Vein at the north of Gicik Village (UTM Coordinates 497249 E, 4429198 N). Arrow indicates the decreasing intensity of argillic alteration.

2.3.3. East Veins

East Vein (Figure 2.3) is another important vein system in the study area and is subdivided into two as East1 and East2. Similar to the Q Vein, the East Vein, especially East2, is also rich in hydrothermal textures.



Figure 2.19. Field photograph of the Q2 Vein cross-cutting agglomerate and forming intense clay alteration (white color) (UTM Coordinates 497035 E, 4428873 N).

The East1 Vein (Figure 2.20) comprises blocks and boulders of silicified host rocks and small amounts of silica veins located around 497863E and 4429141N with an average elevation of 1140 meters. East1 Vein is oriented in the NE-SW direction, with an exposed strike length of up to 40 meters and its thickness varies between 1 and 3 meters. Still, the length and thickness estimates for this vein may be different than the actual due to the absence of well-preserved vein exposures. Because of the same reason, vein textures are not clear, in fact, the East 1 Vein itself appears more as an intensely-silicified volcanic rock, which was cut by thin quartz veins.

East2 Vein (Figure 2.21); however, includes a wide range of hydrothermal textures such as hydrothermal brecciation, stockwork veinlets, and dark gray colored massive

silica zones, where sulfide minerals are mostly concentrated as disseminations. Pyrite is detected in the surface samples, whereas arsenopyrite was detected under thin section. The East2 Vein is oriented in the NE-SW direction, has a thickness varying between 2 and 7 meters and has an approximate exposed strike length of 140 meters. East2 vein is a major vein which is composed of similarly oriented several relatively smaller and thinner veins. Altitude of the southern end of East2 vein is approximately 1150 whereas the northern end of East2 vein is around 1170 meters.

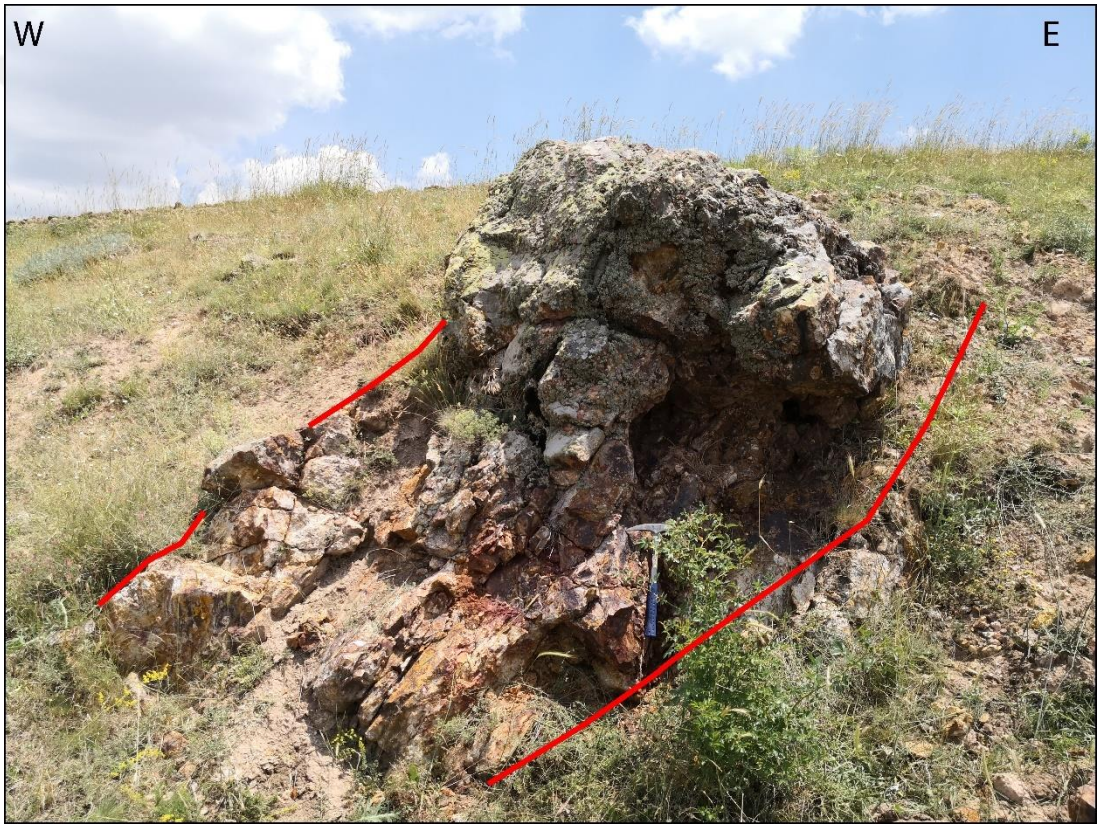


Figure 2.20. Field photograph of NW dipping (~70°) East 1 vein in the field (UTM Coordinates 497711 E, 4429129 N).



Figure 2.21. Field photograph of the NE–SW trending East2 Vein in the field (UTM Coordinates 497809 E, 4428866 N).

2.3.4. G Vein

The NNE-trending steeply-dipping (85°) G Vein (Figure 2.22) comprises 1 to 3 meters-thick, 10 to 60 meters long vein segments, primarily displaying colloform banding. Hosted by the lower agglomerate unit, the G Vein is exposed at a relatively lower elevation ranging from 1070 to 1130 meters. Thus, its surface exposures may represent relatively lower levels of the mineralized system compared to other vein sets.

The G vein returned the best assay results during Eurogold's drilling campaign including hole TD-8 with the most significant drill intercept averaging ~21.6 g/t Au over an 11 meter-long interval.

G Veins are also important for understanding the ore minerals since massive thick (2-5 cm) quartz veins and small fine-grained quartz veinlets give place to dark gray silicified zones with disseminated pyrite towards the deeper parts of the vein. As the depth increases, colloform bands and massive white colored quartz veins start to dominate the vein. At the deepest section of the vein, gray colored silicified zone with disseminated and very fine-grained pyrite was observed, which has been cut by 2–3 cm-thick white quartz veinlets (Figure 2.22b). Intergrown pyrite and tetrahedrite were identified within colloform quartz bands just at the south of the village.

2.3.5. Creek Vein

The name “Creek Vein” was used to denote the veins exposed at the southernmost section of the study area (Figure 2.3). One of these veins was exploited through open-pit mining by Koza Gold during 2009, thus leaving relatively less mineralized and smaller vein segment exposed. After the mining operations ceased, the company moved their main project facilities on top of the exploited vein. Therefore, a detailed observation of this vein could not be possible compared to the other studied veins.

The Creek Vein is the southernmost vein in the study area, where the elevation is the lowest (1060–1070 meters). It is NE-SW oriented with a thickness of 3–4 meters and an exposed strike length of 25 meters. Textures defining this vein is similar to the other veins throughout the study area, and these include open space filling, massive milky quartz veinlets.

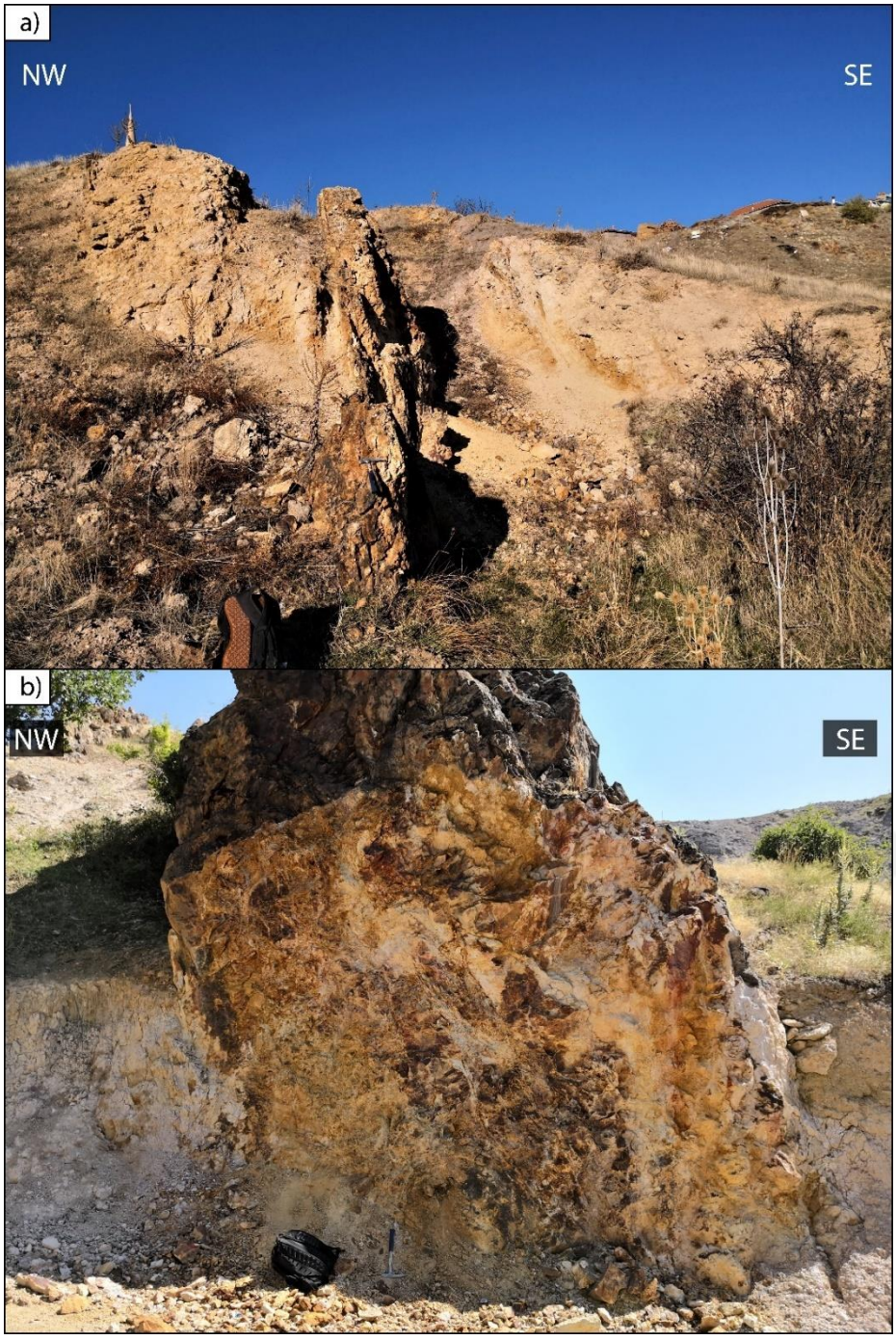


Figure 2.22. Outcrop images of the best exposed section of the NE-SW trending G Vein. a) Northern segment of G Vein exposed immediately to the south of Gicik village (UTM Coordinates 497333 E, 4428844 N), b) southern segment of the G Vein. Dark brown colored center is dominated by dark gray silicified zone, with disseminated pyrite, cut by thin, white colored quartz veinlets (UTM Coordinates 497389 E, 4428585 N).

2.4. Structure

Mineralization in the Gicik is strongly controlled by the structural framework of the study area. Two important deformation stages were identified during the field work (Figure 2.23). The first of these stages is the compressional stage responsible for northeast trending, strike–slip dominated reverse faults which appear to be the host of gold–bearing silica veins (Figure 2.24). These vein systems appear to be cut by E–W and NE–SW trending faults; however, this relation is only interpreted.

A total of 324 measurements were taken from 14 fault planes (Appendix H) around the veins and surrounding volcanic rocks and 14 paleostress configurations were constructed (Table 2.6). All paleostress reconstruction results are presented in Appendix G.

The analyses revealed that the fault slip measurements from strike-slip faults with reverse components have gently plunging (nearly horizontal) σ_1 axes (between 01 and 26°). The orientations of slickenlines developed on the fault planes were collected by a mobile application called eGEO Compass Pro.

It is clear that the trends of mineralized silica veins are consistent with the trends of the first set of major faults (NE-trending strike-slip oblique faults). The second set of faults cuts and offsets the veins. However, this conclusion was interpreted based on the orientation of the second fault set and the distribution of the vein segments.

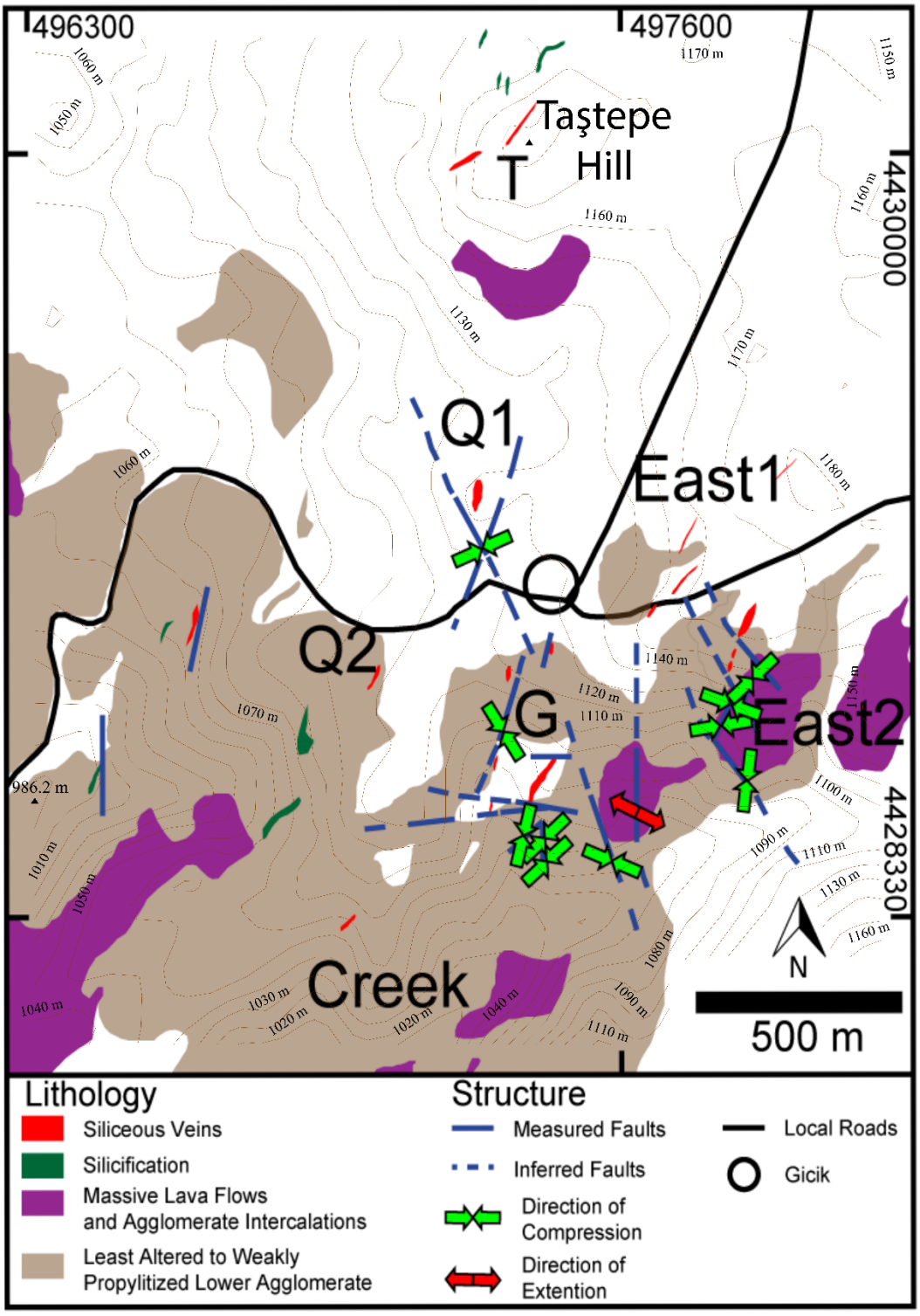


Figure 2.23. Paleostress reconstruction analysis results and their spatial distribution in Gicik.

Table 2.6. Summary of fault surface data from Gicik area.

ID	Easting	Northing	#	σ_1	σ_2	σ_3	r
Fault 1	497839	4428870	40	20/289	69/122	04/020	0,5
Fault 2	497402	4428630	53	17/010	73/181	02/279	0,5
Fault 3	497405	4428617	12	10/046	53/303	35/144	0,5
Fault 4	497382	4428657	23	06/194	07/103	81/323	0,58
Fault 5	497331	4428862	27	03/328	83/080	06/237	0,5
Fault 6	497414	4428660	15	26/057	43/174	36/307	0,51
Fault 7	497532	4428622	7	24/284	41/171	40/035	0,52
Fault 8	497609	4428714	20	72/038	17/201	05/292	0,5
Fault 9	497819	4428746	18	16/008	73/177	03/277	0,5
Fault 10	497809	4428866	30	01/082	49/173	41/350	0,5
Fault 11	497874	4428953	15	04/049	62/147	27/317	0,5
Fault 12	497251	4429237	44	05/249	44/151	45/341	0,5
Fault 13	496906	4437458	7	16/164	65/291	19/069	0,5
Fault 14	498824	4432646	3	02/226	77/323	13/135	0,49

(#: Number of samples, σ: Principle stress, r: Correlation coefficient)

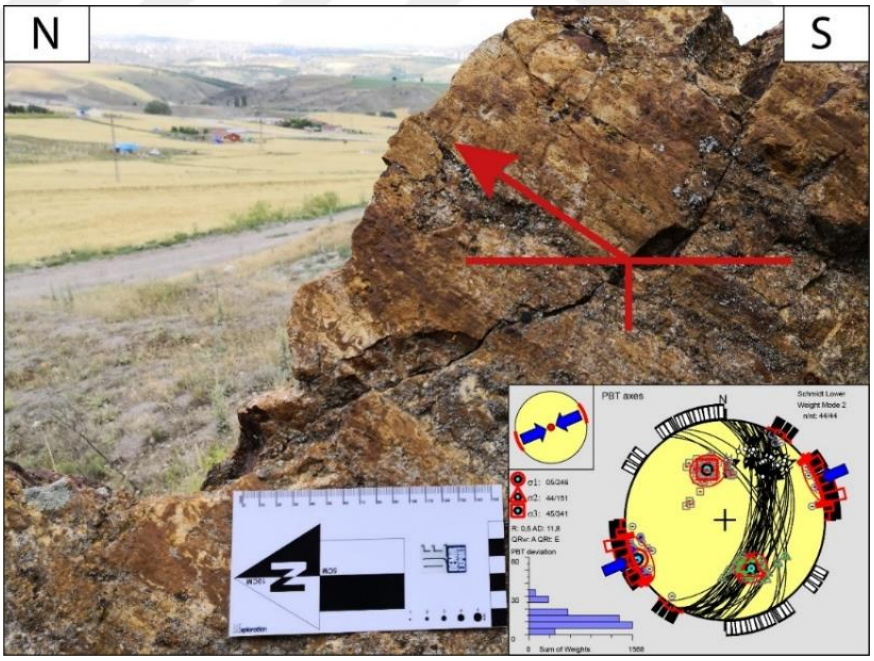


Figure 2.24. Oblique dextral fault with reverse component on the Q1 Vein located near the Gicik Village (UTM Coordinates 497248 E, 4429198 N). Paleostress reconstruction indicates compression along northeast–southwest direction.

CHAPTER 3

LITHOGEOCHEMISTRY

Four igneous rock samples, selected from a suite of least-altered and altered samples, were analyzed for their whole-rock geochemical compositions. Major, trace and rare earth element abundances were used to assess rock types, geochemical affinity (e.g., alkalinity), and tectonic setting. For plotting purposes, all major oxide abundances were recalculated to 100% on a volatile-free basis. The results of whole-rock geochemical analyses are presented in Table 3.1.

Table 3.1. Whole-rock geochemical data of least-altered and altered intermediate composition volcanic rock samples from Gicik.

Sample no.	**GCK-01**	**GCK-03**	**GCK-09**	**GCK-11**
Rock Type	**M**	**A**	**M**	**M**
SiO_2 (wt.%)	62.27	64.14	70.18	65.46
Al_2O_3	15.35	14.28	15.02	16.37
$Fe_2O_{3(T)}$	4.47	3.66	3.45	4.39
MnO	0.06	0.07	0.04	0.04
MgO	1.37	1.72	0.37	0.63
CaO	6.00	5.53	3.32	4.27
Na_2O	3.36	2.99	3.62	3.80
K_2O	1.38	2.44	2.65	2.60
TiO_2	0.70	0.63	0.58	0.81
P_2O_5	0.21	0.20	0.17	0.22
Loss-on-ignition	4.31	4.66	1.07	2.14
Total	99.49	100.30	100.50	100.70

M: Massive Lava Flows A: Agglomerate * in ppb

Table 3.1. (cont'd)

Sample no.	GCK-01	GCK-03	GCK-09	GCK-11
Rock Type	**M**	**A**	**M**	**M**
Ag (ppm)	< 0.5	< 0.5	< 0.5	< 0.5
Au*	< 1	< 1	1	< 1
As	4	3	3	3
Ba	923	606	567	488
Be	1	1	1	2
Bi	< 0.1	< 0.1	0.4	< 0.1
Br	< 0.5	< 0.5	< 0.5	< 0.5
Cd	< 0.5	< 0.5	< 0.5	< 0.5
Co	9.7	10.7	5.7	10.2
Cr	89.5	86	21.5	41
Cs	10.3	4.4	1.3	2.5
Cu	17	29	17	14
Ga	16	16	15	18
Ge	0.9	0.9	1.3	1.4
Hf	3.2	2.9	3	3.1
Hg	< 1	< 1	< 1	< 1
In	< 0.1	< 0.1	< 0.1	< 0.1
Ir*	< 1	< 1	< 1	< 1
Mo	< 2	< 2	< 2	2
Nb	12.4	10.5	12.1	16.1
Ni	40	40	14	19
Pb	12	13	11	10
Rb	37	51	64	63
S	0.004	0.004	0.003	0.003
Sb	1	0.6	1	0.9
Sc	9.75	8.05	5.15	8.65
Se	< 0.5	< 0.5	< 0.5	< 0.5
Sn	< 1	1	1	1
Sr	627	431	358	435
Ta	0.97	0.98	1.12	1.49
Th	8.98	8.87	9.73	9.96
U	1.3	2.01	2.32	2.86
V	66	77	42	80
W	< 1	< 1	< 1	< 1

M: Massive Lava Flows A: Agglomerate * in ppb

Table 3.1. (cont'd)

Sample no.	GCK-01	GCK-03	GCK-09	GCK-11
Rock Type	**M**	**A**	**M**	**M**
Y	12.00	12.00	10.00	13.00
Zn	39	48	28	51
Zr	144	127	133	143
La	27.3	24.8	24.9	26.6
Ce	46.5	42	41.3	45.1
Pr	4.66	4.17	3.98	4.39
Nd	16.6	14.5	14	15.4
Sm	3.15	2.67	2.36	3.18
Eu	0.941	0.788	0.723	0.931
Gd	2.73	2.15	2.08	2.71
Tb	0.41	0.35	0.29	0.42
Dy	2.41	2.28	1.92	2.5
Ho	0.45	0.44	0.38	0.49
Er	1.37	1.27	1.13	1.48
Tl	0.37	0.36	0.41	0.26
Tm	0.197	0.193	0.173	0.215
Yb	1.29	1.24	1.17	1.32
Lu	0.196	0.212	0.171	0.202

M: Massive Lava Flows A: Agglomerate * in ppb

3.1.1. Major Element Geochemistry

All of the volcanic rock samples from Gicik are intermediate to felsic in composition with SiO_2 abundances ranging between 65.1 and 70.9 wt.% (normalized to 100% volatile-free compositions). All samples are metaluminous except one sample that appears slightly peraluminous (Figure 3.1). The samples are dacitic in composition with calc-alkaline affinity as indicated by total alkali (Na_2O+K_2O) versus SiO_2 (TAS) diagram and total alkali (Na_2O+K_2O)-$FeO_{(t)}$-MgO (Figure 3.2) diagram of Irvine and Baragar (1971).

Two of the samples plot within the field of medium-K calc-alkaline series rocks on the K_2O versus SiO_2 diagram, whereas the other two samples lie along the border between medium-K and high-K fields (Figure 3.3).

Despite the limited number of analyses, major and minor oxide compositions of all samples were plotted against their SiO_2 contents (Figure 3.4). The samples broadly show inverse correlations between SiO_2 and most major and minor oxides including Al_2O_3, MgO, FeO, CaO, TiO_2, and P_2O_5 (Figure 3.4), likely indicating fractionation of Fe- and Mg-rich mafic minerals as well as feldspars. Such trends, however, were not observed for K_2O and Na_2O (Figure 3.4), suggesting mobility of alkali elements due to hydrothermal alteration.

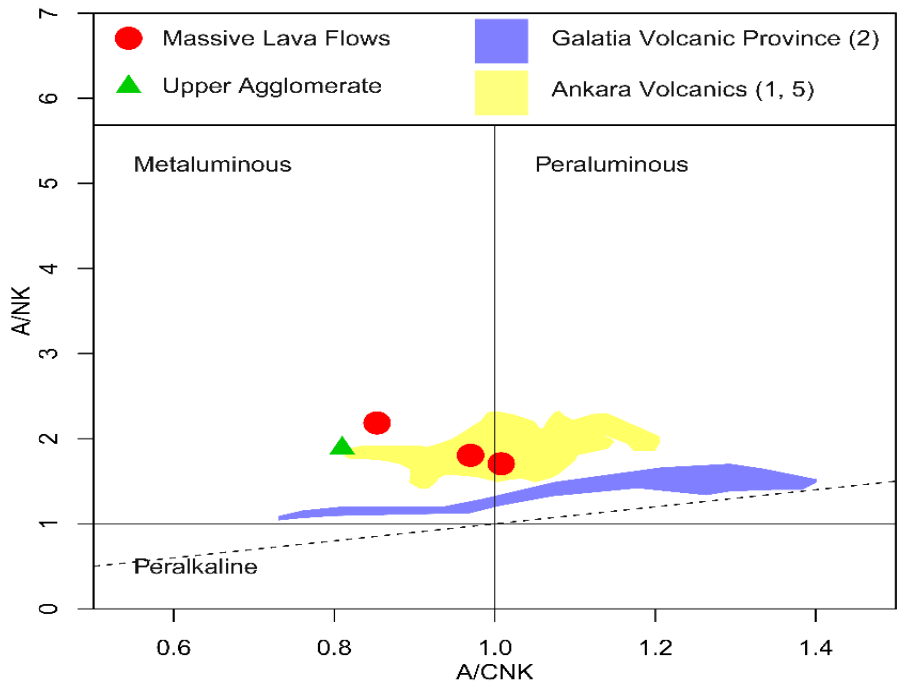


Figure 3.1. Plots of the least-altered and altered Gicik samples on the $Al_2O_3/CaO+Na_2O+K_2O$ versus Al_2O_3/Na_2O+K_2O diagram (Shand, 1943). Data for comparison with regional volcanic systems are from (1) Seyitoğlu and Büyükönal (1995), (2) Tankut et al. (1998) and (5) Tankut (1985).

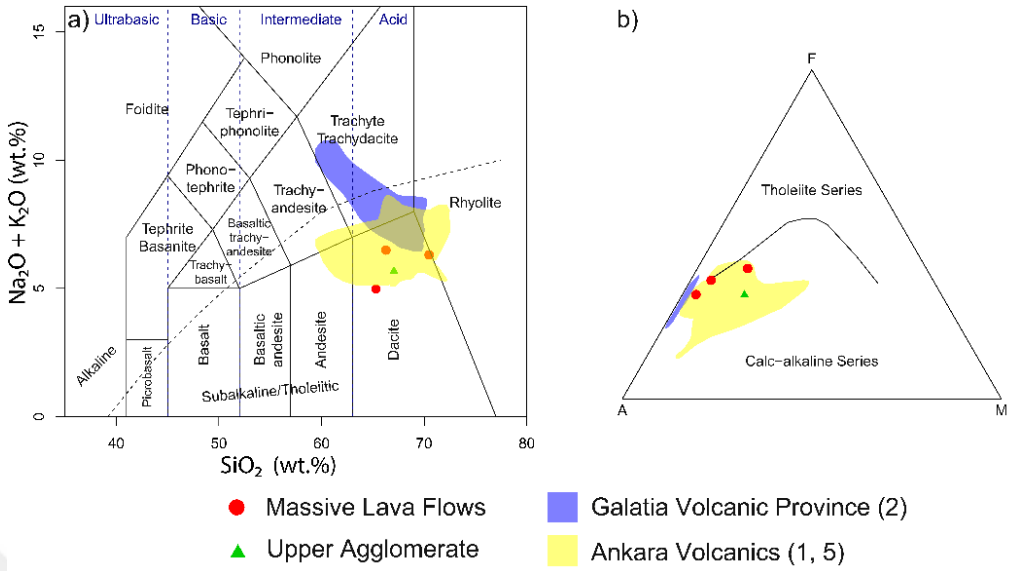


Figure 3.2. Plots of the least-altered and altered samples from Gicik on rock classification diagrams. a) Total alkali versus silica diagram (Le Bas et al., 1968), b) total alkali (Na_2O+K_2O)-$FeO_{(t)}$-MgO diagram (Irvine and Baragar, 1971).

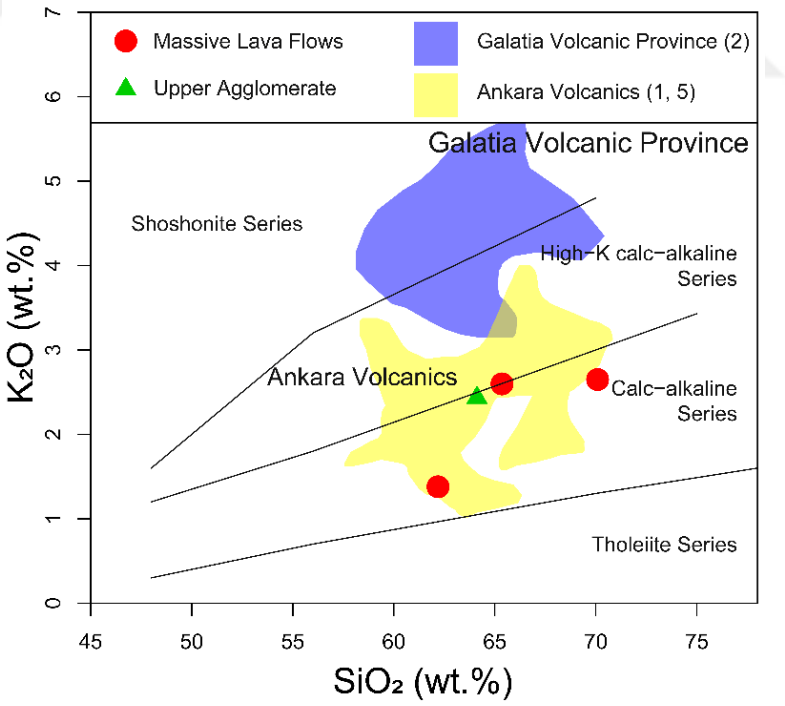


Figure 3.3. Plots of the least-altered and altered volcanic rocks from Gicik on K_2O versus SiO_2 diagram (Peccerillo and Taylor, 1976).

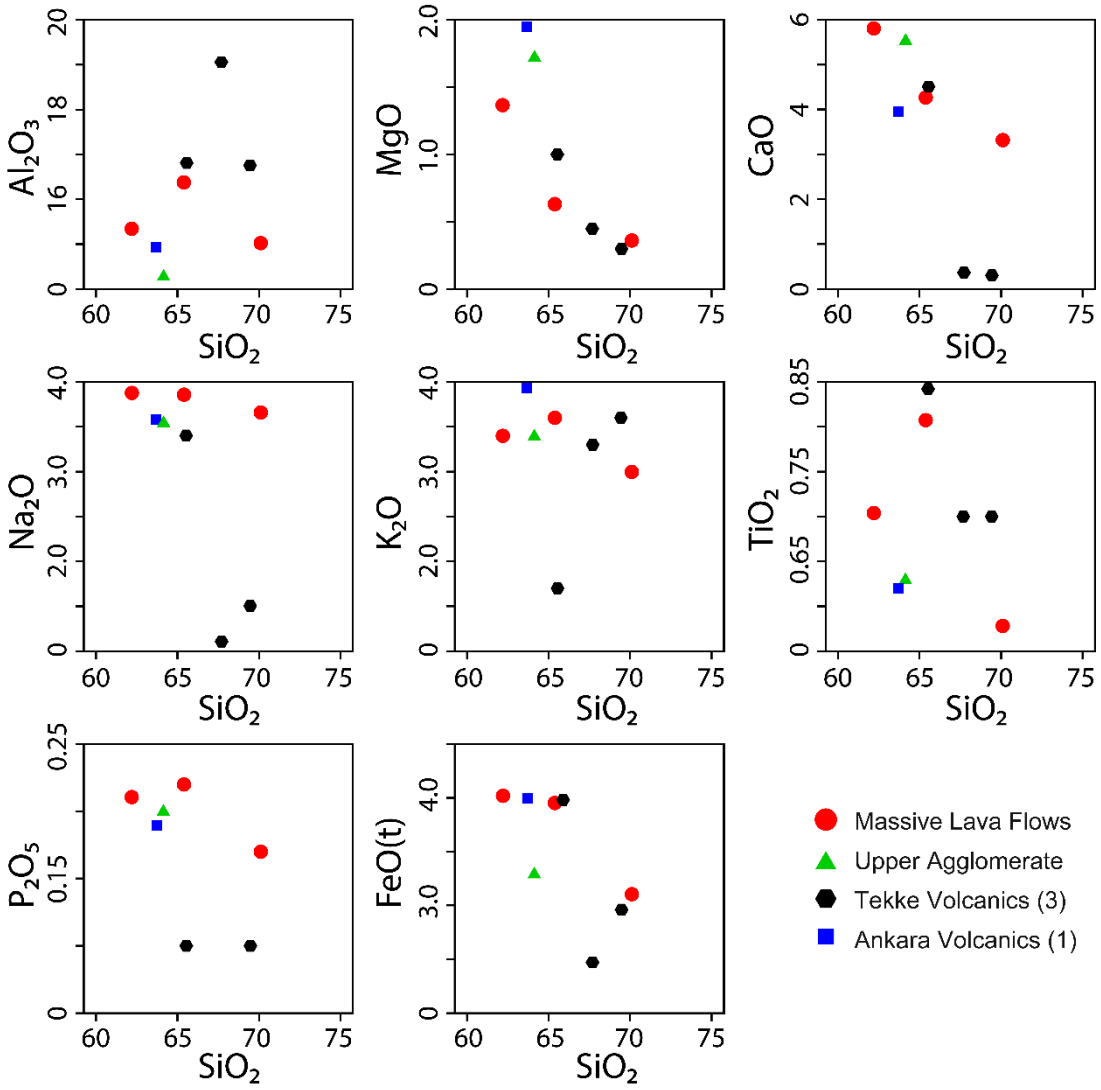


Figure 3.4. Harker variation diagrams for the major elements in the Gicik intermediate rocks. Reference data are from (1) Seyitoğlu and Büyükönal (1995) and, (3) Besbelli and Varol (2002). All values are in wt%.

3.1.2. Trace Element Geochemistry

Multi-element variation diagrams were plotted in order to understand the compositional characteristics of the igneous host rocks of the Gicik mineralized system. Primitive-mantle normalized trace element diagram is shown in Figure 3.5, whereas chondrite-normalized rare earth element (REE) diagram is shown in Figure

3.6. All normalization values were taken from Sun and McDonough (1989). In both trace element and rare earth element diagrams, both least-altered and altered samples show broadly similar enrichment or depletion levels, and they also display almost identical patterns (Figures 3.5 and 3.6), suggesting that element mobility did not have a significant effect on trace and rare earth element abundances.

On the primitive-normalized trace element diagram, all samples show relative enrichments in incompatible elements including large-ion lithophile elements (LILE) such as K, Rb, Cs, Sr, and Ba (Figure 3.5). Prominent negative anomalies for high field strength elements (HFSE) including Ta, Nb, and Ti (Figure 3.5) on the other hand are characteristic of subduction-related magmas (Gill, 1981; Brenan et al., 1994). In addition, observed depletions in Ti and P (Figure 3.5) may be indicative of fractionation of mineral phases such as magnetite, hornblende, and apatite.

The Gicik samples are relatively enriched in light rare earth elements (LREE) relative to medium (MREE) and heavy rare earth elements (HREE) on a C1 chondrite-normalized diagram (Figure 3.6). MREE are usually compatible with hornblende and titanite, whereas HREE are compatible with garnet and zircon, and to a lesser extent in other mafic silicate mineral phases. This may explain the observed downward sloping pattern in Figure 3.6. Slight negative Eu anomalies (Figure 3.6) on the other hand are suggestive of plagioclase fractionation.

3.1.3. Tectonic Discrimination Diagrams

Several tectonic discrimination diagrams were plotted in order to reveal the possible tectonic setting of the samples from the study area. Ti versus Zr diagram (Pearce, 1982; Figure 3.7) indicates an island arc environment. However, Ta versus Yb (Pearce et al., 1984; Figure 3.8a) and Nb versus Y (Pearce et al., 1984; Figure 3.8b) diagrams suggest volcanic arc and syn-collisional tectono-magmatic environment. Trivariate diagram of Harris et al. (1986; Figure 3.8c), on the hand, implies late stage magmatism in a post-collisional setting.

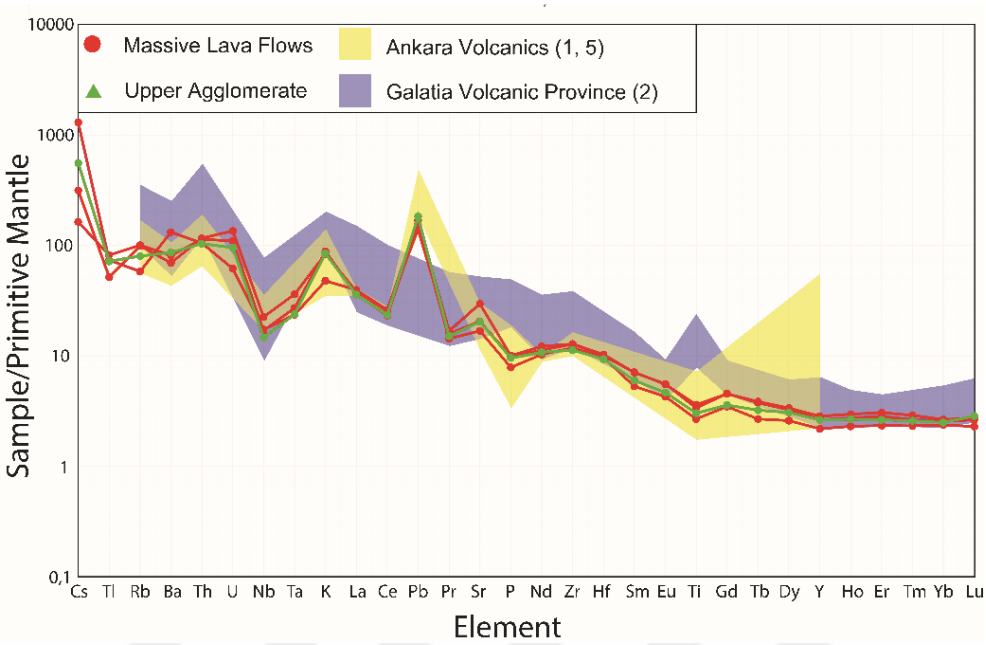


Figure 3.5. Primitive mantle-normalized multi–element diagram of volcanic samples. Normalization values are from Sun and McDonough (1989).

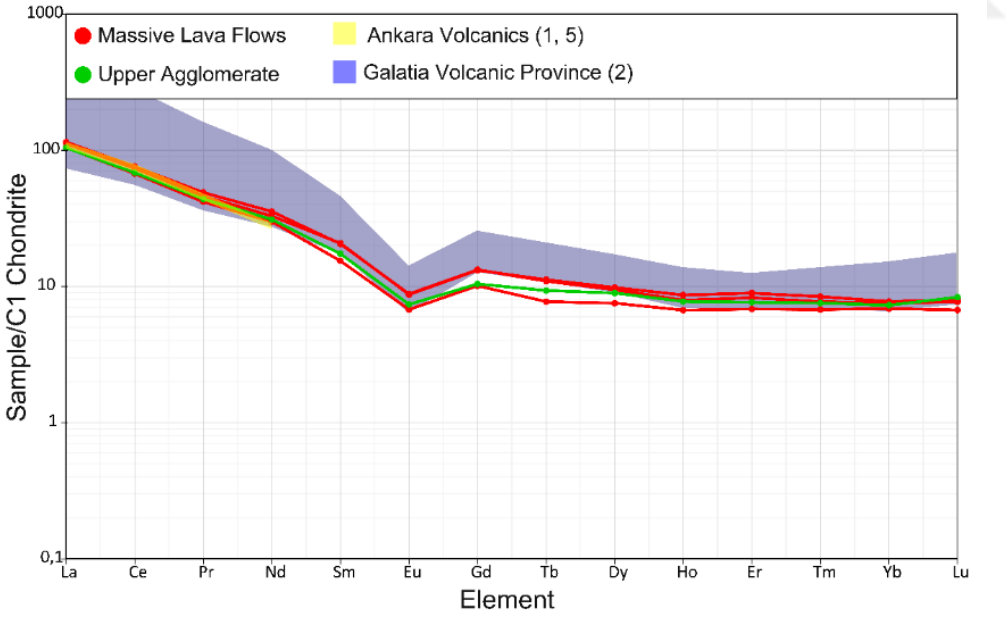


Figure 3.6. C1 Chondrite-normalized rare earth element diagram of volcanic samples. Normalization values are from Sun and McDonough (1989).

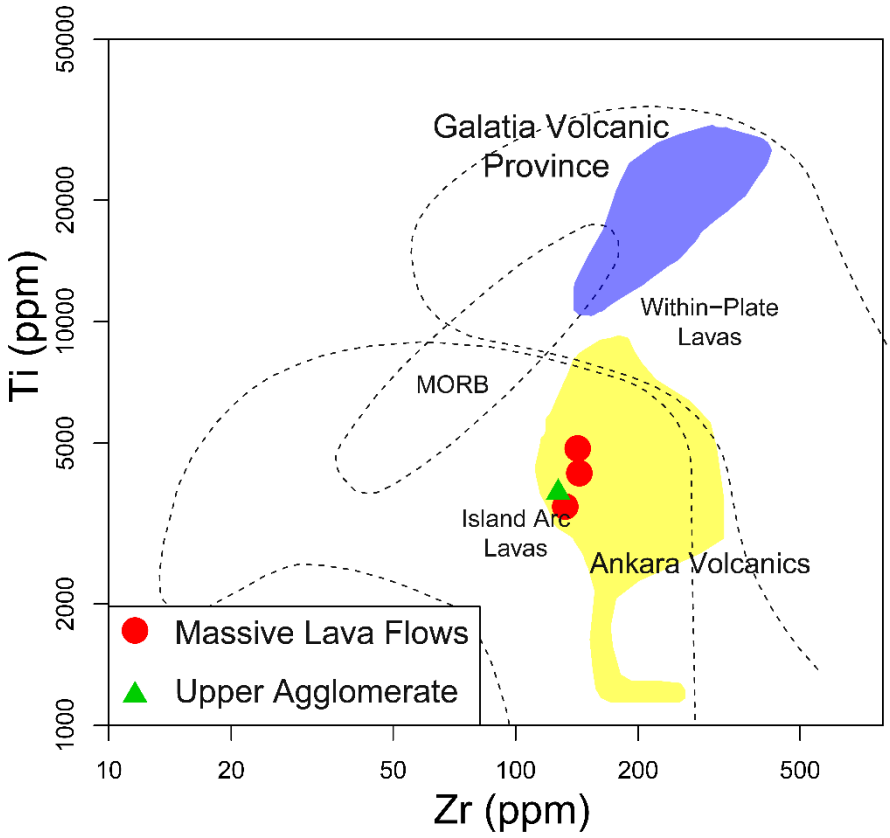


Figure 3.7. Plots of the Gicik samples on the Ti versus Zr tectonic discrimination diagram (Pearce, 1982).

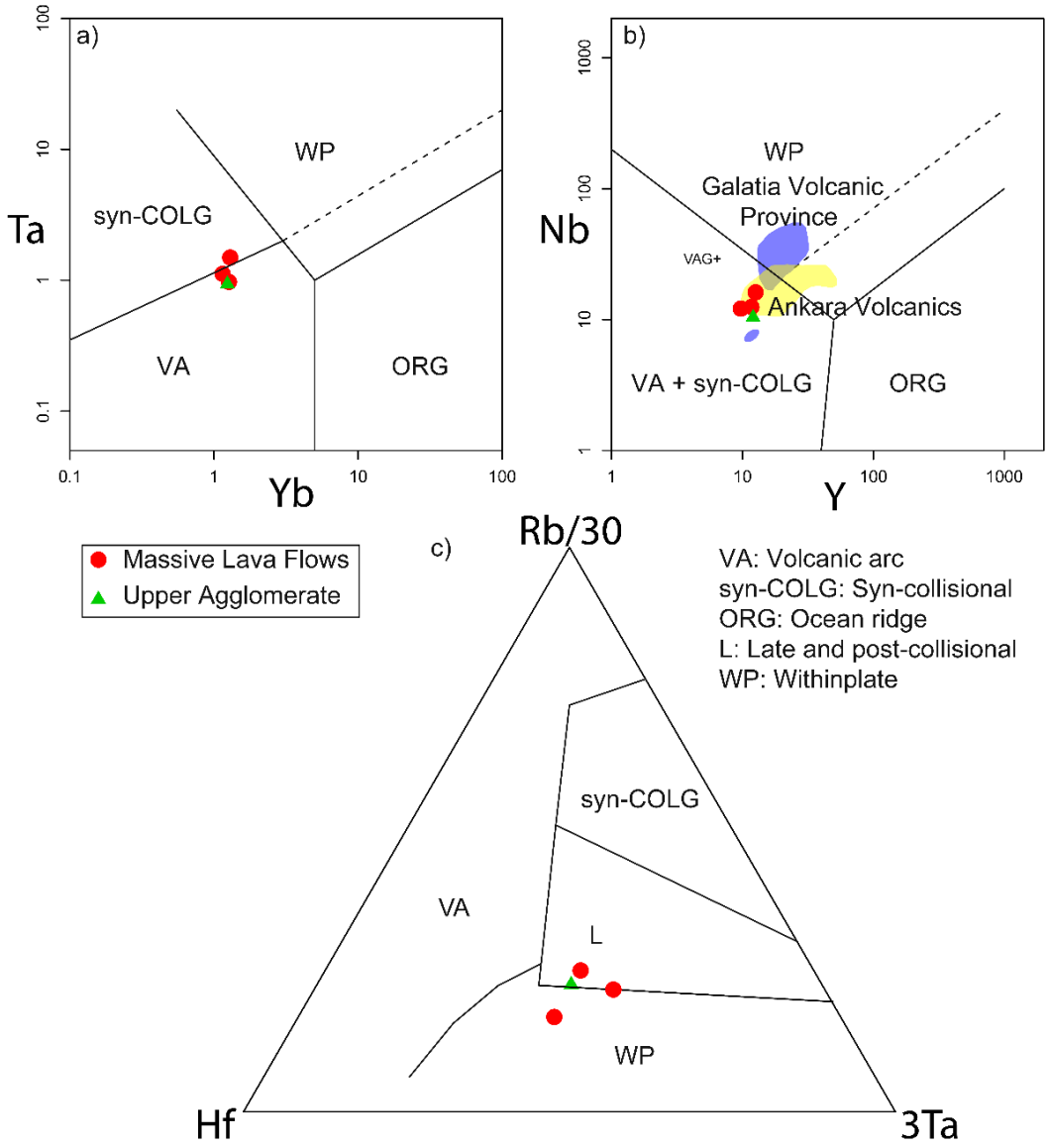


Figure 3.8. Plots of least-altered and altered igneous rocks from Gicik on tectonic discrimination diagrams. a) Ta versus Yb diagram (Pearce et al., 1984), b) Nb versus Y diagram (Pearce et al., 1984), c) Rb/30-Hf-3Ta trivariate diagram (Harris et al., 1986).

CHAPTER 4

MINERALIZATION AND HYDROTHERMAL ALTERATION

4.1. Mineralization

Gicik gold deposit contains series of silicified hydrothermal veins. Episodic hydrothermal activity is evident in these veins since of silica input are responsible for the formation of these veins and mineralization. In order to understand the evolution of this system, a detailed petrographic investigation of siliceous veins and altered igneous wall-rock was carried out.

4.1.1. Ore Mineralogy

The ore mineralogy of the mineralized samples from the surface is characterized by a number of sulfide mineral species, but the overall sulfide contents of veins are quite low (<5%). However, the shallow portions of the veins have undergone supergene weathering, and consequently limited information on the hypogene mineral assemblages could be obtained from surface samples.

The predominant ore mineral in all mineralized veins is pyrite (Figures 4.1a and 4.1b), which is intergrown in some vein segments with arsenopyrite (Figure 4.1b) and/or tetrahedrite (Figure 4.1c). Pyrite commonly occurs as colloform bands together with fine- to medium-grained quartz and also as disseminations in the silicified wall-rocks in close proximity of siliceous (Figures 4.2c, 4.2d, 4.2e and 4.2f). Pyrite grains (20-60 μm) are usually euhedral with cubic or pyritohedron forms (Figures 4.1a and 4.2d). Slight anisotropy observed in many of the pyrite crystals suggest presence of at least minor amounts of arsenic, which was further confirmed through EPMA studies (Table 4.1; see Appendix I for full data). In argillized wall-rocks disseminated pyrites have been leached out likely due to acidic nature of hydrothermal fluids, whereas in

silicified veins it has been oxidized into Fe-oxide phases such as hematite and goethite (Figure 4.1a).

Arsenopyrite was found as intergrown with pyrite, and occurs as rhombic or lozenge-shaped grains with sizes ranging between 5 and 20 microns in diameter. It is present as disseminated grains within siliceous veins of G and East Veins.

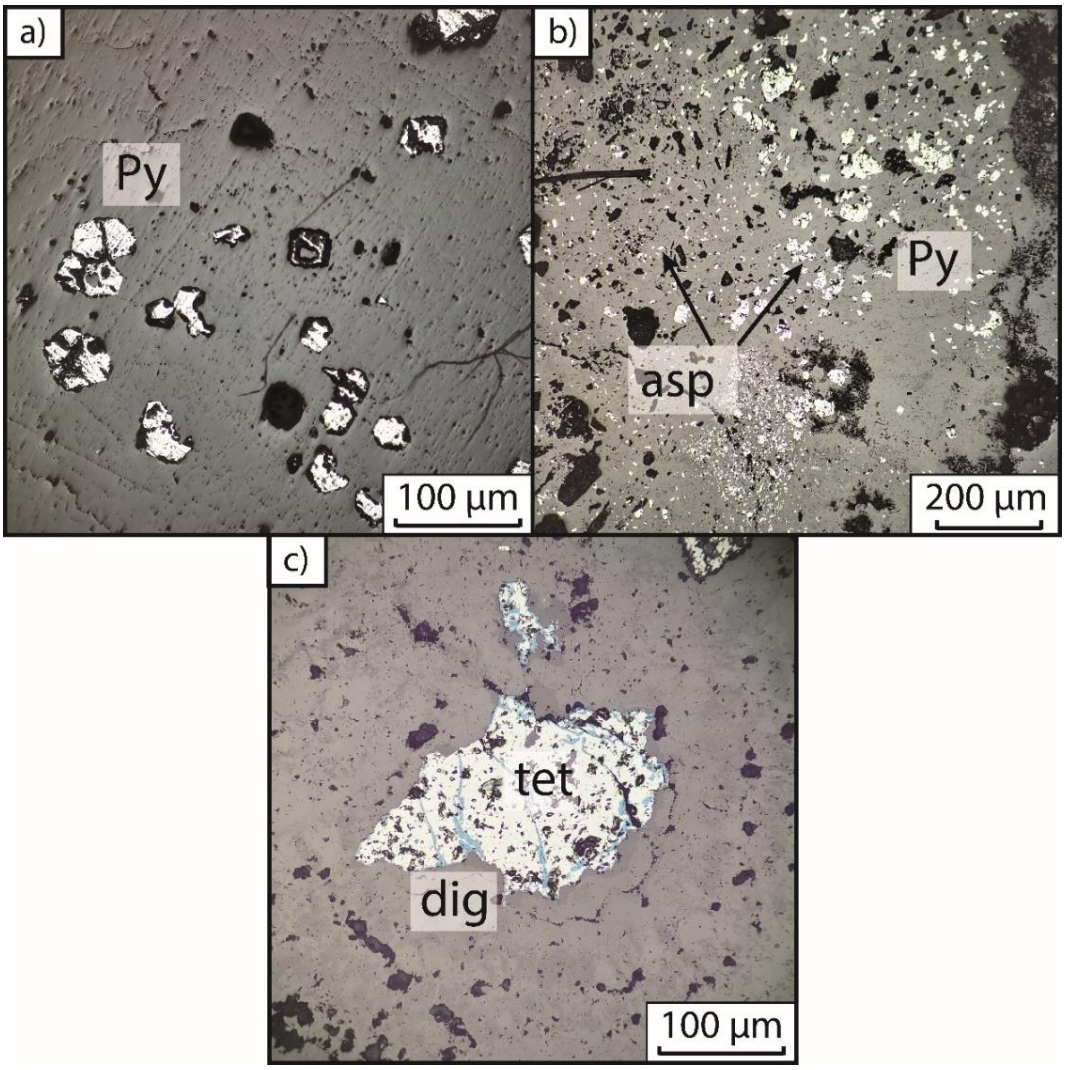


Figure 4.1. Microphotographs of a) oxidized pyrite (py; center) with pyrite (left; Sample GCK-38, reflected light), b) pyrite and arsenopyrite (apy; Sample GCK-61, reflected light) and c) argentiferous tetrahedrite mineral (tet) partially oxidized into digenite (dig) along microfractures (Sample GCK-64-2, reflected light).

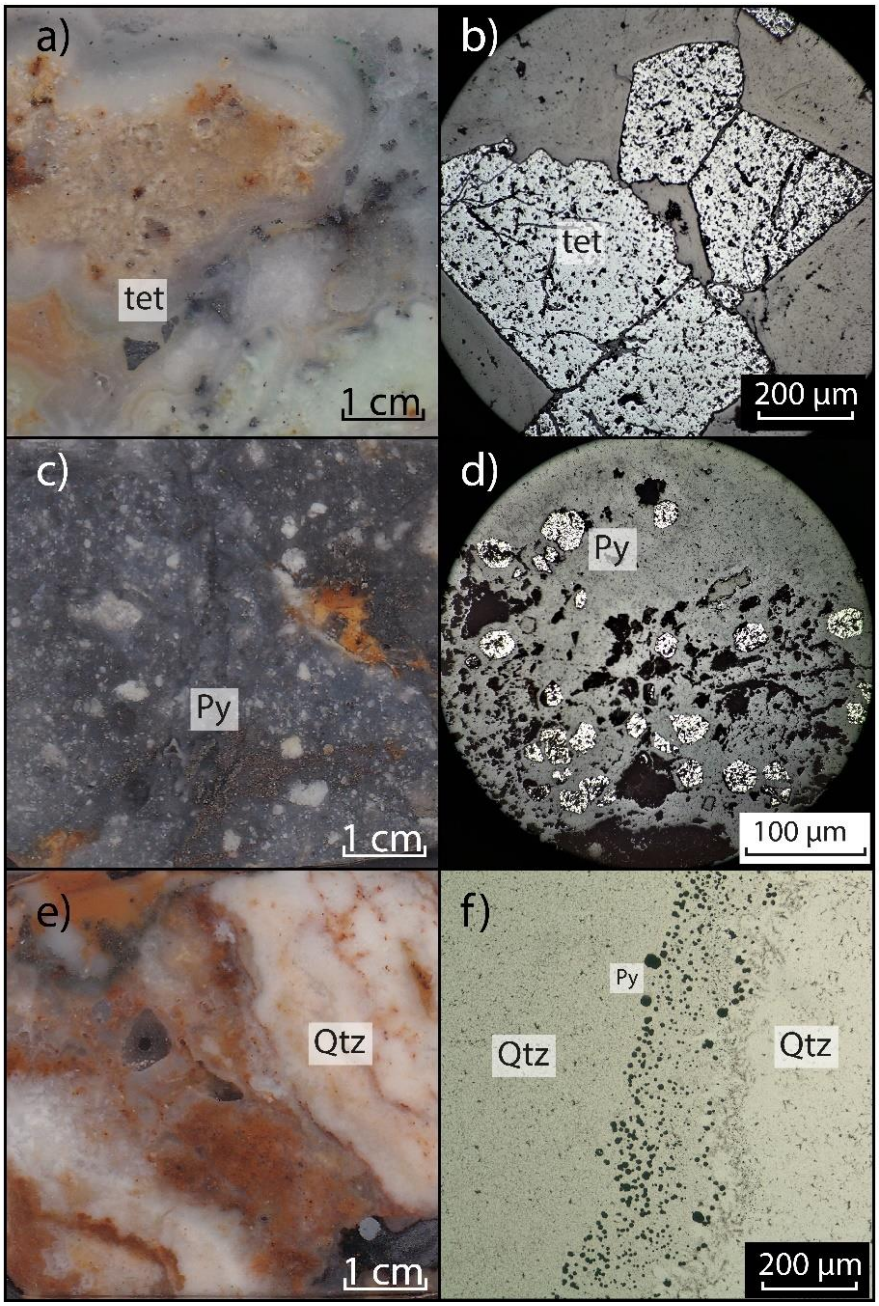


Figure 4.2. Ore minerals of Gicik epithermal system: a) close-up view of tetrahedrite in colloform banded sample from G Vein (Sample GCK-64-2), b) microphotograph of large euhedral tetrahedrite grain (Sample GCK-64-2, reflected plane polarized light), c) close-up view of disseminated pyrite and arsenopyrite in silicified volcanic wall-rock (Sample GCK-61), d) microphotograph of pyrite in silicified wall-rock (Sample GCK-61, reflected plane polarized light), e) close-up view of colloform banding (Sample GCK-32-A), and f) microphotograph of colloform banded quartz-pyrite (Sample GCK-32-A, PPL).

Euhedral to subhedral argentiferous tetrahedrite was identified in surface samples collected particularly from the G Vein. Here, Ag-tetrahedrite occurs as large (200–800 microns) euhedral crystals of rhombohedral form, alongside pyrite and quartz in colloform bands (Figure 4.2a). Weak surface oxidation resulted in development of digenite especially along fractures and rims of Ag-tetrahedrite grains (Figure 4.1c).

Table 4.1. Mineral geochemistry results of pyrite (py) and arsenopyrite (apy). All values are reported in wt%.

Sample No.	G61-1-1 py	G61-1-2 py	G61-1-3 py	G61-1-4 py	G61-2-2 py	G61-3-1 py	G61-3-2 py	G61-3-3 py	G642-5 py	G61-2 apy
As	0.008	0.050	0.034	0.864	0.021	0.034	0.123	0.727	0.180	1.627
Se	0.002	0.003	0.012	0.007	0.013	0.012	0.009	0.018	0.018	0.015
S	53.14	53.35	53.08	52.80	53.49	53.08	53.30	53.39	53.38	34.38
Sb	0.006	0.001	0.003	0.045	0.000	0.003	0.065	0.010	0.004	0.051
Mo	0.00	0.00	0.00	0.00	0.00	0.00	0.00	0.00	0.00	0.00
Cu	0.008	0.029	0.00	0.123	0.00	0.00	0.007	0.049	0.009	0.048
Pb	0.00	0.00	0.00	0.00	0.00	0.00	0.00	0.00	0.00	0.00
Zn	0.021	0.023	0.007	0.00	0.008	0.007	0.019	0.007	0.011	0.006
Fe	45.89	45.65	45.08	45.45	46.03	45.08	45.69	45.69	46.36	29.91
Hg	0.00	0.00	0.00	0.00	0.00	0.00	0.00	0.00	0.00	0.00
Co	0.00	0.00	0.00	0.00	0.00	0.00	0.00	0.00	0.00	0.00
Bi	0.00	0.00	0.00	0.00	0.00	0.00	0.00	0.00	0.00	0.00
Cd	0.012	0.030	0.013	0.011	0.005	0.013	0.014	0.009	0.010	0.007
Te	0.010	0.00	0.00	0.00	0.001	0.00	0.002	0.004	0.004	0.008
Ag	0.003	0.00	0.021	0.00	0.003	0.021	0.001	0.005	0.004	0.010
Au	0.002	0.00	0.003	0.041	0.016	0.003	0.010	0.007	0.007	0.015
Total	99.11	99.14	98.26	99.34	99.59	98.26	99.21	99.91	99.98	66.08

No native gold or silver were identified in any of the surface samples. On the other hand, up to several ppm gold was detected in all aforementioned sulfide minerals during EPMA studies (see Table 4.2 and Appendix J). Pyrite and arsenopyrite also contains similar levels of silver (Table 4.1), but most silver in studied samples is contained within argentiferous tetrahedrite (up to 8.5 wt.%; Table 4.1). Argentiferous

tetrahedrite is also characterized by elevated levels of Zn (up to 7.6 wt.%; Table 4.2). Se is another element which was constantly detected in all sulfide minerals, but it is particularly enriched in some of the argentiferous tetrahedrite with abundances reaching close to 1 wt.% (Table 4.2). In contrast, Te, another trace metal characteristic of epithermal systems, is either absent in sulfide minerals from Gicik veins or is present in very low amounts (Table 4.2).

Table 4.2. Representative EMPA compositions of tetrahedrites from Gicik. All values are reported in wt%.

Sample No.	G641-1	G641-2	G641-4	G641-6	G642-1	G642-2	G642-3	G642-4
As	5.00	5.27	5.12	4.29	4.29	7.12	7.06	5.50
Se	0.3525	0.3440	0.3541	0.7579	0.7579	0.3291	0.3307	0.4336
S	25.02	25.20	24.82	24.19	24.19	25.31	25.21	25.13
Sb	23.99	24.29	22.20	19.61	19.61	23.86	24.10	21.52
Mo	0.00	0.00	0.00	0.00	0.00	0.00	0.00	0.00
Cu	37.01	37.37	38.22	35.37	35.37	37.94	37.81	39.29
Pb	0.00	0.00	0.00	0.00	0.00	0.00	0.00	0.00
Zn	6.66	6.82	6.17	4.88	4.88	7.43	7.45	5.97
Fe	0.0980	0.1022	0.0803	0.0130	0.0130	0.0824	0.0802	0.0557
Hg	0.0027	0.00	0.00	0.2078	0.2078	0.0057	0.0062	0.0065
Co	0.0068	0.0012	0.00	0.0044	0.0044	0.0025	0.00	0.00
Bi	0.00	0.00	0.0033	0.0254	0.0254	0.00	0.00	0.00
Cd	0.3043	0.2960	0.3195	0.5903	0.5903	0.3386	0.3395	0.2560
Te	0.00	0.00	0.3080	0.00	0.00	0.00	0.00	0.0472
Ag	2.11200	1.60500	1.97000	7.09500	7.09500	0.60543	0.72527	0.50858
Au	0.02430	0.01185	0.01234	0.00200	0.00200	0.01242	0.00787	0.01117
Total	100.58	101.29	99.57	97.02	97.02	103.03	103.12	98.72

4.1.2. Hydrothermal Alteration

At Gicik, although gold mineralization is limited to narrow vein segments in a restricted area near the town of Gicik, the hydrothermal system presents a large alteration footprint almost over the entire study area, manifested by widespread

hydrothermal alteration of volcanic lithologies. Within the scope of this thesis, hydrothermal alteration was only followed about 2 km to the south of Gicik, but it probably extends towards Hüseyingazi Hill located farther south.

Three major alteration types have been identified in the field and also during laboratory studies. These include propylitic alteration (Figure 4.3a and Figure 4.3b), argillic alteration (Figures 4.3c, 4.3d, 4.4a and 4.4b), and silicification (Figures 4.4a and 4.4b).

Propylitic alteration has developed regionally in the entire volcanic sequence, and even the least-altered volcanic units show some degree of chlorite (after ferro-magnesian minerals), epidote, and carbonate replacement with minor disseminated pyrite. However, the intensity of propylitic alteration increases significantly in the vicinity of mineralized veins, with almost complete replacement of the original volcanic lithologies by an alteration assemblage of chlorite-epidote-carbonate-quartz-pyrite.

Various types of silicification, readily characterized by discrete quartz forms, developed along mineralized veins (Figures 4.5 and 4.6). Most veins have cores consisting of massive milky white quartz, whereas colloform banded veins display alternating layers of very fine-grained to medium-grained quartz. In low-sulfidation epithermal systems, silica supersaturated hydrothermal fluids usually precipitate out cyclic layers of amorphous or cryptocrystalline silica (e.g., chalcedony, opaline silica) at temperatures <200°C. However, such silica phases are often metastable and recrystallize into quartz upon abrupt changes in the physico-chemical parameters (primarily temperature) of the hydrothermal system (Fournier, 1985). Recrystallization into quartz is also evident in colloform banded veins in Gicik. Quartz varieties similar to those observed in colloform banded veins are also present as cement material in hydrothermal breccias as well as in lattice bladed aggregates (developed after calcite) associated with boiling hydrothermal fluids. In some veins (East 2 and G), a dark gray variety of quartz was observed instead of massive milky

quartz, and this dark gray quartz is associated with the common pyrite-arsenopyrite assemblage. Relatively higher-grade gold-silver mineralization at Gicik is intimately related either with the dark gray quartz-sulfide veins or with colloform banded quartz-pyrite-tetrahedrite veins.

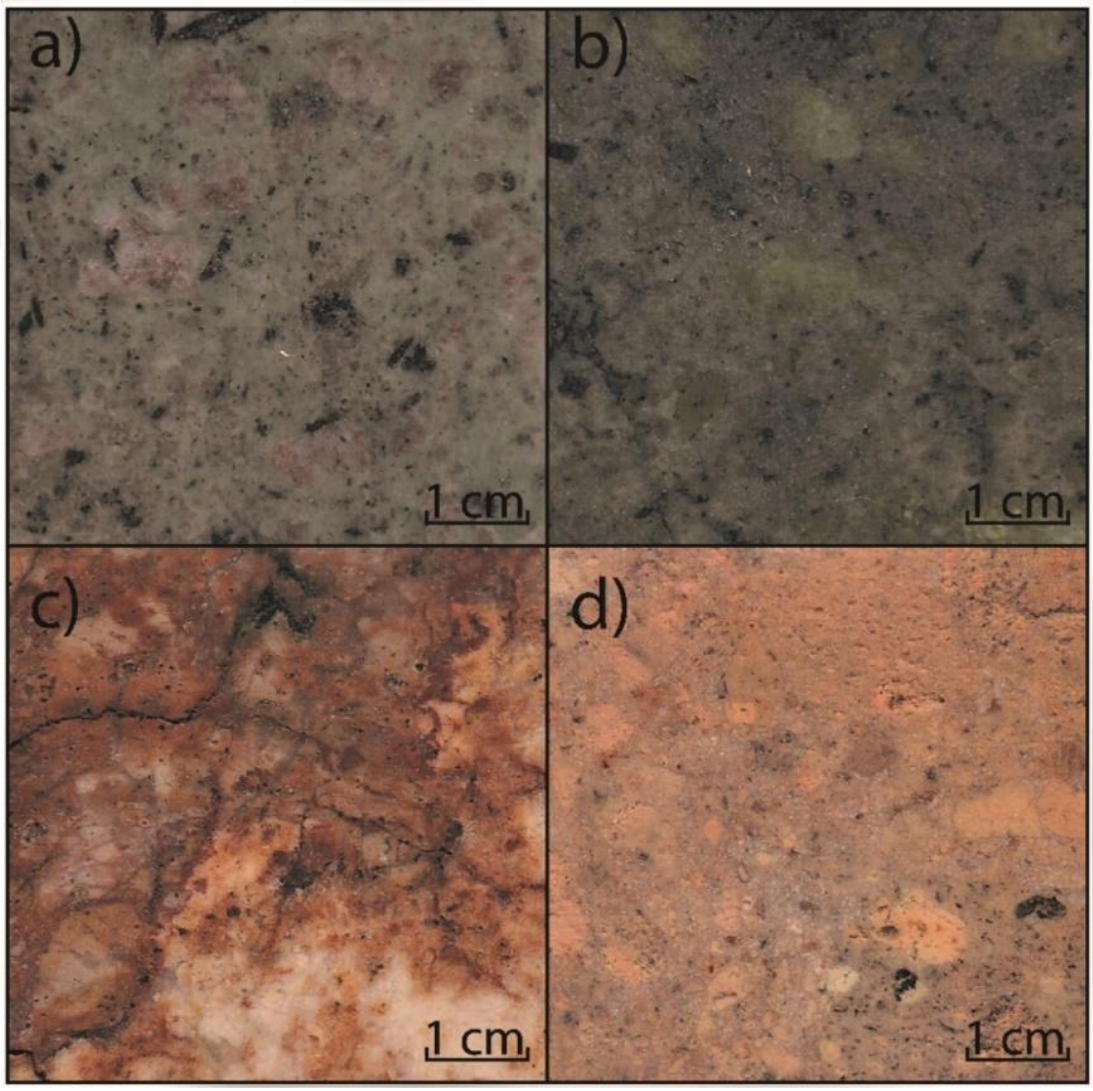


Figure 4.3. Hand specimens of altered samples; a) epidote-chlorite-carbonate altered agglomerate (Sample GCK-35), b) epidote-chlorite-carbonate alteration (Sample GCK-10), c) argillic-altered (quartz-clay) volcanic rock with Fe-oxides after pyrite oxidation (Sample GCK-27), and d) argillic-altered (clay) volcanic rock (Sample GCK-24).

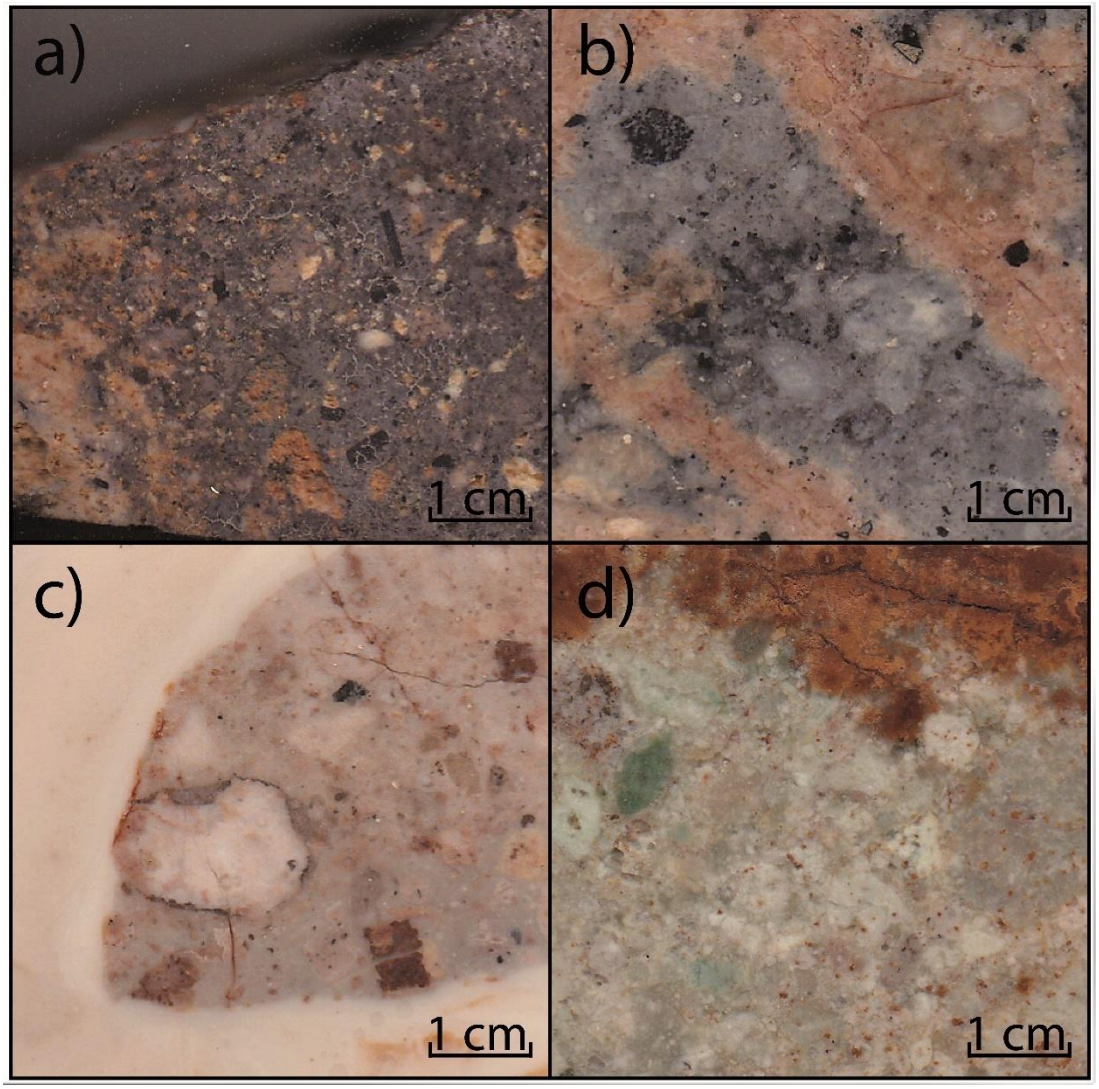


Figure 4.4. Hand specimens of altered samples. a) slightly argillized volcanic rock (Sample GCK-20), b) argillic alteration (Sample GCK-44-A), c) silicified agglomerate (Sample GCK-44-B) and d) silicified agglomerate (Sample GCK-40).

Amethystic quartz and vitreous coarse-grained quartz, identified as late stage open-space filling phases in siliceous veins, mark the final stage of silica addition into the system, probably at relatively higher temperatures.

Argillic alteration, represented by quartz-clay/sericite±adularia assemblages developed throughout immediate volcanic wall-rocks adjacent to the siliceous veins,

mainly in the central and southern parts of the study area (Figure 2.3). Argillic-altered volcanic rocks have bleached light gray to white colors, and are commonly coated with Fe-(hydr)oxide phases due to surface oxidation of sulfides, particularly of pyrite (Figure 4.7). Rare adularia (hydrothermal K-feldspar; Figure 4.8b) was observed in colloform banded vein samples collected from the G Vein, but this mineral is usually absent in other surface samples. Common clay mineral phases, as detected by XRD analyses, developed proximal to the mineralized veins are kaolinite, illite, and minor smectite (Appendix K), whereas relatively coarse-grained muscovitic sericite (Figure 4.8d) was also locally observed.

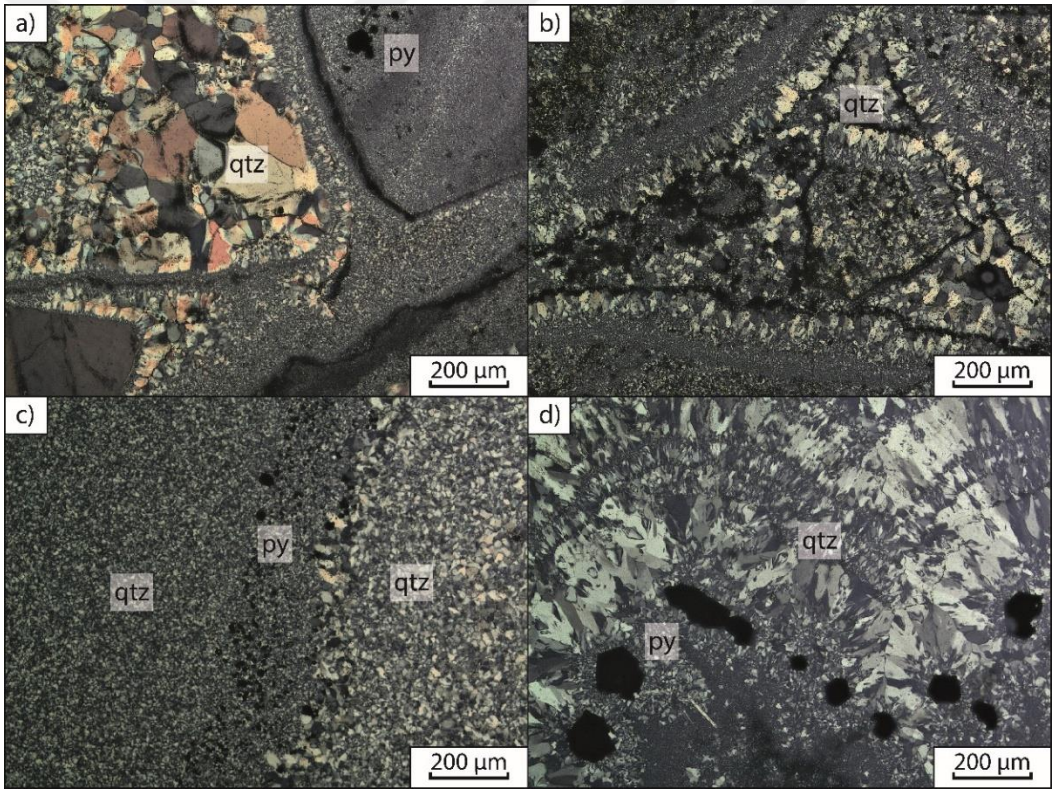


Figure 4.5. Microphotographs of vein textures a) hydrothermal breccia in quartz vein (Sample GCK-55, XPL), b) colloform banding surrounding silicified hydrothermal breccia (Sample GCK-49, XPL), c) siliceous vein showing paragenesis of earlier medium-grained massive quartz and pyrite bearing later fine-grained quartz (Sample GCK-32A, XPL), and d) pyrite within finer quartz changing into coarser barren quartz zone (Sample GCK-30, XPL).

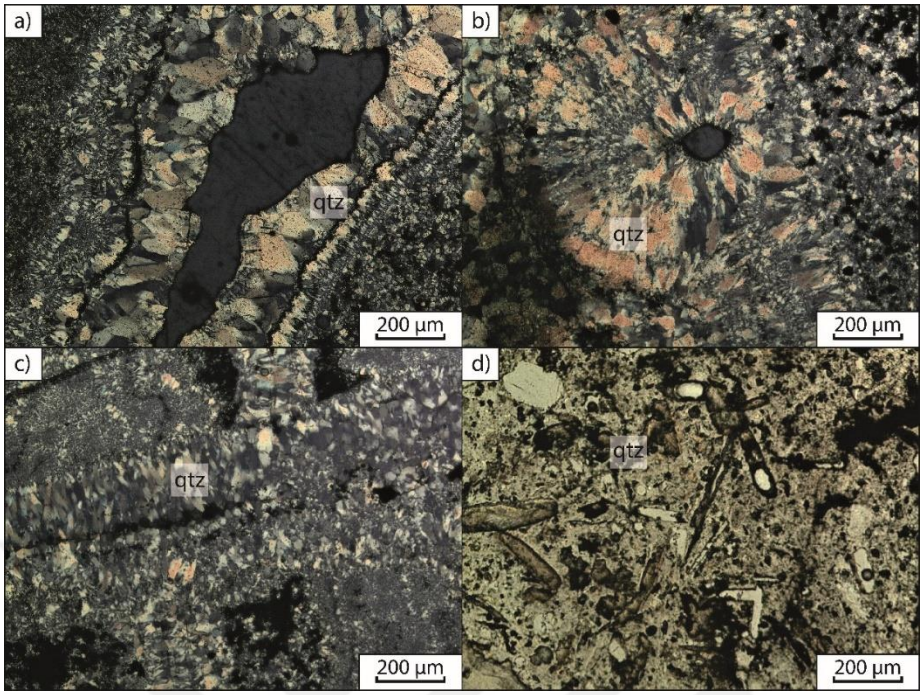


Figure 4.6. Microphotographs of vein textures a) silicified vein with comb texture (Sample GCK-49, x4, XPL), b) quartz forming cockade texture (GCK-48, XPL), c) quartz veins cutting each other (Sample GCK-51, XPL) and d) quartz vein displaying lattice bladed texture (Sample GCK-66, PPL).



Figure 4.7. Hand specimen of Fe-(hydr)oxide-coated siliceous rock from Q1 Vein (UTM Coordinates 497249 E, 4429198 N).

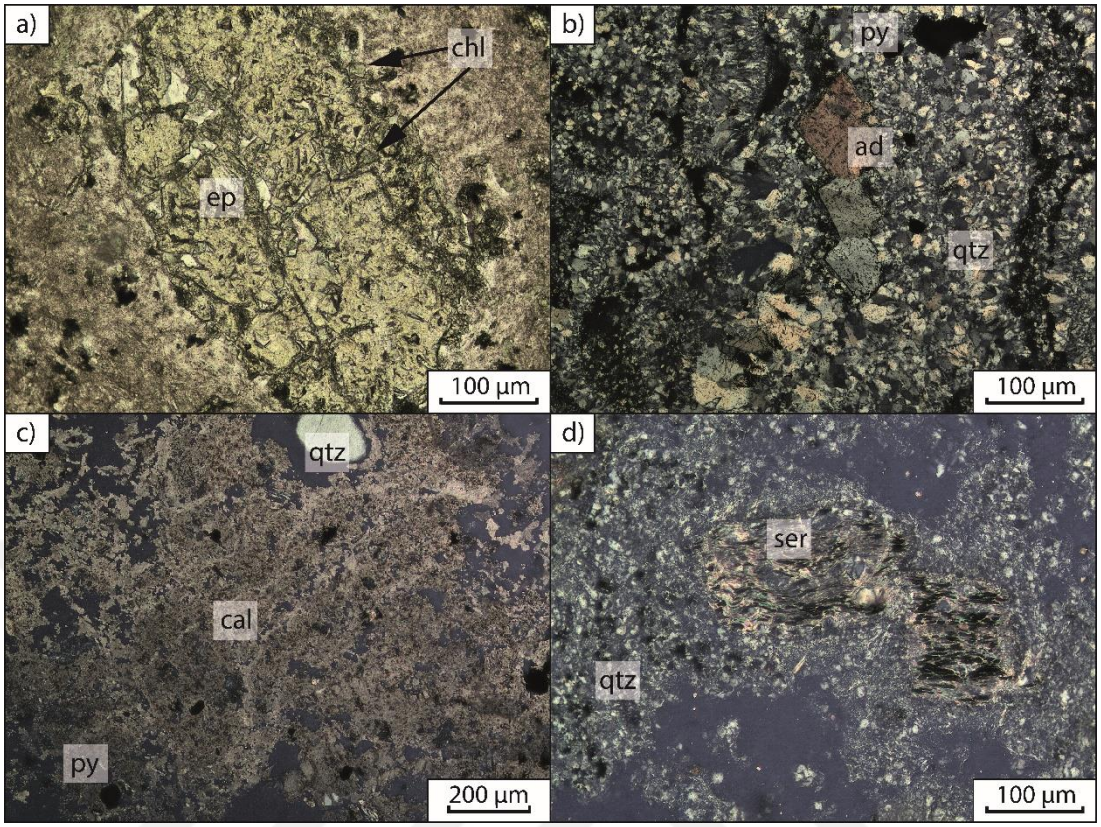


Figure 4.8. Microphotographs of alteration minerals a) epidote and chlorite crystals formed after plagioclase mineral. Epidote has its characteristic pale-yellow color; on the other hand, chlorite has distinctive pale green color (Sample GCK-10, PPL), b) euhedral adularia formed in the colloform bands (Sample GCK-64-1, XPL), c) calcite formed as a result of epidote–chlorite (propylitic) alteration (Sample GCK-6, XPL) and d) sericite formed after plagioclase feldspar (Sample GCK-15, XPL).

4.1.2.1. Timing of Hydrothermal Alteration

$^{40}Ar/^{39}Ar$ geochronological data was obtained from two hydrothermally-altered rock samples from Gicik (unpublished data of I. Kuscu) in order to understand the temporal relationship between magmatism and hydrothermal alteration. Both dated samples were collected from argillic-altered volcanic rocks; sample 542636 from a hydrothermal breccia outcrop from the western margin of the study area (Figure 2.1), whereas sample 661564 was collected from the northern part of the Q1 vein as exposed in the Gicik town center (Figure 2.18). $^{40}Ar/^{39}Ar$ geochronological analyses

were carried at the Pacific Centre for Isotopic and Geochemical Research at the University of British Columbia (B.C., Canada). A summary of the $^{40}Ar/^{39}Ar$ geochronological analyses is given in Table 4.3 and illustrated in Figure 4.9, and full data are given in Appendix L. Age errors are reported at the ± 2σ level.

Table 4.3. $^{40}Ar/^{39}Ar$ age of the sericite minerals from Gicik altered rocks (personal communication with İlkay Kuşcu, unpublished data).

Sample	Mineral	Easting	Northing	Rock Type	Plateau Age (Ma)	Normal Isochron Age (Ma)	Inverse Isochron Age (Ma)
542639	Sericite	494683	4428863	Altered hydrothermal breccia	45.31±0.38	44.42±0.58	44.66±0.55
661564	Sericite	496925	4428816	Altered argillitized dacite	46.95±0.73	48.0±3.6	-

The hydrothermal breccia sample (542639) yielded an undisturbed plateau age of 45.31±0.38 Ma (MSWD = 2.1) in five consecutive steps containing 64% of the released ^{36}Ar (Figure 4.9). Although inverse isochron (44.66±0.55 Ma; Figure 4.9) and total gas ages (44.44±1.30 Ma) overlap with the plateau age, the latter is preferred as a better estimate of the formation age of sericite.

Sericite in sample 661564 from near the Q1 vein yielded one low apparent age step followed by a four-step plateau containing 72.5% of the released ^{36}Ar (Figure 4.9) with an age of 46.95±0.73 Ma (MSWD = 2.9). These were again followed by low apparent age steps suggesting diffusive ^{40}Ar loss as a result of partial resetting (Figure 4.9). The sample did not yield a valid inverse isochron age, and the total gas age of 44.14±0.53 Ma is considered as a better estimate of the true age of this sample.

$^{40}Ar/^{39}Ar$ ages obtained from both samples are statistically indistinguishable from each other and they also overlap with the previously published K-Ar ages (44.7±1.0 Ma and 44.7±1.0) from the Gicik volcanic rocks by Seyitoğlu and Büyükonal (1995).

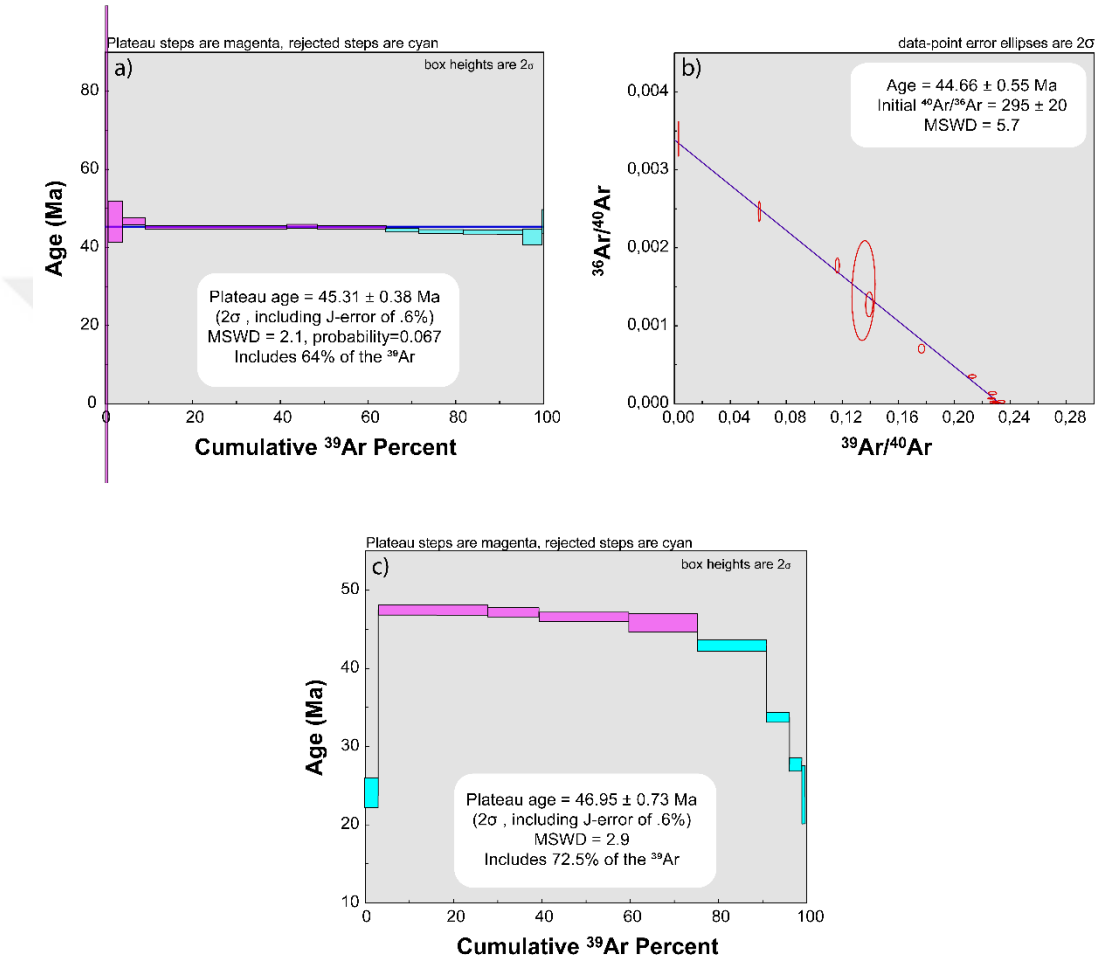


Figure 4.9. $^{40}Ar/^{39}Ar$ spectra and inverse isochron plots of sericite from hydrothermally-altered samples 542639 (a and b) and 661564 (c). Sample locations and analytical are given in the text. (Data is from Kuşcu, unpublished).

CHAPTER 5

DISCUSSIONS

5.1. Nature and Tectonic Setting of Gicik Volcanism

The Gicik vein-hosted gold deposit is one of only few epithermal gold systems that have been reported from central Anatolia, and is currently the only epithermal gold deposit known in the north central Anatolia. The deposit area is dominated by an intermediate composition volcanic sequence consisting mainly of andesitic to dacitic lava flows and agglomerates. K-Ar dating of these volcanic units constrained the timing of eruption at Gicik to middle Eocene (ca. 44 Ma). Similar to slightly younger K-Ar ages obtained from andesitic–dacitic volcanic rocks from Hüseyingazi Hill (44 to 41 Ma; Seyitoğlu and Büyükönal, 1995; Dönmez et al., 2009) as well as from various volcanic exposures near Bağlum, Elmadağ, and Çubuk areas indicated a major volcanic event during middle to late Eocene (Ach, 1982; Seyitoğlu and Büyükönal, 1995; Dönmez et al., 2009). The middle Eocene age of volcanism contradicts with some of the earlier studies (e.g., Akyürek et al., 1984) that suggested a Miocene age for calc-alkaline magmatism (i.e., Tekke Volcanics) in northern Ankara.

The least-altered and altered andesite to dacites from Gicik are metaluminous, medium-K calc-alkaline volcanic rocks (Figures 3.1, 3.2 and 3.3). Their geochemical affinities suggest derivation from a relatively HFSE-depleted, and LILE- and LREE-enriched melt source (Figures 3.5 and 3.6), which are typical of arc settings.

Although earlier studies (Koçyiğit, 1991; Koçyiğit et al., 2003) envisaged a subduction setting for middle Eocene volcanism developed in north Ankara including the older Eocene volcanic cycle in the Galatean Volcanic Province, paleotectonic reconstructions and regional tectonic models challenge this hypothesis.

The Izmir-Ankara-Erzincan Ocean was already closing in the Late Cretaceous by northward subduction beneath the Pontides, during which time an Upper Cretaceous accretionary prism developed in between the Sakarya Zone and the Kırşehir Block (Koçyiğit, 1991; Rojay et al., 2001). The leading edge of the Kırşehir Block initially collided ("soft" collision) with the south-facing margin of the Sakarya Zone at the end of the Cretaceous or earliest Paleocene causing early oroclinal bending (Kaymakçı et al., 2000 and 2009) and internal deformation in the northern part of the Kırşehir Block (Görür et al., 1998; Görür and Tüysüz, 2001). Small exposures of Campanian–Maastrichtian calc-alkaline volcanic rocks identified in the northern part of Ankara represent products of subduction-related magmatism during this interval (Koçyiğit, 1991; Keller et al., 1992). The collisional event progressed in the Paleocene, and the remaining parts of the Izmir-Ankara-Erzincan seaway was completely terminated by "hard" collision by the early Eocene (Görür et al., 1998; Nairn et al., 2012). The middle Eocene volcanic event in the north of Ankara post-dates the collision between the Sakarya Zone and the Kırşehir Block, and therefore suggested to have developed in a post-collisional setting.

Geochemically, the middle Eocene volcanic units erupted in Gicik are difficult to distinguish from normal arc magmas, which typically form by partial melting of the asthenospheric mantle wedge. Dehydration of the downgoing slab promotes the partial melting of this portion of the mantle through transport of slab-derived volatile components and fluids (Gill, 1981). Once subduction ceases melt production in the mantle wedge usually terminates (Gill and Whelan, 1989; Cloos et al., 2005). However, major tectonic readjustments during or after collision (e.g., delamination, post-collisional extension, etc.) may trigger re-melting of the previously subduction-modified regions of the mantle or lower crust (Harris, et al., 1986; Cloos et al., 2005; Richards, 2009). Magmas generated under such circumstances may have broadly similar geochemical characteristics to normal arc magmas, or they may be relatively alkaline rather than calc-alkaline (Harris et al., 1986; Davies and von Blankenburg, 1995; Richards, 2009).

A major belt of middle Eocene calc-alkaline magmatic rocks exists along and to the north of the Izmir-Ankara-Erzincan Suture Zone. The development of this belt is widely attributed to roll-back and break-off of the northward-subducting Izmir-Ankara-Erzincan Ocean leading to upwelling of hot asthenosphere and eventual partial melting of the mantle wedge or mafic lower crust (Altunkaynak and Genç, 2008; Boztuğ and Harlavan, 2008; Keskin et al., 2008; Karslı et al., 2011; Dokuz et al., 2013). Therefore, the middle Eocene Gicik volcanic sequence and coeval volcanism throughout north of Ankara likely developed in response to this slab break-off event.

Following the Eocene eruptive event, magmatism to the north of Ankara resumed with eruption of volcanic rocks between 25 and 10 Ma with a wide compositional range from trachybasalts and trachyandesites to rhyolites (Wilson et al., 1997; Tankut et al., 1998a, b; Adıyaman et al., 2001; Varol et al., 2007, 2008, 2014). A comparison between intermediate composition Gicik and Galatean volcanic rocks indicated that the latter are relatively more alkaline and have high–K calc–alkaline to shoshonitic affinities (Wilson et al., 1997; Tankut et al., 1998; Figures 3.2 and 3.3). Although normalized multi-element variation and REE diagrams indicate that these two distinct magmatic suites display subduction signatures (Figures 3.5 and 3.6), the relatively more alkaline character of the Galatean volcanic rocks may indicate formation at relatively advanced stages of collision in north Ankara. A similar distinction is evident on the Ti versus Zr diagram (Figure 3.7), which clearly demonstrates the within-plate character of the intermediate composition Galatean volcanic rocks.

Overall, the Gicik volcanic sequence hosting vein-type gold mineralization shows arc-like geochemical signatures in that they are medium-K calc-alkaline igneous rocks that are characterized by relative enrichments in LILE and LREE, and depletions in HFSE such as Nb and Ta. The presence of magnetite microphenocrysts and common presence of hornblende and biotite in host volcanic rocks suggest that source magmas are relatively oxidized and hydrous. Such magmas are considered as a prerequisite for formation of porphyry-type and associated high-sulfidation epithermal deposits

(Richards, 2005, 2009, 2011). However, such a relationship is not clear established for low-sulfidation epithermal systems, which usually post-date volcanic activity. Still, studies on some low-sulfidation system have clearly demonstrated significant fluid and/or metal contributions to low-sulfidation epithermal mineralization (Alderton and Fallick, 2000; John, 2001; Faure et al., 2002; Richards et al., 2006). A compilation of whole-rock geochemical data from globally-significant epithermal districts also confirmed that epithermal deposits, regardless of the sub-type, are genetically associated with relatively oxidized and water-rich magmas (du Bray, 2017). Thus, the geochemical features of the middle Eocene volcanic host rocks may have an important role in the formation of the Gicik low-sulfidation system, which is also supported by the overlap between ages (ca. 44 Ma) obtained from igneous host rocks and hydrothermal alteration minerals. However, stable isotope and fluid inclusion studies are required to confirm such a genetic relationship

5.2. Formation of Gicik Low-Sulfidation Epithermal System

Gicik epithermal system comprises several NE–SW-trending silicified veins; T, Q, G, East and Creek Veins. These veins are situated along NE–SW-trending oblique faults with dominant strike-slip components, which acted as permeable pathways for convection of hydrothermal solutions. Paleostress analyses of fault surface measurements has shown that these NE–SW-trending structures were formed under transpressional stress conditions. Although most epithermal, and particularly low-sulfidation, systems develop within pure extensional or transtensional tectonic settings (Cooke and Simmons, 2000; Sillitoe and Hedenquist, 2003), there are several examples that were formed under transpressional rather than extensional or transtensional stress conditions, such as McLaughlin in western U.S. (Sherlock et al., 1995) and low-sulfidation epithermal systems of the Rosario-Bunawan district in Philippines (Kolb and Hagemann, 2009)

Textures that are characteristic of low-sulfidation systems such as colloform banding, crustification, bladed/lattice bladed textures, and cockade textures are common in

almost all vein systems with the exception of the T vein, which is only poorly exposed, and is characterized by massive silicification and a texture-poor porphyritic wall-rock situated at the northeast of Gicik village. The T vein is exposed at an altitude of ~1180 meters a.s.l., whereas other relatively better exposed veins outcrop between altitudes of 1060–1170 meters a.s.l., suggesting that the T vein may be a relatively higher level manifestation of the Gicik epithermal system. Based on the elevation, mineralogical and textural data, identified veins strongly display sub-vertical zones in low-sulfidation epithermal systems; the T vein corresponds to relatively shallow sections, whereas the Q and G veins correspond to relatively deeper sections sections.

Main textures are identified as; hydrothermal breccia, colloform banding, cockade, lattice bladed, stockwork, thin quartz veinlets (resembling stockwork), chalcedonic, amethyst quartz, crustiform, comb, drusy and massive quartz veins. Relationship of textures between each other is not clear; however, local interpretations can be made. In many samples, hydrothermal brecciation has been cross-cut by colloform bands. Two types of colloform bands are identified, barren and sulfide-bearing (mainly pyrite- and arsenopyrite-bearing) varieties. Fine-grained chalcedonic quartz was followed in the paragenesis by sulfide-bearing colloform bands, which in turn was overprinted by coarse-grained quartz bands. In some samples, pyrite with fine-grained quartz form the center of the cockade texture, surrounded by coarse-grained barren quartz bands. Massive coarse-grained quartz and open-space filling textures such as crustiform, drusy and amethystic quartz are interpreted to represent the latest stage in the paragenesis.

Ore mineralogy of the Gicik vein system is dominated mainly by pyrite and arsenopyrite, which have been observed almost in all veins as within colloform bands or in intensely silicified volcanic wall-rocks as dissemination. Argentiferous tetrahedrite is another ore mineral observed particularly in higher and middle sections of the G Veins, as both fine-grained disseminations and relatively coarse-grained euhedral rhombohedral crystals within colloform bands. The pyrite-arsenopyrite assemblage is stable under relatively low f_{S2} conditions (Einaudi et al., 2003; Sillitoe

and Hedenquist, 2003; Simmons et al., 2005). In addition, Ag and Se signatures rather than Cu and Te in the mineralized rocks is also indicative of a low-sulfidation epithermal system.

Hydrothermal alteration is widespread throughout the study area and shows a broad zonation pattern laterally around the mineralized siliceous veins. Regional propylitic alteration, characterized by epidote-chlorite-carbonate assemblages, developed distally with alteration intensity increasing towards siliceous veins. This was followed inward by an argillic alteration zone of kaolinite-sericite/illite-smectite-quartz±adularia, whereas the core of the mineralized system is characterized by intense silicification.

The co-existence of illite and kaolinite in altered volcanic wall-rocks suggests fluid pH levels of 4–5, and the predominance of illite with minor smectite (rather than muscovite) in argillic alteration zones combined with ore mineralogy suggests and formation temperatures between 150° and 250°C at depths below 300 m (Reyes, 1990; Hedenquist et al., 2000). A fluid inclusion investigation was attempted in order to accurately constrain the formation temperatures, depths, and fluid compositions, but none of the studied samples yielded fluid inclusions suitable for fluid inclusion microthermometry. In fact, inclusion-free recrystallized quartz was observed in most of the studied samples. Nevertheless, the estimated temperature conditions are in line with the homogenization temperature data (140° to 240°C) obtained by Besbelli and Varol (2002).

5.3. Potential Implications for Regional Metallogeny

The Gicik gold deposit was developed in a post-collisional setting following closure of the Izmir-Ankara-Erzincan Ocean. The temporal link established between middle Eocene magmatism and epithermal gold mineralization may have some implications for metallogeny of the northern part of Anatolia, where widespread Eocene magmatism can be observed.

As mentioned earlier, the Gicik volcanic sequence carries arc-like geochemical signatures, yet these volcanic rocks were erupted in a post-collisional tectonic setting, and most likely in response to the break-off of the downgoing slab of the Izmir-Ankara-Erzincan Ocean.

Although no other major precious and/or base metal deposits are known from northern part of Ankara, the continuation of the post-collisional middle Eocene magmatic belt towards the west and eastern parts of Turkey hosts several important mineral systems. In central northwest Anatolia near Kaymaz, middle Eocene magmatic rocks emplaced into a sequence of meta-siliciclastic and ophiolitic units resulted in formation of the Kaymaz orogenic gold system (Demirbilek et al., 2018). Farther in the northwest, in the Biga Peninsula, majority of the base and precious metal deposits are associated with late Eocene and Oligocene plutonic and volcanic rocks, but there are several epithermal systems, such as the Kartaldağ high-sulfidation, and Madendağ and Kestanelik/Lapseki low-sulfidation deposits as well as, which again developed in relation to middle Eocene calc-alkaline magmatism (Ünal-İmer et al., 2013; Gülyüz et al., 2018).

The Mastra intermediate-sulfidation in Gümüşhane (Tüysüz et al., 1995) and the Taç and Çorak low-sulfidation deposits near Yusufeli (Artvin) are important examples from the Eastern Pontide Magmatic Belt, which are also hosted in calc-alkaline volcanic rocks of middle Eocene age.

Because post-collisional magmatism may remobilize gold in refractory sulfide phases in the mafic lower crustal rocks (Richards, 2009), the entire middle Eocene magmatic belt to the north of the Izmir-Ankara-Erzincan Suture Zone has the potential to host particularly precious metal-rich mineralization (rather than base metal-rich).

CHAPTER 6

CONCLUSIONS

Volcanism around Ankara and related Gicik Au mineralization was evaluated using geological mapping and sampling, alteration and ore mineral identification, detailed petrography, $^{40}Ar/^{39}Ar$ geochronology, whole-rock and mineral geochemistry. The conclusions of this study are summarized as followed:

- Volcanic rocks which host the Gicik Au deposits comprise are metaluminous, medium-K calc-alkaline intermediate (dacitic) composition with arc-like geochemical signatures. These volcanic rocks are suggested to be derived from melt source with geochemical affinities of depleted HFSE, and enriched LILE and LREE.
- Development of Eocene magmatic belt in Anatolia is widely attributed to slab break-off of the northward-subducting İzmir-Ankara-Erzincan Ocean. Volcanism at the north of Ankara and the Gicik area are considered to be formed in response to such event.
- Calc-alkaline Eocene volcanism around Ankara was followed by relatively more alkaline Miocene eruptive events of Galatean volcanic rocks in central Anatolia which suggests formation at relatively advanced stages of collision in north Ankara although the similar presence of subduction signatures in each volcanic sequence.
- The idea of magmatic contribution to the hydrothermal fluids which are responsible for the formation of Gicik mineralized system are supported by the overlapping volcanism and hydrothermal alteration ages, however, stable isotope and fluid inclusion studies should be performed to understand this genetic relationship.

- Gold at Gicik is host in multiple NE-SW oriented silicified veins which are developed in response to the NE-SW trending strike-slip dominated oblique faults under transpressional stress conditions.
- Typical low-sulfidation epithermal system textures, including cockade, colloform banding, hydrothermal breccia, bladed/lattice bladed and crustification, are widely observed within the silicified vein systems in Gicik.
- In terms of ore mineralogy, pyrite and arsenopyrite are the dominant minerals. Pyrite and arsenopyrite are observed within colloform bands and as disseminations in silicified volcanic rocks. In addition to these, argentiferous tetrahedrite is locally observed within colloform bands at relatively higher and middle sections of G Veins.
- Alteration mineralogy is well displayed in Gicik as widely distributed propylitic alteration characterized by epidote-chlorite-carbonate assemblages, and argillic alteration zone with kaolinite-sericite/illite-smectite-quartz±adularia. Argillic alteration intensifies through the silicified veins.
- Eastern and western continuation of Eocene magmatic belt in Anatolia host numerous mineralized systems, whereas the central parts are remained relatively underexplored. Proving the existence of Eocene magmatic-hydrothermal system in central Anatolain segment puts entire Eocene magmatic belt to susceptive position to host particularly precious metal-rich mineralization.

REFERENCES

Ach, J. A. (1982). The petrochemistry of the Ankara volcanics, central Turkey. Department of Geological Sciences, MSc, 145.

Ach, J. A., Wilson, F. U. (1986). Potassium-Argon ages of volcanic rocks from near Ankara, Central Turkey. Isocron/West 47, 15-17.

Adiyaman, Ö., Chorowicz, J., Arnaud, O. N., Gündogdu, M. N., and Gourgaud, A. (2001). Late Cenozoic tectonics and volcanism along the North Anatolian Fault: New structural and geochemical data. Tectonophysics, 338(2), 135–165. https://doi.org/10.1016/S0040-1951(01)00131-7

Akyürek, B., Akbaş, B., and Dağer, Z. (1988). Çankırı-E16 paftası 1:100.000 ölçekli açınsama nitelikli Türkiye Jeoloji Haritaları Serisi.

Akyürek, B., Bilginer, E., Akbaş, B., Hepşen, N., Pehlivan, Ş., Sunu, O., Soysal, Y., Dağer, Z., Çatal, E., Sözeri, B. Yıldırım, H. and Hakyemez, Y. (1982). Ankara-Elmadağ-Kalecik dolayının jeolojisi. Ankara.

Alderton, D. H., & Fallick, A. E. (2000). The nature and genesis of gold-silver-tellurium mineralization in the Metaliferi Mountains of western Romania. Economic Geology, 95(3), 495-516.

Altunkaynak, Ş., & Genç, Ş. C. (2008). Petrogenesis and time-progressive evolution of the Cenozoic continental volcanism in the Biga Peninsula, NW Anatolia (Turkey). Lithos, 102(1-2), 316-340.

Asan, K., and Kurt, H. (2011). Petrology and geochemistry of post-collisional Early Miocene volcanism in the Karacadağ Area (Central Anatolia, Turkey). Acta Geologica Sinica, 85(5), 1100–1117.

Asan, K. Mineral chemistry and geothermobarometry of alkali basalts from the Elmadağ Volcanic Complex, Ankara (Central Anatolia, Turkey). Mechanics, Energy, Environment, 177–181.

Ashley, R. P. (1982). Occurence model for enargite-gold deposits: U.S. Geological Survey Open-File Report, 82(795), 144–147.

Baker, T. (2019). Gold ± copper endowment and deposit diversity in the West Tethyan magmatic belt, southeast Europe: Implications for exploration. Econ. Geol.

Bas, M. J. L., Maitre, R. W. L., Streckeisen, A., and Zanettin, B. (1986). A chemical classification of volcanic rocks based on the total alkali-silica diagram. Journal of Petrology, 27(3), 745–750.

Berger, B. R., and Henley, R. W. (1989). Advances in understanding of epithermal gold-silver deposits, with special reference to the western United States. Economic Geology Monograph, 6, 405–423.

Berk Biryol, C., Beck, S. L., Zandt, G., and Özacar, A. A. (2011). Segmented African lithosphere beneath the Anatolian region inferred from teleseismic P-wave tomography. Geophysical Journal International, 184(3), 1037–1057.

Besbelli, A., and Varol, B. (2002). Tekke volkanitlerinde hidrotermal alterasyon ürünü kil mineralleşmeleri (Çubuk, Ankara KD). MTA, 125(1902), 121–137.

Bonham, H. F. J. (n.d.). Models for volcanic-hosted epithermal precious metal deposits: A review. International Volcanological Congress, Symposium 5, 13–17. Hamilton, New Zealand.

Bonham, H. F. J. (1988). Models for volcanic-hosted precious metal deposits: A review. In R. W. Schafer, J. J. Cooper, and P. G. Vikre (Eds.), Geological Society of Nevada (Bulk mine).

Bozkurt, E., and Mittwede, S. K. (2001). Introduction to the geology of Turkey - A synthesis. International Geology Review, 43(7), 578–594.

Boztuğ, D., & Harlavan, Y. (2008). K–Ar ages of granitoids unravel the stages of Neo-Tethyan convergence in the eastern Pontides and central Anatolia, Turkey. International Journal of Earth Sciences, 97(3), 585-599.

Brown, T. J., Idoine, N.E., Raycradt, E. R., Hobbs, S. F., Shaw, R. A., Everett, P., Kresse, C., Deady, E. A., Bide, T. (2019). World mineral production 2013-17. British Geological Survey. Keyworth, Nottingam, 91 p.

Buchanan, L. J. (1981). Precious metal deposits associated with volcanic environments in the Southwest. Arizona Geological Society Digest, 14, 237–262.

Büyükönal, G. (1971). Microscopical study of the volcanic rocks around Ankara. Communications de La Faculté Des Sciences de l'Université d'Ankara, 15c.

Chambefort, I., Dilles, J. H., and Longo, A. A. (2013). Amphibole geochemistry of the yanacocha volcanics, peru: Evidence for diverse sources of magmati Cvolatiles related to gold ores. Journal of Petrology, 54(5), 1017–1046.

Cooke, D. R., and Simmons, S. F. (2000). Characteristics and genesis of epithermal gold deposits. Society of Economic Geologists Reviews, 13, 221–244.

Corbett, G. (2002). Epithermal gold for explorationists. AIG Journal, Applied Geoscientific Practice and Research in Australia, (February), 26 p.

Cox, K. G., Bell, J. D., and Pankhurst, R. J. (1979). The interpretation of igneous rocks (Allen and Un). London.

Çalgın, R., Ercan, T., Pehlivanoğlu, H., and Şengün, M. (1973). Ankara çevresi jeolojisi. Ankara.

Demirbilek, M., Mutlu, H., Fallick, A. E., Sarıiz, K., and Kibici, Yaşar. (2018). Petrogenetic evolution of the Eocene granitoids in eastern part of the Tavşanlı Zone in northwestern Anatolia, Turkey. Lithos, 314-315, 236-259.

Dhont, D., Chorowicz, J., Yürür, T., Froger, J. L., Köse, O., and Gündogdu, N. (1998). Emplacement of volcanic vents and geodynamics of Central Anatolia, Turkey. Journal of Volcanology and Geothermal Research, 85(1–4), 33–54.

Dirik, K., and Göncüoglu, M. C. (1996). Neotectonic characteristics of central anatolia. International Geology Review, 38(9), 807–817.

Dogan-Kulahci, G. D., Temel, A., Gourgaud, A., Varol, E., Guillou, H., and Deniel, C. (2018). Contemporaneous alkaline and calc-alkaline series in Central Anatolia (Turkey): Spatio-temporal evolution of a post-collisional Quaternary basaltic volcanism. Journal of Volcanology and Geothermal Research, 356, 56–74.

Dokuz, A., Uysal, I., Siebel, W., Turan, M., Duncan, R., & Akçay, M. (2013). Post-collisional adakitic volcanism in the eastern part of the Sakarya Zone, Turkey: evidence for slab and crustal melting. Contributions to Mineralogy and Petrology, 166(5), 1443-1468.

du Bray, E. A. (2017). Geochemical characteristics of igneous rocks associated with epithermal mineral deposits—a review. Ore Geology Reviews, 80, 767-783.

Dumanlılar H, Aydal D, and Dumanlılar Ö. (1999) Geology, mineralogy and geochemistry of sulfide mineralization in the Ispendere region (Malatya). Bull Min Res Explor Inst Turkey (MTA) 121:57–82.

Faure, K., Matsuhisa, Y., Metsugi, H., Mizota, C., & Hayashi, S. (2002). The Hishikari Au-Ag epithermal deposit, Japan: oxygen and hydrogen isotope evidence in determining the source of paleohydrothermal fluids. Economic Geology, 97(3), 481-498.

Fournier, J. M. (1985). Magnetic properties of actinide solids. In Actinides—Chemistry and Physical Properties (pp. 127-196). Springer, Berlin, Heidelberg.

Gençoğlu Korkmaz, G., Asan, K., Kurt, H., and Morgan, G. (2017). 40Ar/39Ar geochronology, elemental and Sr-Nd-Pb isotope geochemistry of the Neogene bimodal volcanism in the Yükselen area, NW Konya (Central Anatolia, Turkey). Journal of African Earth Sciences, 129, 427–444.

Giggenbach, W.F., 1992, Magma degassing and mineral deposition in hydrothermal systems along convergent plate boundaries: Economic Geology, v. 87, p. 1927-1944.

Giles, D. L., and Nelson, C. E. (1982). Principal features of epithermal lode gold deposits of the circum-Pacific rim. Circum-Pasific Energy and Mineral Resources Conference, 3rd, 273–278. Honolulu: American Association of Petroleum Geologists.

Goldfarb, R., Baker, T., Dubé, B., Groves, D. I., Hart, C. J. R., and Gosselin, P. (2005). Distribution, character, and genesis of gold deposits in metamorphic terranes. Economic Geology, 100th Anni, 407–450.

Gökten, E., Özaksoy, V., and Karakus, K. (1996). Tertiary volcanic and tectonic evolution of the ayas-güdül-celtikci region, turkey. International Geology Review, 38(10), 926–934.

Göncüoğlu, M. C., Toprak, V., Kuşcu, İ., Erler, A., and Olgun, E. (1991). Geology of the western part of the Central Anatolian Massif. In Turkish Petroleum Corporation Report.

Gorur, N., & Tuysuz, O. (2001). Cretaceous to Miocene palaeogeographic evolution of Turkey: implications for hydrocarbon potential. Journal of Petroleum Geology, 24(2), 119-146.

Görür, N., Tüysüz, O., & Celal Şengör, A. M. (1998). Tectonic evolution of the central Anatolian basins. International Geology Review, 40(9), 831-850.

Gribble, C. D., and Hall, A. J. (1992). Optical mineralogy: Principles and practice. CRC Press.

Groves, D. I., Goldfarb, R. J., Gebre-Mariam, M., Hagemann, S. G., and Robert, F. (1998). Orogenic gold deposits: A proposed classification in the context of their crustal distribution and relationship to other gold deposit types. Ore Geology Reviews, 13, 7–27.

Groves, D. I., and Bierlein, F. P. (2007). Geodynamic settings of mineral deposit systems. Journal of the Geological Society, 164(1), 19–30.

Harker, A. (1909). The natural history of igneous rocks. Methuen, London.

Harris, N. B., Pearce, J. A., and Tindle, A. G., 1986, Geochemical characteristics of collision-zone magmatism. Geological Society, London, Special Publications, 19(1), 67-81.

Hayba, D. O., Bethke, P. M., Heald, P., and Foley, N. K. (1985). Geologic, mineralogic, and geochemical characteristics of volcanic-hosted epithermal precious metal deposits. Reviews in Economic Geology, 2, 129–167.

Heald, P., Foley, N. K., and Hayba, D. O. (1987). Comparative anatomy of volcanic-hosted epithermal deposits: Acid sulfate and adularia-sericite types. Economic Geology, 82, 1–26.

Hedenquist, J. W. (1987). Volcanic-related hydrothermal systems in the Circum-Pasific Basin and their potential for mineralization. Mining Geology, 37(205), 347–364.

Hedenquist, J.W. and Lowenstern, J.B., 1994, The role of magmas in the formation of hydrothermal ore deposits: Nature, v. 370, 519-527.

Hedenquist, J. W., Arribas, A., and Gonzalez-Urien, E. (2000). Exploration for epithermal gold deposits. Reviews in Economic Geology, 13(1), 245–277.

Hedenquist, J. W., and Inan, E. E. (2003). Porphyry to Epithermal Environments. Society, (February), 1–50.

Henley, R.W., Truesdell, A.H. and Barton, P.B., 1984, Fluid-mineral equilibria in hydrothermal systems. Society of Economic Geologists, Reviews in Economic Geology, v. 1, 267 p.

İmer, A., Richards, J. P., and Creaser, R. A. (2013). Age and tectonomagmatic setting of the Eocene Çöpler-Kabataş magmatic complex and porphyry-epithermal Au deposit, East Central Anatolia, Turkey. Mineralium Deposita, 48(5), 557–583.

İmer, A., Richards, J. P., Creaser, R. A., and Spell, T. L. (2015). The late Oligocene Cevizlidere Cu-Au-Mo deposit, Tunceli Province, eastern Turkey. Mineralium Deposita, 50(2), 245–263.

İmer, A., Richards, J. P., and Muehlenbachs, K. (2016). Hydrothermal evolution of the Çöpler porphyry-epithermal Au deposit, Erzincan Province, Central Eastern Turkey. Economic Geology, 111(7), 1619–1658.

Innocenti, F., Mazzuoli, R., Pasquarè, G., Radicati di Brozolo, F., and Villari, L. (1975). The Neogene calcalkaline volcanism of Central Anatolia: Geochronological data on Kayseri—Nigde area. Geological Magazine, 112(4), 349–360.

Irvine, T. N., and Baragar, W. R. A. (2011). A Guide to the Chemical Classification of the Common Volcanic Rocks. Canadian Journal of Earth Sciences, 8(5), 523–548.

John, A. D., Hofstra, A. H., Fleck, R. J., Brummer, J. E., and Saderholm, E. C. (2003). Geologic setting and genesis of the Mule Canyon low-sulfidation epithermal gold-silver deposit, North-Central Nevada. Economic Geology, 98, 425-463.

John, A. D. (2001). Miocene and early Pliocene epithermal gold-silver deposits in the northern Great Basin, western United States: Characteristics, distribution, and relationship to magmatism. Economic Geology, 96 (8), 1827-1853.

John, D. A., and Wallace, A. R. (2000). Epithermal gold-silver deposits related to the northern Nevada rift. Geology and ore deposits, 155-175.

Kaptan, E. (1990). Findings related to the history of mining in Turkey. Mineral Research and Exploration Bulletin v. 111, 75-84.

Karadenizli, L. (2011). Oligocene to Pliocene palaeogeographic evolution of the Çankiri-Çorum Basin, central Anatolia, Turkey. Sedimentary Geology, 237(1–2), 1–29.

Karsli, O., Ketenci, M., Uysal, İ., Dokuz, A., Aydin, F., Chen, B., ... & Wijbrans, J. (2011). Adakite-like granitoid porphyries in the Eastern Pontides, NE Turkey: potential parental melts and geodynamic implications. Lithos, 127(1-2), 354-372.

Karslı, O., Dokuz, A., Uysal, İ., Aydın, F., Kandemir, R., and Wijbrans, J. (2010). Generation of the Early Cenozoic adakitic volcanism by partial melting of mafic lower crust, Eastern Turkey: Implications for crustal thickening to delamination. Lithos, 114, 109-120.

Keller, J., Jung, D., Eckhardt, F. J., and Kreuzer, H. (1992). Radiometric ages and chemical characterization of the Galatean andesite massif, Pontus, Turkey. Acta Vulcanologica Marinelli, 2, 267–276.

Keskin, M. (2003). Magma generation by slab steepening and breakoff beneath a subduction-accretion complex: An alternative model for collision-related volcanism in Eastern Anatolia, Turkey.

Keskin M, Genç ŞC, Tüysüz O (2008) Petrology and geochemistry of post-collisional Middle Eocene volcanic units in North-Central Turkey: Evidence for magma generation by slab breakoff following the closure of the Northern Neotethys Ocean. Lithos 104:267–305.

Ketin, İ. (1966). Tectonic units of Anatolia. Maden Tetkik ve Arama Bulletin, 66, 23–34.

Koçyiğit, A., and Beyhan, A. (1999). Reply to Rob Westaway's Comment on 'A new intracontinental transcurrent structure: The Central Anatolian Fault Zone, Turkey.' Tectonophysics, 314(4), 481–496. https://doi.org/10.1016/s0040-1951(99)00227-9

Kolb, J., & Hagemann, S. (2009). Structural control of low-sulfidation epithermal gold mineralization in the Rosario–Bunawan district, East Mindanao Ridge, Philippines. Mineralium Deposita, 44(7), 795.

Kurt, H., Asan, K., and Ruffet, G. (2008). The relationship between collision-related calcalkaline, and within-plate alkaline volcanism in the Karacadağ Area (Konya-Türkiye, Central Anatolia). Chemie Der Erde, 68(2), 155–176.

Kuscu, G. G., and Geneli, F. (2010). Review of post-collisional volcanism in the Central Anatolian Volcanic Province (Turkey), with special reference to the Tepekoy Volcanic Complex. International Journal of Earth Sciences, 99(3), 593–621.

Kuscu, I., and Erler, A. (1998). Mineralization events in a collision-related setting: The central anatolian crystalline complex, Turkey. International Geology Review, 40(6), 552–565.

Kuşcu İ., Tosdal R.M., Gençalioğlu-Kuşcu G. (2019) Porphyry-Cu Deposits of Turkey. In: Pirajno F., Ünlü T., Dönmez C., Şahin M. (eds) Mineral Resources of Turkey. Modern Approaches in Solid Earth Sciences, vol 16. Springer, Cham

Kuşcu İ, Gençalioğlu-Kuşcu G, Tosdal RM, Ulrich TD, Friedman R (2010) Magmatism in the southeastern Anatolian orogenic belt: transition from arc to post-collisional setting in an evolving orogen. In: Sosson M, Kaymakçı N, Stephenson RA, Bergerat F, Starostenko V (eds) Sedimentary Basin Tectonics from the Black Sea and Caucasus to the Arabian Platform. Geol Soc Lond Spec Publ 340:437–460.

Kuşcu İ, Tosdal RM, Gençalioğlu-Kuşcu G, Friedman R, Ullrich TD (2013) Late Cretaceous to Middle Eocene Magmatism and Metallogeny of a Portion of the Southeastern Anatolian Orogenic Belt, East-Central Turkey. Econ Geol 108:641–666.

Kürkcüoglu, B. (2010). Geochemistry and petrogenesis of basaltic rocks from the Develidağ volcanic complex, Central Anatolia, Turkey. Journal of Asian Earth Sciences, 37(1), 42–51.

Maitre, L. (1989). A classification of igneous rocks and glossary of terms. Recommendations of the international union of geological sciences subcommission on the systematics of igneous rocks, 193.

Nairn, S. P., Robertson, A. H. F., Ünlügenç, U. C., Taşlı, K., and İnan, N. (2012). Tectonostratigraphic evolution of the Upper Cretaceous-Cenozoic central Anatolian basins: an integrated study of diachronous ocean basin closure and continental collision. Geological Society, London, Special Publications, 372, 343-384, 8 October 2012.

Lefebvre, C., Barnhoorn, A., van Hinsbergen, D. J. J., Kaymakci, N., and Vissers, R. L. M. (2011). Late Cretaceous extensional denudation along a marble detachment fault zone in the Kşrşehir massif near Kaman, central Turkey. Journal of Structural Geology, 33(8), 1220–1236.

Leonhard, R. (1902). Geologische Skizze des galatischen andesitgebietes nörlich von Angora. Schweizerbart.

Leonhard, R. (1915). Reisen und Forschungen im nördlichen Kleinasien.

Lindgren, W. (1933). Differentiation and ore deposition, Cordilleran region of the United States. Ore Deposits of the United States, Lindgren V, (170).

Lindgren, W. (1922). A suggestion for the terminology of certain mineral deposits. Economic Geology, 17, 292–294.

Middlemost, E. A. K. (1994). Naming materials in the magma/igneous rock system. Earth Science Reviews, 37(3–4), 215–224.

Moix, P., Beccaletto, L., Kozur, H. W., Hochard, C., Rosselet, F., and Stampfli, G. M. (2008). A new classification of the Turkish terranes and sutures and its implication for the paleotectonic history of the region. Tectonophysics, 451(1–4), 7–39.

Nekvasil, H., 1991. Ascent of felsic magmas and formation of rapakivi. Am. Mineral. 76, 1279–1290

Okay, A. I., and Tuysuz, O. (1999). Tethyan sutures of northern Turkey Major continental blocks of Turkey. The Mediterranean Basins: Tertiary Extension within the Alpine Orogen., 475–515.

Oyman, T. (2019). Epithermal deposits of Turkey. In Modern Approaches in Solid Earth Sciences (Vol. 16).

Özsayin, E., Çiner, T. A., Rojay, F. B., Dirik, R. K., Melnick, D., Fernández-Blanco, D., Bertotti, G., Schildgen, T. F., Garcin, T. F., Strecker, M. R., Sudo, M. (2013). Plio-Quaternary extensional tectonics of the Central Anatolian Plateau: A case study from the Tuz Gölü Basin, Turkey. Turkish Journal of Earth Sciences, 22(5), 691–714.

Öztürk, A., İnan, S., and Tutkun, Z. (1985). Abant-Yenicaga (Bolu) bölgesinin tektoniği. Mühendislik Fakültesi Dergisi, 2(1), 35–52.

Pasquarè, G., Poli, S., Vezzoli, L., and Zanchi, A. (1988). Continental arc volcanism and tectonic setting in Central Anatolia, Turkey. Tectonophysics, 146(1–4), 217–230.

Pearce, J. A. (1982). Trace element characteristics of lavas from destructive plate boundaries. Andesites 8, 525-548.

Pearce, J. A., Harris, N. B., and Tindle, A. G., 1984, Trace element discrimination diagrams for the tectonic interpretation of granitic rocks. Journal of petrology, 25(4), 956-983.

Pearce, J. A., Bender, J. F., De Long, S. E., Kidd, W. S. F., Low, P. J., Güner, Y., Saroğlu, Y., Moorbath, S., Mitchell, J. G. (1990). Genesis of collision volcanism in Eastern Anatolia, Turkey. Journal of Volcanology and Geothermal Research, 44(1–2), 189–229.

Peccerillo, A., and Taylor, S. R. (1976). Geochemistry of eocene calc-alkaline volcanic rocks from the Kastamonu area, Northern Turkey. Contributions to Mineralogy and Petrology, 58(1), 63–81.

Rabayrol, F., Hart, C. J. R., and Thorkelson, D. J. (2019). Temporal, spatial and geochemical evolution of the late Cenozoic post-subduction magmatism in central and eastern Anatolia, Turkey. Lithos, 336-337, 67-69.

Reyes, A.G., 1990, Petrology of Philippine geothermal systems and the application of alteration mineralogy to their assessment. Journal of Volcanology and Geothermal Research 43, 279-309.

Rojay, B., and Karaca, A. (2008). Post-Miocene deformation in the south of the Galatean Volcanic province, NW of Central Anatolia (Turkey). Turkish Journal of Earth Sciences, 17(4), 653–672.

Rojay, B., Yalınız, K., & Altıner, D. (2001). Age and origin of some pillow basalts from Ankara melange and their tectonic implications to the evolution of northern branch of Neotethys, Central Anatolia. Turkish Journal of Earth Sciences, 10(3), 93-102.

Richards, J. P. (2015). Tectonic, magmatic, and metallogenic evolution of the Tethyan orogen: From subduction to collision. Ore Geology Reviews, 70, 323-345.

Richards, J. P. (2009). Postsubduction porphyry Cu-Au and epithermal Au deposits: Products of remelting of subduction-modified lithosphere. Geology, 37 (3), 247-250.

Richards, J. P., Wilkinson, D., & Ullrich, T. (2006). Geology of the Sari Gunay epithermal gold deposit, northwest Iran. Economic Geology, 101(8), 1455-1496.

Rutherford, M., and Hill, P. (1993). Magma Ascent Rates from Amphibole Breakdown: An Experimental Study Applied to the 1980-1986 Mount St. Helens Eruptions. Journal of Geophysical Research, 98(B11), 19667–19685.

Şengör, A. M. C., and Yilmaz, Y. (1981). Tethyan evolution of Turkey: A plate tectonic approach. Tectonophysics, 75(3–4).

Seyitoğlu, G., and Büyükönal, G. (1995). Geochemistry of Ankara Volcanics and the implications of their K-Ar dates on the Cenozoic stratigraphy of central Turkey. Turkish Journal of Earth Sciences, 4, 77-92.

Scotese, C.R., 2007. Atlas of Earth History. Paleogeography: PALEOMAP Project, Arlington, Texas vol. 1, 52 pp.

Sherlock, R. L., Tosdal, R. M., Lehrman, N.J., Graney, J. R., Losh, S., Jowett, E. C., and Kesler, S. R. (1995). Origin of the McLaughlin Mine sheeted vein complex; metal zoning, fluid inclusion, and isotopic evidence. Econ Geol 90(8), 2156-2181.

Sillitoe, R. H., and Hedenquist, J. W. (2003). Linkages between volcanotectonic settings, ore-fluid compositions, and epithermal precious-metal deposits. Society of Economic Geologists. Special Publication, 10, 315–343.

Sillitoe, R. H. (2002). Some metallogenic features of gold and copper deposits related to alkaline rocks and consequences for exploration. Mineralium Deposita, 37, 4–13.

Sillitoe, R. H. (1997). Characteristics and controls of the largest porphyry copper-gold and epithermal gold deposits in the circum-Pacific region. Australian Journal of Earth Sciences, 44(3), 373–388.

Sillitoe, R. H. (1993). Giant and bonanza gold deposits in the epithermal environment: Assessment of potential genetic factors. BH Whiting, CJ Hodgson and R. Mason. Society of Economic Geologists, Special Publication, (3), 125-156.

Sillitoe, R. H. (1977). Metallic mineralization affiliated to subaerial volcanism. Geological Society, London, Special Publications, 7, 99–116.

Simmons, S. F., and Christenson, B. W. (1994). Origins of calcite in a boiling geothermal system. American Journal of Science, 294(March), 361–400.

Simmons, S. F., White, N. C., and John, D. A. (2005). Geological characteristics of epithermal precious and base metal deposits. Economic Geology 100th Anniversary, 29(January 2005), 485–522.

Sun, S. S., and McDonough, W. F. (1989). Chemical and isotopic systematics of oceanic basalts: Imlications for mantle composition and processes. Geological Society, London, Special Publications, 42, 313-345.

Stoffregren, R. E. (1987). Genesis of acid-sulfate alteration and Au-Cu-Ag mineralization at Summitville, Colorado. Economic Geology, 82, 1575–1591.

Şen, P. A. (2009). Trace element modelling of the origin and evolution of the Oyaca-Boyalik volcanic rocks (NE of Haymana, Ankara, Turkey). International Geology Review, 51(2), 116–132.

Şen, P. A., Temel, A., and Gourgaud, A. (2004). Petrogenetic modelling of Quaternary post-collisional volcanism: a case study of central and eastern Anatolia. Geological Magazine, 141(1), 81–98.

Tankut, A. (1985). Ankara dolaylarındaki Neojen yaşlı volkaniklerin jeokimyası. Türkiye Jeoloji Bülteni, 28(1973), 55–66.

Tankut, A. (2008). Basic and ultrabasic rocks from the Ankara Melange, Turkey. Geological Society, London, Special Publications, 17(1), 449–454.

Tankut, A., Dilek, Y., and Önen, P. (1998). Petrology and geochemistry of the Neo-Tethyan volcanism as revealed in the Ankara melange, Turkey. Journal of Volcanology and Geothermal Research, 85(1–4), 265–284.

Tankut, A., Wilson, M., and Yihunie, T. (1998). Geochemistry and tectonic setting of Tertiary volcanism in the. North, 285–301.

Taylor, B. E. (2007). Mineral deposits of Canada: A Synthesis of Major Deposit Types, District Metallogeny, the Evolution of Geological Provinces, and Exploration Methods. Geological Association of Canada, Mineral Deposits Division, Special Publication (5), 113–139.

Temel, A. (2001). Post-collisional miocene alkaline volcanism in the oglakçi region, Turkey: Petrology and geochemistry. International Geology Review, 43(7), 640–660.

Temel, A., Gündogdu, M. N., Gourgaud, A., and Le Pennec, J. L. (1998). Ignimbrites of Cappadocia (Central Anatolia, Turkey): Petrology and geochemistry. Journal of Volcanology and Geothermal Research, 85(1–4), 447–471.

Temel, A., Gündogdu, M. Niyazi, and Gourgaud, A. (1998). Petrological and geochemical characteristics of Cenozoic high-K calc-alkaline volcanism in Konya, Central Anatolia, Turkey. Journal of Volcanology and Geothermal Research, 85(1–4), 327–354.

Temel, A., Yürür, T., Alici, P., Varol, E., Gourgaud, A., Bellon, H., and Demirbağ, H. (2010). Alkaline series related to Early-Middle Miocene intra-continental rifting in a collision zone: An example from Polatli, Central Anatolia, Turkey. Journal of Asian Earth Sciences, 38(6), 289–306.

Toprak, V., Savascin, Y., Gulec, N., and Tankut, A. (1996). Structure of the galatean volcanic province, turkey. International Geology Review, 38(8), 747–758.

Toprak, V., and Göncüoglu, M. C. (1993). Tectonic control on the development of the Neogene-Quaternary Central Anatolian Volcanic Province, Turkey. Geological Journal, 28(3–4), 357–369.

Türkecan, A., Hepşen, N., Papak, İ., Akbaş, B., Dinçel, A., Karataş, S., Sevin, M., Özgür, İ. B., Bedi, Y., Mutlu, G., Sevin, D., Ünay, E., and Saraç, G. (1991). Seben-Gerede (Bolu)-Güdü Beypazarı (Ankara) ve Çerkeş-Orta-Kurşunlu

(Çankırı) yörelerinin (Köroğlu Dağları) jeolojisi ve volkanik kayaçların petrolojisi. Ankara.

Ünal İmer, E., Güleç, N., Kuşçu, İ., and Fallick, A. E. (2013). Genetic investigation and comparison of Kartaldağ and Madendağ epithermal gold deposits in Çanakkale, NW Turkey. Ore Geology Reviews 53, 204-222.

Varol, E., Temel, A., and Gourgaud, A. (2008). Textural and compositional evidence for magma mixing in the evolution of the çamlıdere volcanic rocks (Galatean Volcanic Province), Central Anatolia, Turkey. Turkish Journal of Earth Sciences, 17(4), 709–727.

Varol, E., Temel, A., Gourgaud, A., and Bellon, H. (2007). Early Miocene adakite-like volcanism in the Balkuyumcu region, central Anatolia, Turkey: Petrology and geochemistry. Journal of Asian Earth Sciences, 30(5–6), 613–628.

Varol, E., Temel, A., Yürür, T., Gourgaud, A., and Bellon, H. (2014). Petrogenesis of the Neogene bimodal magmatism of the Galatean Volcanic Province, Central Anatolia, Turkey. Journal of Volcanology and Geothermal Research, 280, 14–29. https://doi.org/10.1016/j.jvolgeores.2014.04.014

White, N. C., and Hedenquist, J. W. (1995). Epithermal Gold Deposits: Styles, Characteristics and Exploration. SEG Newsletter, 23(January 1995).

White, N. C., and Hedenquist, J. W. (1990). Epithermal environments and styles of mineralization: Variations and their causes, and guidelines for exploration. Journal of Geochemical Exploration, 36(1–3), 445–474.

Wilson, C., and Tunningley, A. (2013). Understanding Low Sulphidation (LS) Epithermal Deposits. (July).

Wilson, M., Tankut, A., and Guleç, N. (1997). Tertiary volcanism of the Galatia province, north-west Central Anatolia, Turkey. Lithos, 42(1–2), 105–121.

Winchester, J. A., and Floyd, P. A. (1976). Geochemical magma type discrimination application to altered and metamorphosed basic igneous rocks. Earth and Planetary Sciences Letters, 28, 459–469.

Yigit, O. (2006). Gold in Turkey - A missing link in Tethyan metallogeny. Ore Geology Reviews, 28(2), 147–179.

Yigit, O. (2009). Mineral deposits of Turkey in relation to tethyan metallogeny: Implications for future mineral exploration. Economic Geology, 104(1), 19–51.

Yürür, T., Temel, A., and Köse, O. (2002). Evidences of Extensional Tectonics at the Southern Boundary of the Galatean Volcanic Province, NW Central Anatolia. Geological Bulletin of Turkey, 45(1), 85–98.

Adıyaman, Ö. And Chorowicz, J. 2002. Late Cenozoic tectonics and volcanics in the northwestern corner of the Arabian plate: a consequence of the strike-slip Dead Sea Fault Zone and lateral escape of Anatolia, Journal of Volcanology and Geothermal Research, 117. 327-345.

A. Compositional Data from Hornblende Phenocrysts.

Sample No.	G1-2-1	G1-2-2	G1-2-3	G1-4-1	G1-4-2	G1-5-1	G1-5-2	G1-5-3	G1-5-4	G1-5-5	G12-2-1	G12-2-2	G12-2-3	G12-4-1	G12-4-2	G12-4-3	G12-6-1	G12-6-2	G12-6-3	G12-7-1	G12-7-2	G12-7-3
Na_2O	1.16	1.16	1.11	1.07	1.08	1.22	1.04	1.32	1.12	1.25	1.21	1.22	1.54	1.14	1.21	0.89	1.08	0.98	1.17	1.27	1.07	1.18
SiO_2	48.57	48.25	48.69	49.22	49.38	48.38	49.75	47.05	49.21	47.36	47.43	48.23	44.94	48.76	48.57	49.36	48.47	49.08	48.18	48.80	49.76	48.46
Al_2O_3	6.39	6.43	6.10	6.05	6.73	6.46	5.67	7.44	6.12	7.21	6.90	6.70	8.68	6.01	6.29	4.94	5.93	5.69	6.33	6.56	5.70	6.40
MgO	15.84	15.40	15.68	15.86	15.85	15.54	16.09	14.89	15.91	15.15	14.44	15.32	13.89	15.83	15.46	15.98	15.52	15.91	15.39	15.70	15.98	15.39
K_2O	0.369	0.421	0.373	0.323	0.342	0.349	0.305	0.414	0.302	0.406	0.433	0.417	0.549	0.318	0.328	0.267	0.333	0.312	0.352	0.342	0.289	0.356
CaO	11.06	11.29	11.19	10.97	10.78	10.74	10.93	10.88	10.89	10.80	10.94	11.13	11.10	10.79	11.04	10.78	11.03	10.91	11.07	10.78	10.96	11.02
FeO	11.99	11.98	11.75	11.73	12.33	11.76	11.45	12.34	11.51	12.27	12.39	11.80	13.18	11.30	11.72	11.06	11.60	11.56	11.94	12.06	11.39	11.68
MnO	0.426	0.402	0.381	0.435	0.478	0.379	0.368	0.406	0.401	0.397	0.350	0.354	0.335	0.413	0.447	0.433	0.425	0.443	0.404	0.372	0.451	0.442
NiO	0.00	0.030	0.005	0.00	0.017	0.00	0.028	0.006	0.009	0.016	0.029	0.014	0.036	0.017	0.00	0.033	0.010	0.024	0.016	0.00	0.006	0.013
TiO_2	1.16	1.10	1.09	1.06	1.17	1.23	1.03	1.42	1.16	1.31	1.52	1.20	1.67	1.10	1.21	0.93	1.15	1.07	1.43	1.21	0.99	1.24
Cr_2O_3	0.00	0.00	0.002	0.007	0.00	0.00	0.00	0.015	0.001	0.007	0.00	0.00	0.037	0.023	0.00	0.010	0.003	0.042	0.009	0.019	0.021	0.104
O	1.82	1.81	1.81	1.82	1.85	1.81	1.83	1.80	1.82	1.80	1.79	1.81	1.78	1.81	1.81	1.79	1.80	1.81	1.81	1.83	1.83	1.81
Total	98.79	98.27	98.18	98.54	100.0	97.86	98.49	97.98	98.45	97.97	97.43	98.19	97.74	97.51	98.09	96.47	97.36	97.84	98.10	98.95	98.44	98.09

B. Compositional Data from Biotite Phenocrysts.

Sample No.	G1-4-1	G1-4-2	G1-4-3
Na_2O	0.68	0.74	0.47
SiO_2	37.70	37.92	38.26
Al_2O_3	13.86	13.95	14.25
MgO	14.90	15.68	13.77
K_2O	8.680	8.480	8.810
CaO	0.04	0.02	0.05
FeO	14.33	13.40	14.57
MnO	0.156	0.126	0.129
NiO	0.010	0.013	0.000
TiO_2	4.36	4.14	4.42
Cr_2O_3	0.00	0.00	0.038
O	3.56	3.57	3.57
Total	98.28	98.04	98.34

C. Compositional Data from Plagioclase Phenocrysts.

Sample No.	Na_2O	SiO_2	Al_2O_3	K_2O	CaO	SrO	BaO	FeO	Total
G1-1-1	6.21	58.53	25.70	0.441	7.94	0.077	0.032	0.210	99.14
G1-1-2	6.34	58.74	25.88	0.423	7.84	0.154	0.010	0.208	99.59
G1-1-3	6.20	58.72	25.65	0.470	7.90	0.135	0.051	0.208	99.33
G1-1-4	6.31	58.44	26.08	0.390	8.15	0.113	0.043	0.211	99.74
G1-1-5	5.87	57.52	26.62	0.357	8.77	0.147	0.062	0.195	99.54
G1-1-6	6.76	60.11	25.06	0.516	7.17	0.143	0.050	0.219	100.03
G1-3-1	6.17	59.01	25.59	0.423	7.70	0.144	0.053	0.233	99.32
G1-3-2	6.26	58.49	25.80	0.367	8.03	0.110	0.048	0.228	99.33
G1-3-3	6.34	58.50	25.68	0.415	7.92	0.115	0.048	0.225	99.24
G1-3-4	6.54	59.68	25.14	0.443	7.30	0.108	0.067	0.210	99.49
G1-3-5	6.39	59.27	25.38	0.449	7.43	0.181	0.039	0.201	99.34
G1-6-1	6.46	58.93	25.44	0.423	7.54	0.152	0.011	0.195	99.15
G1-6-2	5.89	57.45	26.46	0.346	8.66	0.132	0.000	0.186	99.12
G1-6-3	6.29	58.74	25.87	0.401	7.83	0.094	0.021	0.227	99.47
G1-6-4	5.99	57.37	26.38	0.330	8.80	0.122	0.028	0.159	99.18
G1-6-5	5.77	57.12	26.84	0.314	9.02	0.135	0.027	0.183	99.41
G1-7-1	5.82	57.86	26.39	0.342	8.47	0.140	0.067	0.211	99.30
G1-7-2	6.25	58.84	25.62	0.419	7.86	0.130	0.092	0.203	99.41
G1-7-3	6.32	58.45	25.71	0.407	7.85	0.149	0.059	0.205	99.15
G1-7-4	5.59	56.70	26.68	0.328	9.16	0.117	0.025	0.209	98.81
G1-7-5	6.72	59.76	24.97	0.478	7.02	0.095	0.025	0.234	99.30
G1-7-6	6.35	58.58	25.63	0.423	7.67	0.122	0.059	0.204	99.04
G12-1-1	5.86	57.79	25.99	0.418	8.38	0.141	0.000	0.224	98.80
G12-1-2	5.65	57.39	26.17	0.374	8.61	0.156	0.063	0.200	98.61
G12-1-3	5.96	57.82	25.84	0.400	8.11	0.117	0.134	0.212	98.59
G12-1-4	6.49	59.33	24.87	0.452	7.17	0.126	0.000	0.205	98.64
G12-1-5	6.05	58.47	25.75	0.414	7.97	0.120	0.068	0.236	99.08
G12-5-1	6.41	58.76	25.27	0.436	7.57	0.112	0.068	0.216	98.84
G12-5-2	6.12	58.01	26.22	0.383	8.16	0.137	0.027	0.198	99.25
G12-5-3	5.80	57.23	26.45	0.347	8.81	0.121	0.024	0.205	98.99
G12-5-4	5.79	57.24	26.48	0.345	8.84	0.122	0.016	0.237	99.07
G12-5-5	6.54	59.24	24.77	0.495	7.07	0.131	0.003	0.201	98.45
G12-8-1	6.16	59.55	24.82	1.009	7.27	0.123	0.066	0.211	99.21
G12-8-2	4.99	54.94	28.01	0.262	10.39	0.155	0.035	0.209	98.99
G12-8-3	5.77	57.30	26.34	0.381	8.72	0.092	0.027	0.192	98.82
G12-6-1	6.43	58.78	25.19	0.464	7.52	0.128	0.106	0.302	98.92
G12-6-2	6.38	58.71	25.59	0.414	7.87	0.133	0.031	0.215	99.34

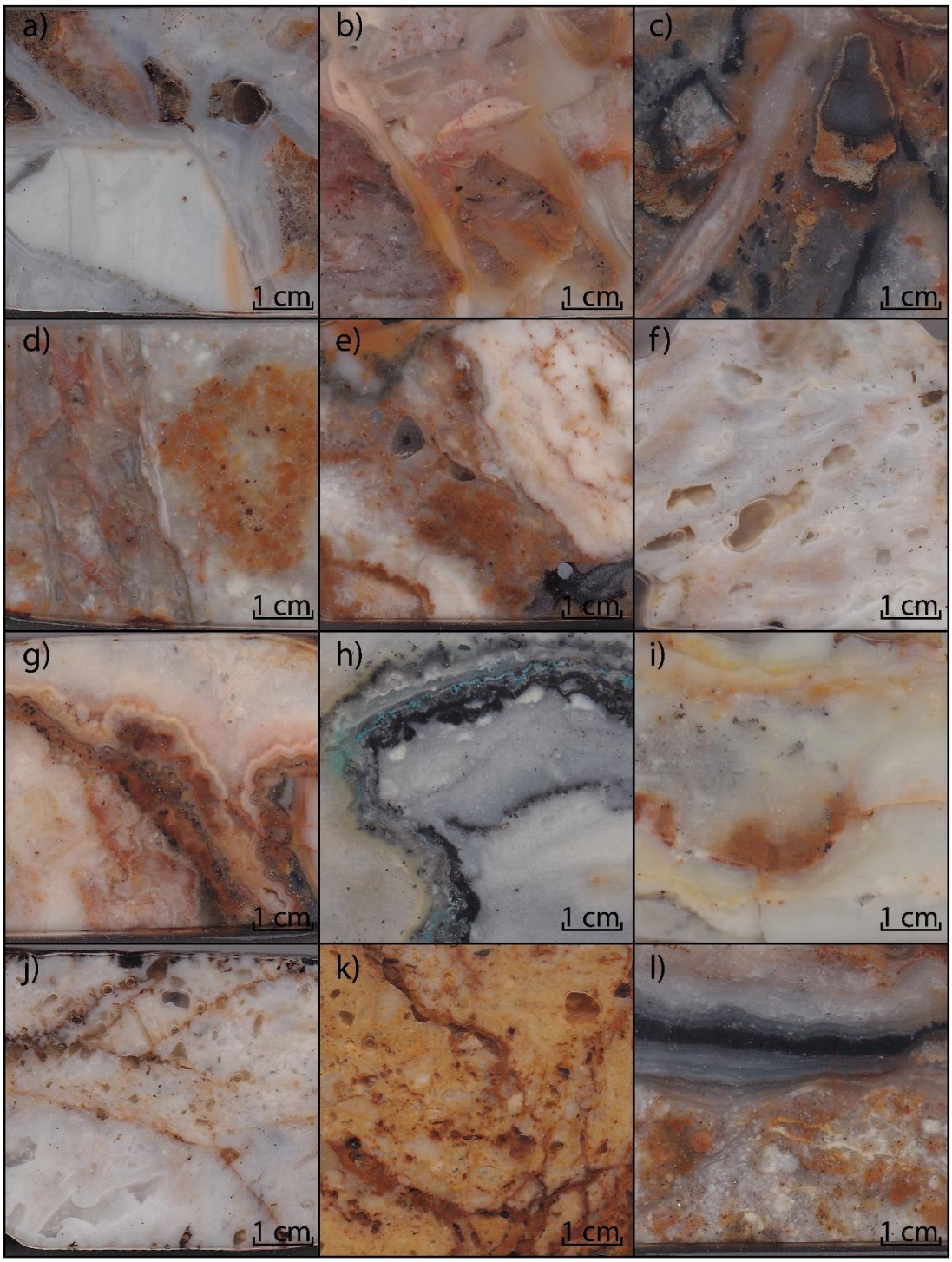
D. Compositional Data from magnetite Phenocrysts.

Sample No.	MgO	Al_2O_3	SiO_2	FeO	TiO_2	MnO	V_2O_3	NiO	Cr_2O_3	CaO	Total
G1-8-2-3	1.84	1.73	0.030	80.31	4.55	0.608	0.043	0.048	0.092	0.026	89.27
G1-8-2-4	2.28	1.91	0.052	78.90	4.88	0.658	0.045	0.026	0.078	0.052	88.88
G1-8-3-1	1.39	0.96	0.510	70.46	16.12	0.259	0.162	0.002	0.098	0.083	90.05
G1-9-1-2	1.38	1.99	0.00	81.94	3.25	0.347	0.025	0.036	0.082	0.021	89.07
G1-9-3-1	1.69	1.71	0.421	71.61	3.45	0.374	0.327	0.030	0.089	5.980	85.68
G1-9-3-2	1.09	2.14	0.012	81.75	2.68	0.360	0.278	0.009	0.113	0.125	88.56
G1-9-4-1	1.46	1.47	0.035	81.62	3.17	0.438	0.066	0.030	0.081	0.111	88.48
G1-9-4-2	1.45	1.92	0.050	80.86	3.30	0.400	0.057	0.020	0.073	0.031	88.16
G1-9-4-3	1.33	1.60	0.00	81.79	3.18	0.401	0.047	0.024	0.083	0.049	88.50
G1-9-4-4	1.26	1.99	0.013	82.05	2.94	0.407	0.079	0.041	0.085	0.060	88.93
G1-9-4-5	1.47	1.35	0.449	81.12	3.45	0.416	0.027	0.005	0.088	0.112	88.49

E. Compositional Data from Ilmenite Phenocrysts.

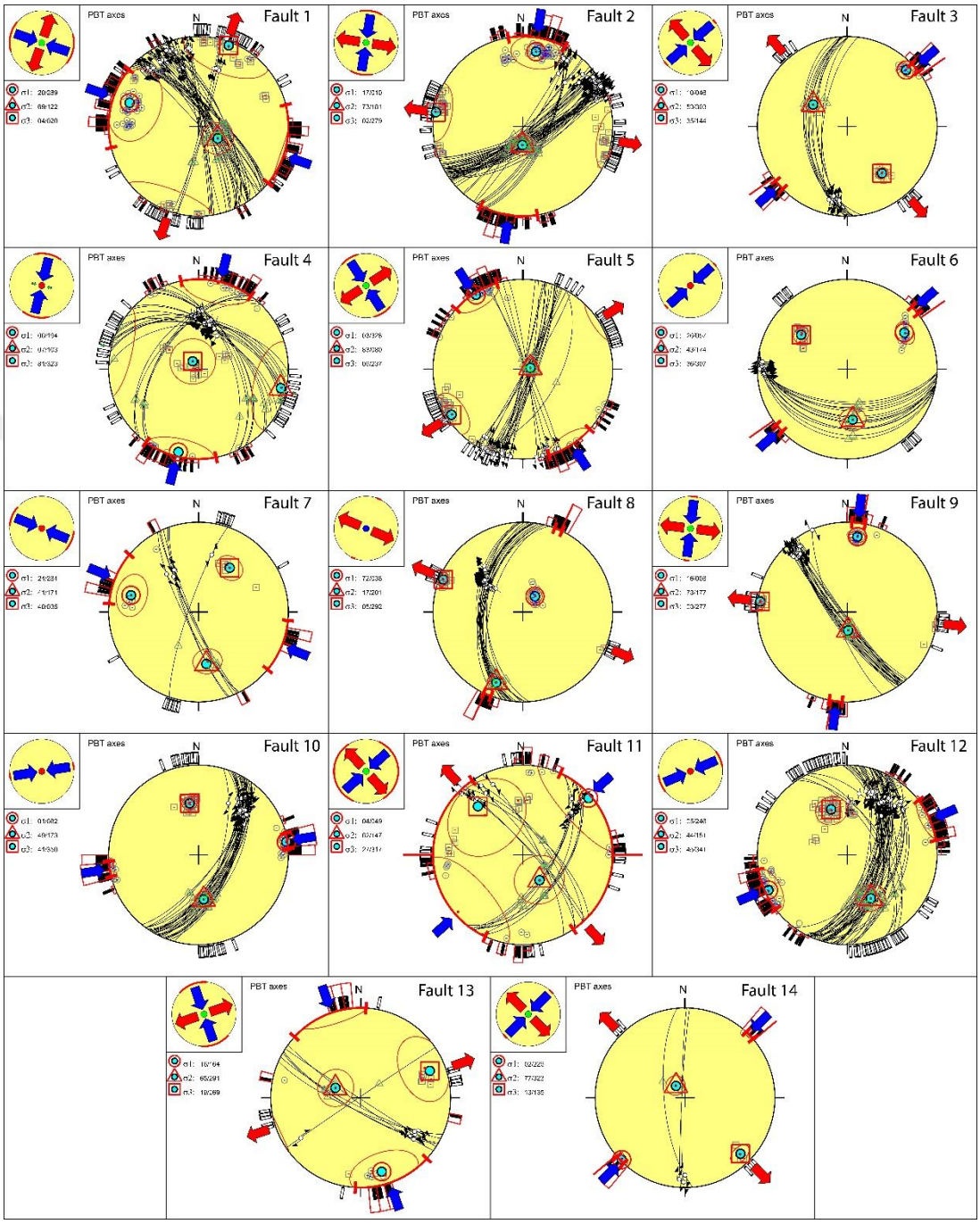
Sample No.	MgO	Al_2O_3	SiO_2	FeO	TiO_2	MnO	V_2O_3	NiO	Cr_2O_3	CaO	Total
G1-8-1-1	2.17	0.55	0.049	48.46	38.77	0.532	0.244	0.025	0.048	0.082	90.93
G1-8-1-2	1.35	0.37	3.850	57.86	26.90	0.543	0.257	0.024	0.009	0.102	91.27
G1-8-2-1	2.43	0.99	0.048	47.03	40.62	0.449	0.170	0.000	0.001	0.051	91.79
G1-8-2-2	1.65	0.72	0.014	48.60	39.91	0.471	0.155	0.030	0.022	0.026	91.60
G1-8-3-2	2.35	1.26	0.023	44.67	42.94	0.191	0.344	0.011	0.009	0.046	91.84
G1-9-1-1	1.84	0.72	0.054	46.96	41.41	0.300	0.144	0.017	0.016	0.016	91.48
G1-9-2-1	2.40	0.62	0.049	52.53	33.50	0.259	0.271	0.024	0.114	0.085	89.85
G1-9-2-2	1.63	0.58	0.005	51.79	36.23	0.231	0.380	0.00	0.055	0.056	90.96

F. Hydrothermal Vein Textures.

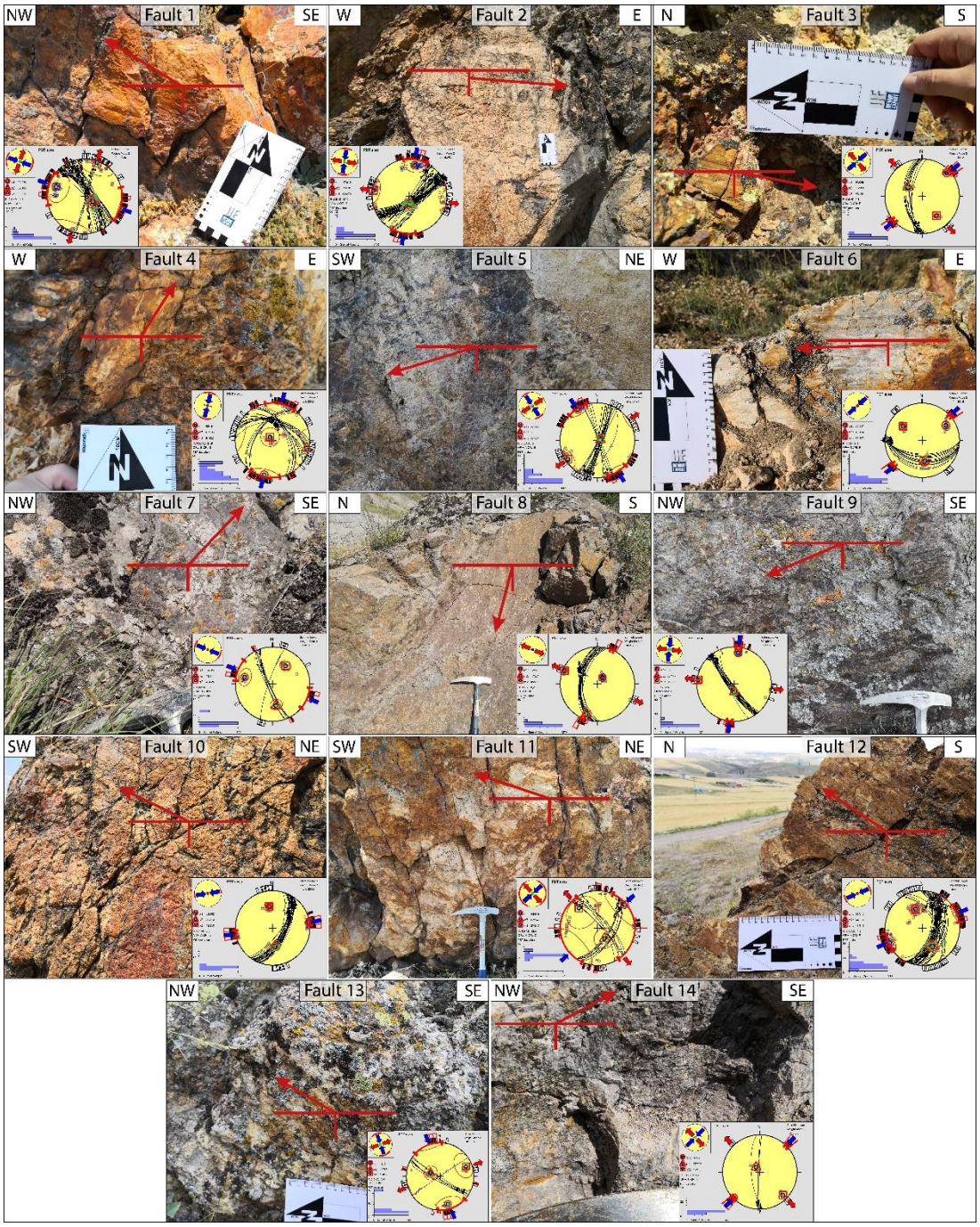


a) hydrothermal breccia with colloform banding (Sample GCK-25), b) hydrothermal breccia with colloform banding (Sample GCK-55), c) quartz veinlet cutting hydrothermal breccia (Sample GCK-51), d) hydrothermal breccia cutting silicified andesite (Sample GCK-49), e) quartz vein cutting pyrite hosted hydrothermal breccia (Sample GCK-32-A), f) chalcedonic quartz (Sample GCK-39), g) colloform bands with pyrite (Sample GCK-30), h) colloform banding with pyrite/arsenopyrite together with metallic mineral (Sample GCK-64-1), i) hydrothermal breccia with disseminated metallic mineral surrounded by chalcedony (Sample GCK-65), j) lattice bladed texture (Sample GCK-26), k) lattice bladed texture (Sample GCK-66), l) colloform dark colored bands with pyrite surrounded by pyrite bearing quartz band (Sample GCK-48).

G. Paleostress Reconstruction Results.



H. Sense of Movement on the Fault Surfaces.



I. Compositional Data from Pyrite and Arsenopyrite Minerals.

Sample No.	As	Se	S	Sb	Mo	Cu	Pb	Zn	Fe	Hg	Co	Bi	Cd	Te	Ag	Au	Total
G61-1-1-1 py	0.0058	0.0041	53.10	0.0033	0.00	0.0052	0.00	0.0314	45.62	0.00	0.00	0.00	0.0121	0.00	0.00	0.00	98.78
G61-1-1-2 py	0.00	0.0017	53.21	0.0141	0.00	0.0045	0.00	0.0223	46.07	0.00	0.00	0.00	0.0232	0.0146	0.0060	0.0055	99.37
G61-1-1-3 py	0.0183	0.00	53.11	0.00	0.00	0.0139	0.00	0.0104	45.99	0.00	0.00	0.00	0.00	0.0166	0.0042	0.00	99.16
G61-1-2-1 py	0.0999	0.0068	53.33	0.0023	0.00	0.0196	0.00	0.0292	45.37	0.00	0.00	0.00	0.0345	0.00	0.00	0.00	98.89
G61-1-2-2 py	0.00	0.00	53.37	0.00	0.00	0.0389	0.00	0.0158	45.93	0.00	0.00	0.00	0.0247	0.00	0.00	0.00	99.38
G61-1-3-1 py	0.00	0.0017	52.86	0.00	0.00	0.0000	0.00	0.00	45.97	0.00	0.00	0.00	0.0045	0.0132	0.00	0.00	98.85
G61-1-3-2 py	0.1201	0.00	52.56	0.00	0.00	0.0187	0.00	0.0403	45.78	0.00	0.00	0.00	0.00	0.00	0.0110	0.00	98.53
G61-1-3-3 py	0.00	0.0242	53.49	0.0204	0.00	0.0021	0.00	0.0034	46.25	0.00	0.00	0.00	0.0253	0.00	0.0042	0.00	99.82
G61-1-4-1 py	0.8640	0.0070	52.80	0.0449	0.00	0.1226	0.00	0.00	45.45	0.00	0.00	0.00	0.0107	0.00	0.00	0.0405	99.34
G61-2-2-1 py	0.0011	0.0383	53.61	0.00	0.00	0.00	0.00	0.0004	46.05	0.00	0.00	0.00	0.0154	0.00	0.00	0.0285	99.74
G61-2-2-2 py	0.0622	0.00	53.34	0.00	0.00	0.00	0.00	0.0236	46.09	0.00	0.00	0.00	0.00	0.00	0.0076	0.0049	99.53
G61-2-2-3 py	0.00	0.00	53.52	0.00	0.00	0.00	0.00	0.00	45.95	0.00	0.00	0.00	0.00	0.0039	0.0007	0.0134	99.49
G61-3-1-1 py	0.00	0.00	53.33	0.0077	0.00	0.00	0.00	0.0121	45.51	0.00	0.00	0.00	0.0246	0.00	0.0093	0.00	98.89
G61-3-1-2 py	0.0609	0.0373	52.93	0.00	0.00	0.00	0.00	0.00	45.38	0.00	0.00	0.00	0.00	0.00	0.0291	0.0062	98.44
G61-3-1-3 py	0.0402	0.00	52.99	0.00	0.00	0.00	0.00	0.0079	44.36	0.00	0.00	0.00	0.0150	0.00	0.0257	0.0016	97.44
G61-3-2-1 py	0.2023	0.00	53.59	0.0087	0.00	0.0117	0.00	0.00	45.92	0.00	0.00	0.00	0.0204	0.00	0.00	0.0032	99.56
G61-3-2-2 py	0.2657	0.0407	53.21	0.0364	0.00	0.00	0.00	0.00	45.84	0.00	0.00	0.00	0.0212	0.0126	0.00	0.0068	99.43
G61-3-2-3 py	0.00	0.00	53.61	0.00	0.00	0.0050	0.00	0.0287	45.58	0.00	0.00	0.00	0.0311	0.00	0.00	0.00	99.25

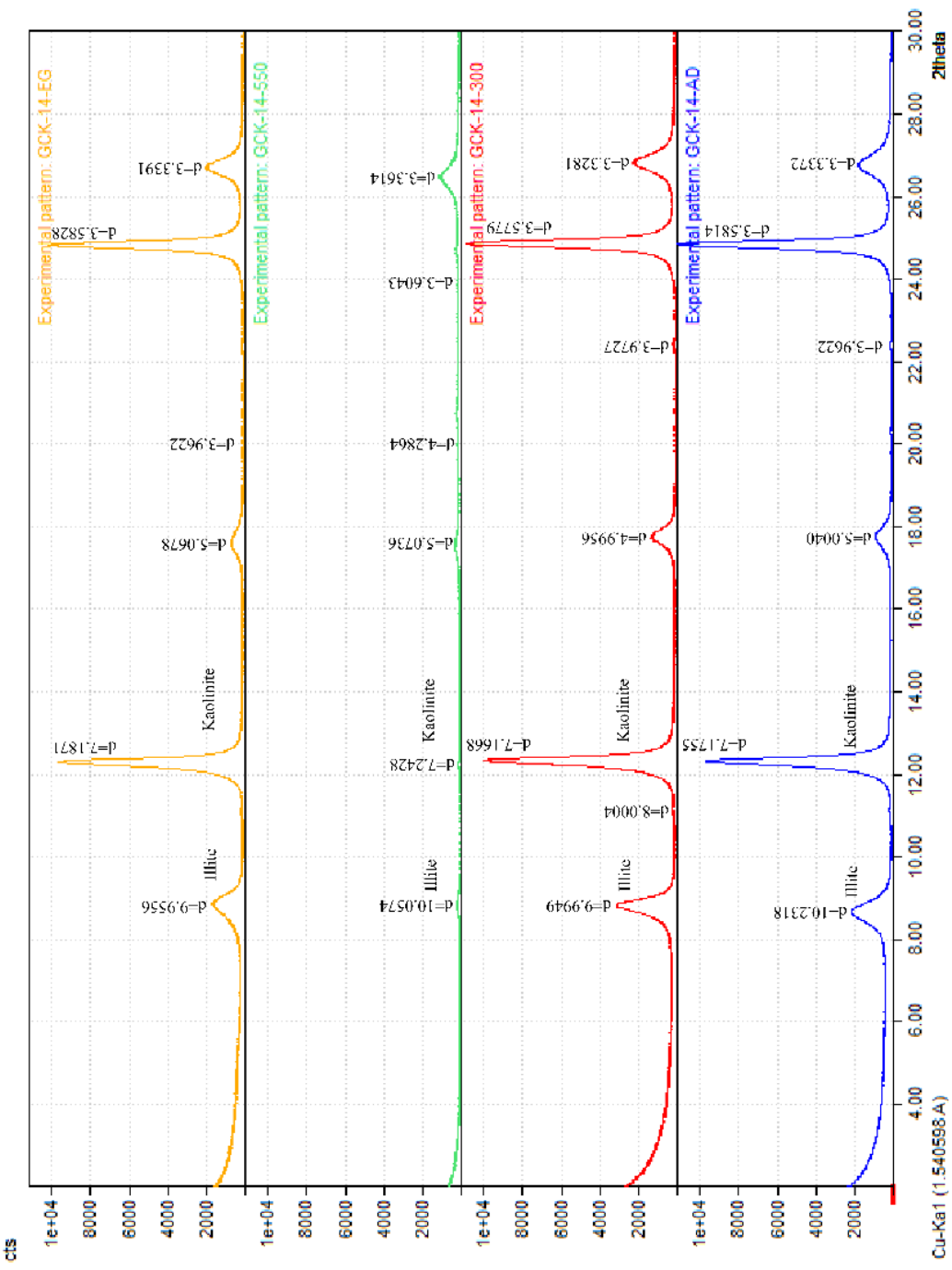
Sample No.	As	Se	S	Sb	Mo	Cu	Pb	Zn	Fe	Hg	Co	Bi	Cd	Te	Ag	Au	Total
G61-3-2-4 py	0.1162	0.00	53.51	0.00	0.00	0.0133	0.00	0.0550	45.54	0.00	0.00	0.00	0.0062	0.00	0.0019	0.0121	99.25
G61-3-2-5 py	0.1043	0.00	52.64	0.3410	0.00	0.0135	0.00	0.0245	45.38	0.00	0.00	0.00	0.0066	0.00	0.00	0.00	98.51
G61-3-2-6 py	0.0509	0.0156	53.22	0.0027	0.00	0.0004	0.00	0.0079	45.90	0.00	0.00	0.00	0.00	0.00	0.0045	0.0386	99.24
G61-3-3-1 py	2.1800	0.0115	52.89	0.0167	0.00	0.0164	0.00	0.0064	45.41	0.00	0.00	0.00	0.00	0.00	0.0071	0.00	100.54
G61-3-3-2 py	0.00	0.00	53.64	0.0124	0.00	0.0158	0.00	0.0136	45.89	0.00	0.00	0.00	0.0199	0.0013	0.00	0.0074	99.60
G61-3-3-3 py	0.00	0.0413	53.63	0.00	0.00	0.1159	0.00	0.00	45.76	0.00	0.00	0.00	0.0062	0.0097	0.0074	0.0145	99.59
G642-5-1 py	0.00	0.0309	53.53	0.00	0.00	0.0226	0.00	0.00	46.54	0.00	0.00	0.00	0.00	0.0231	0.0129	0.00	100.16
G642-5-2 py	0.00	0.00	53.50	0.00	0.00	0.0085	0.00	0.00	46.54	0.00	0.00	0.00	0.0132	0.00	0.00	0.00	100.06
G642-5-3 py	0.0026	0.0425	53.68	0.00	0.00	0.0038	0.00	0.00	46.46	0.00	0.00	0.00	0.0076	0.00	0.0148	0.00	100.21
G642-5-4 py	0.2331	0.00	53.40	0.00	0.00	0.00	0.00	0.0210	46.58	0.00	0.00	0.00	0.0079	0.0127	0.00	0.00	100.25
G642-5-5 py	0.0854	0.00	52.44	0.00	0.00	0.0321	0.00	0.0195	45.51	0.00	0.00	0.00	0.0107	0.00	0.00	0.0188	98.12
G642-5-6 py	0.9905	0.0042	52.74	0.0309	0.00	0.00	0.00	0.00	46.02	0.00	0.00	0.00	0.0079	0.00	0.00	0.0304	99.82
G642-5-7 py	0.00	0.0430	54.20	0.00	0.00	0.00	0.00	0.0123	46.62	0.00	0.00	0.00	0.0016	0.00	0.00	0.0097	100.89
G642-5-8 py	0.1299	0.0224	53.53	0.00	0.00	0.0017	0.00	0.0318	46.58	0.00	0.00	0.00	0.0305	0.00	0.0061	0.00	100.33
G61-2-1-1 apy	1.95	0.0331	40.86	0.0419	0.00	0.0808	0.00	0.00	35.51	0.00	0.00	0.00	0.00	0.0229	0.0208	0.00	78.520
G61-2-1-2 apy	1.06	0.00	33.39	0.0312	0.00	0.0259	0.00	0.00	28.78	0.00	0.00	0.00	0.0083	0.00	0.0045	0.0253	63.325
G61-2-1-3 apy	1.87	0.0117	28.90	0.0784	0.00	0.0383	0.00	0.0192	25.43	0.00	0.00	0.00	0.0129	0.00	0.0042	0.0184	56.383

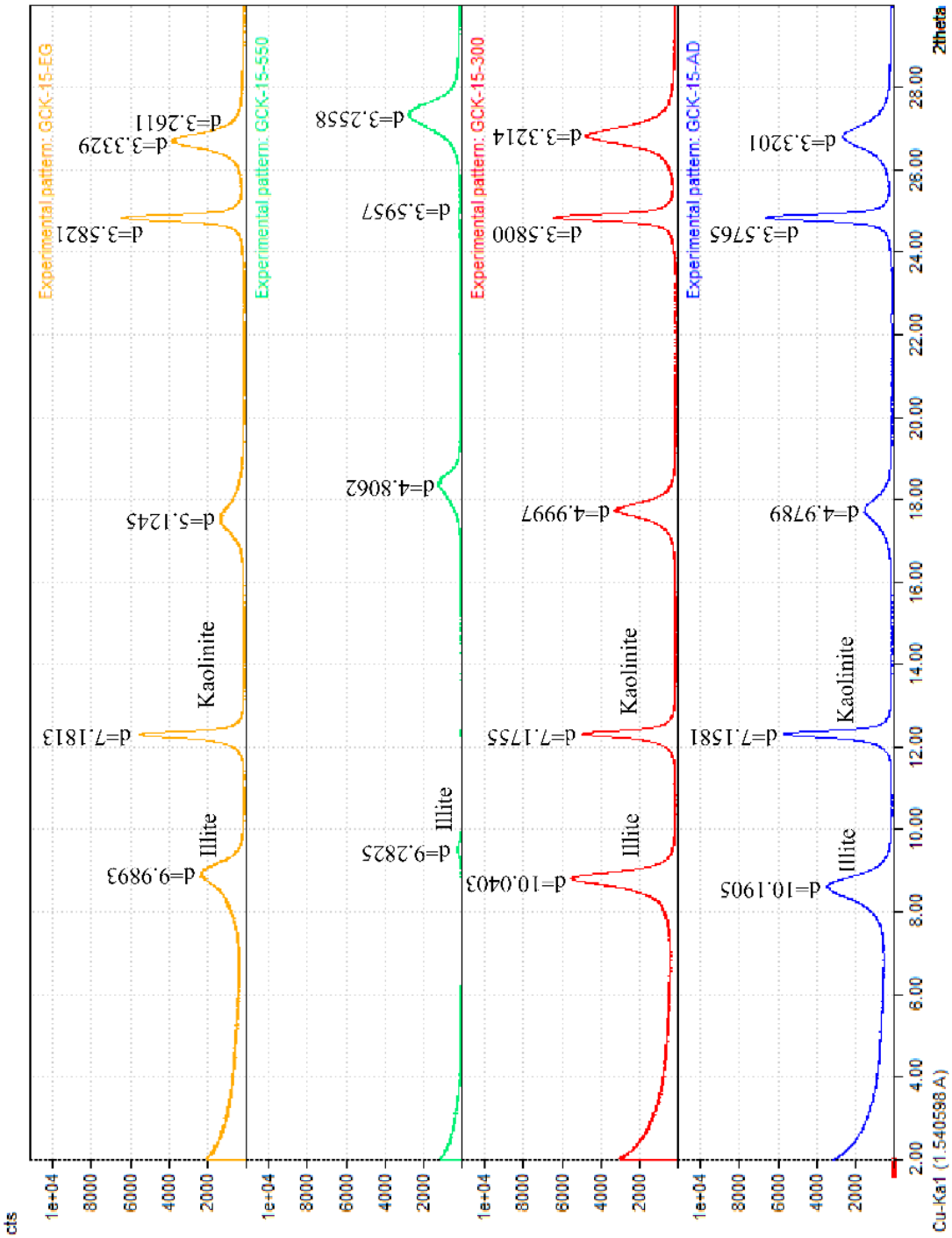
J. Compositional Data from Tetrahedrite Minerals.

Sample No.	As	Se	S	Sb	Mo	Cu	Pb	Zn	Fe	Hg	Co	Bi	Cd	Te	Ag	Au	Total
G641-1-1	4.92	0.2203	25.27	21.81	0.00	38.61	0.00	5.77	0.0590	0.00	0.0168	0.00	0.3120	0.00	1.5700	0.0283	98.59
G641-1-2	4.23	0.4018	25.00	24.28	0.00	37.19	0.00	6.61	0.1030	0.00	0.0080	0.00	0.2622	0.00	1.8200	0.0690	99.97
G641-1-3	5.42	0.3579	25.02	24.80	0.00	37.09	0.00	7.18	0.0962	0.0135	0.0032	0.00	0.3219	0.00	1.8400	0.0242	102.17
G641-1-4	5.33	0.3533	25.04	24.71	0.00	36.09	0.00	7.03	0.1187	0.00	0.0059	0.00	0.3236	0.00	2.8200	0.00	101.82
G641-1-5	5.09	0.4290	24.77	24.36	0.00	36.06	0.00	6.72	0.1131	0.00	0.00	0.00	0.3017	0.00	2.5100	0.00	100.35
G641-2-1	4.30	0.2831	25.34	24.27	0.00	37.91	0.00	6.55	0.0740	0.00	0.00	0.00	0.2375	0.00	1.4300	0.0237	100.42
G641-2-2	6.23	0.4049	25.05	24.31	0.00	36.82	0.00	7.08	0.1304	0.00	0.0023	0.00	0.3545	0.00	1.7800	0.00	102.16
G641-4-1	5.05	0.5800	24.43	15.93	0.00	40.59	0.00	3.80	0.0559	0.00	0.00	0.0112	0.4010	1.540	1.8700	0.00	94.26
G641-4-2	6.10	0.2976	25.02	24.88	0.00	36.55	0.00	7.58	0.1154	0.00	0.00	0.00	0.2872	0.00	2.2900	0.00	103.12
G641-4-3	4.38	0.3278	24.97	23.46	0.00	38.33	0.00	6.42	0.0575	0.00	0.00	0.00	0.3569	0.00	1.8000	0.00	100.10
G641-4-4	4.42	0.1980	25.07	21.90	0.00	38.99	0.00	5.76	0.0764	0.00	0.00	0.0055	0.2458	0.00	1.4100	0.0141	98.09
G641-4-5	5.66	0.3669	24.62	24.81	0.00	36.63	0.00	7.27	0.0961	0.0000	0.00	0.00	0.3066	0.00	2.4800	0.0476	102.29
G641-6-1	3.73	0.9593	23.86	19.07	0.00	36.70	0.00	4.33	0.0170	0.5131	0.00	0.0067	0.5850	0.00	5.8500	0.00	95.62
G641-6-2	4.45	0.7461	24.23	18.71	0.00	34.80	0.00	4.76	0.0142	0.1279	0.0100	0.0892	0.3403	0.00	8.5000	0.0080	96.79
G641-6-3	4.17	0.5969	24.32	22.50	0.00	34.99	0.00	5.92	0.0206	0.0960	0.0077	0.00	1.0800	0.00	5.5900	0.00	99.29
G641-6-4	4.82	0.7292	24.34	18.14	0.00	34.97	0.00	4.50	0.00	0.0943	0.00	0.0055	0.3560	0.00	8.4400	0.00	96.40
G642-1-1	6.50	0.3017	25.17	24.63	0.00	37.63	0.00	7.38	0.0600	0.0153	0.0118	0.00	0.3360	0.00	0.6333	0.0502	102.72
G642-1-2	7.59	0.3176	25.16	23.37	0.00	37.45	0.00	7.45	0.0769	0.00	0.0103	0.00	0.3074	0.00	0.6190	0.0279	102.38
G642-1-3	6.58	0.3121	24.97	24.86	0.00	37.61	0.00	7.45	0.0607	0.0617	0.0201	0.00	0.3192	0.00	0.5827	0.00	102.83
G642-2-1	7.08	0.1873	25.26	24.27	0.00	38.04	0.00	7.60	0.0785	0.00	0.00	0.00	0.3454	0.00	0.7230	0.0465	103.63

Sample No.	As	Se	S	Sb	Mo	Cu	Pb	Zn	Fe	Hg	Co	Bi	Cd	Te	Ag	Au	Total
G642-2-3	6.78	0.2651	25.38	24.56	0.00	37.83	0.00	7.49	0.0889	0.0136	0.0098	0.00	0.3216	0.00	0.6210	0.0280	103.39
G642-2-4	7.35	0.3382	25.29	23.61	0.00	37.67	0.00	7.37	0.0949	0.00	0.00	0.00	0.3687	0.00	0.8011	0.00	102.89
G642-2-5	6.81	0.4043	25.26	23.65	0.00	37.96	0.00	7.37	0.0509	0.00	0.0052	0.00	0.2875	0.00	0.4915	0.00	102.29
G642-2-6	6.80	0.3827	25.22	23.65	0.00	38.03	0.00	7.28	0.1036	0.00	0.00	0.00	0.3633	0.00	0.5269	0.00	102.36
G642-3-1	6.54	0.2501	25.20	24.47	0.00	37.80	0.00	7.43	0.0791	0.00	0.00	0.00	0.3577	0.00	0.7488	0.00	102.88
G642-3-2	7.20	0.3739	25.32	24.00	0.00	37.83	0.00	7.50	0.0648	0.00	0.00	0.00	0.3234	0.00	0.6163	0.0015	103.23
G642-3-3	7.45	0.3682	25.10	23.83	0.00	37.80	0.00	7.43	0.0966	0.0186	0.00	0.00	0.3375	0.00	0.8107	0.0221	103.26
G642-4-1	7.92	0.3085	25.37	23.65	0.00	37.91	0.00	7.38	0.0678	0.0254	0.00	0.00	0.3737	0.00	0.5844	0.00	103.59
G642-4-2	7.30	0.2968	25.21	24.07	0.00	37.95	0.00	7.42	0.0837	0.00	0.00	0.00	0.3651	0.00	0.6056	0.0141	103.32
G642-4-3	5.77	0.3748	25.05	24.90	0.00	37.81	0.00	7.34	0.0766	0.00	0.00	0.00	0.2856	0.00	0.5859	0.00	102.19
G642-4-1	4.24	0.4328	25.06	20.20	0.00	39.85	0.00	5.06	0.0386	0.00	0.00	0.00	0.2087	0.00	0.4237	0.0529	95.57
G642-4-5	3.69	0.5868	24.99	17.74	0.00	41.32	0.00	4.09	0.0491	0.00	0.00	0.00	0.1396	0.283	0.3636	0.00	93.25
G642-4-6	4.08	0.6017	25.09	18.55	0.00	40.88	0.00	4.54	0.0184	0.0135	0.00	0.00	0.1632	0.00	0.4883	0.00	94.43

K. XRD Analyses Results of Samples GCK-14 (497261E, 4429301E) and GCK-15 (497262E, 4429292N).




cts
Experimental pattern: GCK-15-EG
Experimental pattern: GCK-15-550
Experimental pattern: GCK-15-300
Experimental pattern: GCK-15-AD
d=9.9893
Illite
d=7.1813
Kaolinite
d=5.1245
d=3.5821
d=3.3329
d=3.2611
d=9.2825
Illite
d=4.8062
d=3.5957
d=3.2558
d=10.0403
Illite
d=7.1755
Kaolinite
d=4.9997
d=3.5800
d=3.2314
d=10.1905
Illite
d=7.1581
Kaolinite
d=4.9789
d=3.5765
d=3.3201
Cu-Ka1 (1.540598 A)
2theta

L. $^{40}Ar/^{39}Ar$ Analyses Results of Samples 542639 and 661564.

Laser	*Isotope Ratios*												
	542639 sericite				*(sample/mineral)*								
Power(%)	*40Ar/39Ar*	*1σ*	*37Ar/39Ar*	*1σ*	*36Ar/39Ar*	*1σ*	*Ca/K*	*Cl/K*	*%40Ar atm*	*f 39Ar*	*40Ar*/39ArK*	*Age*	*2σ*
2.00 W	330.37	1.81	0.07	0.02	1.123	0.031	0.12		100.42	0.65	1.399	-14.82	± 190.47
2.10 W	16.48	0.08	0.01	0.01	0.041	0.001	0.03		72.89	3.33	4.468	46.55	± 5.26
2.20 W	5.69	0.03	0.01	0.01	0.004	0.000	0.02		21.30	5.15	4.479	46.66	± 0.94
2.40 W	4.44	0.02	0.00	0.00	0.000	0.000	0.01		2.59	32.24	4.329	45.12	± 0.46
2.50 W	4.41	0.02	0.01	0.00	0.000	0.000	0.01		1.25	6.99	4.351	45.35	± 0.49
2.70 W	4.38	0.02	0.01	0.00	0.000	0.000	0.01		1.10	15.60	4.328	45.11	± 0.46
2.90 W	4.31	0.02	0.01	0.00	0.000	0.000	0.01		1.40	7.51	4.252	44.32	± 0.48
3.20 W	4.43	0.02	0.01	0.00	0.001	0.000	0.01		4.63	10.15	4.222	44.02	± 0.50
3.80 W	4.73	0.02	0.01	0.00	0.002	0.000	0.02		10.91	13.45	4.210	43.90	± 0.52
4.50 W	8.61	0.04	0.01	0.00	0.015	0.000	0.02		52.54	4.45	4.088	42.64	± 2.09
5.50 W	7.21	0.05	0.06	0.04	0.009	0.000	0.12		37.94	0.39	4.474	46.61	± 3.00
7.00 W	7.43	0.19	0.03	0.18	0.011	0.002	0.06		43.11	0.08	4.224	44.04	± 12.23

Power(%)	*40Ar/39Ar*	*1σ*	*37Ar/39Ar*	*1σ*	*36Ar/39Ar*	*1σ*	*Ca/K*	*Cl/K*	*%40Ar atm*	*f 39Ar*	*40Ar*/39ArK*	*1σ*
Total/Average	4.899	0.009	0.006	0.001	0.0003	0.0000				100.00	4.293	0.009

J = 0.0058362 ± 0.0000292 Volume 39ArK = 2.371 Integrated Date = 44.44 ± 1.30 Ma

Plateau Age = 45.31 ± 0.38 Ma (2s, including J-error of .3%) MSWD = 2.1, probability = 0.067 64% of the 39Ar, steps 1 through 6

Inverse isochron (correlation age) results, plateau steps: Model 1 Solution (±95%-conf.) on 12 points Age = 44.66 ± 0.55Ma

40/36 intercept: 295 ± 20 MSWD = 5.7, Probability = 0

Laser	Isotope Ratios												
	661564 sericite				(sample/mineral)								
Power(%)	40Ar/39Ar	1σ	37Ar/39Ar	1σ	36Ar/39Ar	1σ	Ca/K	Cl/K	%40Ar atm	f 39Ar	40Ar*/39ArK	Age	2σ
2.00 W	5.54	0.04	0.22	0.05	0.011	0.000	0.40		58.53	3.01	2.300	24.08	± 1.89
2.20 W	5.03	0.03	0.03	0.01	0.001	0.000	0.06		9.19	24.92	4.565	47.48	± 0.64
2.30 W	4.69	0.03	0.02	0.01	0.000	0.000	0.04		3.31	11.62	4.534	47.17	± 0.59
2.50 W	4.57	0.03	0.01	0.02	0.000	0.000	0.02		2.09	20.42	4.479	46.60	± 0.57
2.80 W	4.51	0.06	0.01	0.01	0.000	0.000	0.02		2.40	15.62	4.400	45.79	± 1.20
3.20 W	4.28	0.04	0.01	0.01	0.000	0.000	0.02		3.58	15.57	4.123	42.93	± 0.78
3.60 W	3.58	0.02	0.08	0.06	0.001	0.000	0.14		9.65	5.24	3.231	33.73	± 0.63
4.50 W	3.15	0.02	0.01	0.09	0.002	0.000	0.03		16.02	2.88	2.644	27.66	± 0.86
6.00 W	2.81	0.02	0.13	0.25	0.002	0.001	0.24		19.10	0.72	2.275	23.82	± 3.70

Power(%)	40Ar/39Ar	1σ	37Ar/39Ar	1σ	36Ar/39Ar	1σ	Ca/K	Cl/K	%40Ar atm	f 39Ar	40Ar*/39ArK	1σ
Total/Average	3.848	0.009	0.024	0.005	0.0003	0.0000				100.00	4.028	0.013

J = 0.0058282 ± 0.0000291 Volume 39ArK = 1.480 Integrated Date = 42.00 ± 0.26 Ma

Age = 46.95 ± 0.73 Ma (2s, including J-error of .6%) MSWD = 2.9 Includes 72.5% of the 39Ar steps 2 through 5

Inverse isochron (correlation age) results, plateau steps: Model 1 Solution (±95%-conf.) on 9 points 0

0 0 Probability = 0